Shaping Effects on Magnetohydrodynamic Instabilities in a Tokamak Plasma Surrounded by a Resistive Wall

Dov Joseph Rhodes

Submitted in partial fulfillment of the
requirements for the degree of
Doctor of Philosophy
in the Graduate School of Arts and Sciences

COLUMBIA UNIVERSITY

2017

ABSTRACT

Shaping Effects on Magnetohydrodynamic Instabilities in a Tokamak Plasma Surrounded by a Resistive Wall

Dov Joseph Rhodes

The primary achievement of this study is the development of a new approach for optimizing the plasma shape in a tokamak fusion energy reactor. In the interest of producing the largest possible fusion power output, the shape is optimized to allow for the highest possible β - the ratio of the fluid to magnetic pressure - that can be sustained without the onset of magnetohydrodynamic (MHD) instabilities. To this end, the study explores the β-domain that is *stabilizable* by bulk plasma rotation, with rotation timescales comparable to the resistive dissipation time of the plasma tearing surfaces or of the surrounding vacuum chamber. Modern feedback control systems are able to apply external magnetic fields which are phased to emulate the effect of plasma rotation, making the technique applicable even to large tokamaks with inadequate plasma rotation.

In order to explore how the rotationally stabilizable β-domain is affected by plasma shaping, a new semi-analytic MHD model of a tokamak has been developed. In addition to shaped toroidal tokamak geometry, the model contains dissipative effects resulting from resistivity in both the plasma and in the vacuum-chamber wall. The inclusion of plasma and wall resistivity introduces a lower β-limit, associated with the onset of an unstable MHD mode, which can become dominated by either resistive-plasma (tearing) or resistive-wall effects in different parts of the parameter space. The computation time for analyzing the mode stability is greatly reduced by approximating the plasma current to reside in a thin layer, a form known as a *sharp-boundary model*. With fast calculations that focus on the key physics of these MHD instabilities, the model is able to explore qualitative trends of rotational stabilizability over a broad range of plasma shapes.

Results of this study predict that varying the elongation or triangularity of the plasma cross-section can lead to qualitatively different β-limits for the rotationally stabilizable domain. As the shape is varied, the upper bound in β for rotational stabilization is found to switch from resistive-wall dominated behavior to resistive-plasma dominated behavior. The optimal plasma shape, associated with the highest β-limit achievable with plasma rotation, is shown to be at the crossing point between the two domains. This discovery provides a basis for understanding existing experimental results and lays the groundwork for more quantitative studies with larger codes.

Contents

List of Figures

List of Tables

Acknowledgments[1]

Many inspiring and formative teachers have contributed to the completion of approximately 32 years of studenthood. Four in particular come to mind. I owe my initial intellectual development to my high school physics teachers, Ronen Jacovi who taught me how to ask questions, and Alex Kaploon who taught me how to answer them. No less important, I owe much of my physical and spiritual development to my karate instructors, Sensei Izidor Peled and Sensei Oded Friedman.

My formal introduction to the challenging field of plasma physics is owed to the accomplished faculty at Columbia University, Allen Boozer, Andrew Cole, Mike Mauel, Jerry Navratil and Francesco Volpe. It has been in great part facilitated by my interaction with Columbia labmates Mel Abler, Sarah Angelini, John Brooks, Pat Byrne, Brian DeBono, Ken Hammond, Paul Hughes, Jeff Levesque, Qian Peng, Niko Rath, Max Roberts, Daisuke Shiraki, Chris Stoafer and Ryan Sweeney; thanks for many illuminating discussions and for making the whole experience more enjoyable. Particular thanks to Max and Jeff for the awesome CAD renderings of a tokamak and a kink mode. Thanks to Jim Andrello and Nick Rivera who kept the HBT-EP experiment up and running. I would like to acknowledge Antoine Cerfon, Richard Fitzpatrick and Hank Strauss for ongoing interest in my work and helpful conversations along the way. Credit for ongoing guidance in this work goes to my esteemed colleagues Dylan Brennan of Princeton University and John Finn of Los Alamos (more recently at Tibbar Plasma Technologies). Most of all, I owe my theoretical and computational plasma physics skills to my mentor, Andrew Cole; a talented and passionate physicist - my deep gratitude.

This thesis is dedicated to a devoted support network of friends and family. Thanks to Mary Ann and Ron for planting the seed of fusion energy. Thanks to Richard Rauch and Alex Glasser for their contagious enthusiasm for the pursuit of knowledge and omphaloskepsis. Thanks to my wonderful second family in Israel, the Kogan-Rhodes. Thanks to Nataly for her enduring optimism and positive outlook. Thanks to Maggy for her hospitality and inspiring ambition and work ethic. Thanks to all six of my grandparents for their love and wisdom. Thanks to Mark and Eileen and Peggy for their moral support. Thanks to the more recent additions to my family, Steph and Linden, for raising the morale in tough times. Thanks to Avigal for her undying faith in me and to Eran for his courage and brotherhood. Thanks to my parents for teaching me most of what I know.

Thanks to my Rachel.

[1]This research was supported by DOE grants DE-FGO2-86ER53222 and DE-SC0014119.

Chapter 1

Introduction to Plasma Physics and Fusion Energy

This introductory chapter provides a non-specialist background on nuclear fusion and the effort to control it for energy production. We focus on the method of magnetic plasma confinement in a *tokamak* device, the leading candidate for controlled fusion. For further reading on the history and development of fusion energy, we recommend Seife [6], who clearly introduces the fundamental physics, or Cleary [7], who tells a compelling story of the initial historical development in the United States, England and the Soviet Union.

1.1 Nuclear Fusion: The Optimal Energy Source

The deuterium atoms in a liter of water contain more stored nuclear energy than 300 liters of gasoline [8]. The abundance of water on Earth makes this the largest known untapped source of energy for the future of humankind. This stored energy is accessed by fusing two atoms together into a larger atom with a mass slightly less than the sum of the two initial atoms. The lost rest mass is converted into energy according to Einstein's famous formula $E = mc^2$. In addition to a much higher energy density than fossil fuel, fusion produces no carbon ash or greenhouse gases.

Nuclear *fusion* is not to be confused with nuclear *fission* used in present day reactors. The difference is seen in the nuclear binding energy curve shown in figure 1.1. Fusion energy is released

by merging elements to the left of iron ('Fe' at the bottom of the curve) while fission energy is released by breaking apart elements to right. A fission chain reaction occurs at room temperature with a sufficient critical mass. This makes fission energy more accessible than fusion but also more dangerous due to the risk of a runaway chain reaction, with an exponentially growing number of energetic neutrons. A fusion reactor, on the other hand, would be inherently more safe because the process requires much higher temperature. In order to release fusion energy, two positively charged nuclei need enough starting energy to overcome their mutual electrostatic (Coulomb) repulsion. For this reason the most promising reactor fuel is a mixture of heavy hydrogen isotopes, deuterium and tritium, since they have the same charge as hydrogen but larger mass and hence more inertia to overcome the same repulsive force. Their combination

$$D + T \longrightarrow He^4(3.5MeV) + n(14.1MeV), \tag{1.1}$$

yields a helium ion and a neutron, which together carry an excess kinetic energy of $17.6MeV$. The helium ions are used to continue heating the plasma, while the energetic neutrons can be used to heat the reactor walls, which in turn could convert water into steam, turn a turbine and produce electricity. In further contrast with fission, fusion also does not require long-lived radioactive materials such as uranium or produce large amounts of transuranic waste.

The conditions for fusion energy are created by confining the fusion fuel as a collection of charged nuclei - known as *plasma* - at a high density (n) and temperature (T), with a sufficiently long energy confinement time (τ_E) for them to react. The product of these three parameters, called the fusion triple product, has a minimum threshold required to ignite a self-sustaining fusion process, given by the Lawson criterion [9]. Each fuel tends to have a different peak temperature for maximizing the fusion cross-section, or likelihood of a fusion reaction. Deuterium and tritium, for example, work best at temperatures on the order of $10keV$ or $100,000,000K$ (Kelvin), where the corresponding Lawson criterion is

$$nT\tau_E > 5 \times 10^{21} m^{-1} sKeV. \tag{1.2}$$

A main challenge of controlled fusion is to fulfill this plasma confinement criterion. Fusion is more safe than fission for electricity production because it requires such extreme conditions, and a reaction ceases as soon as the critical fusion conditions are lost. Full details of the nuclear processes and requirements are laid out by Glasstone and Lovberg [8].

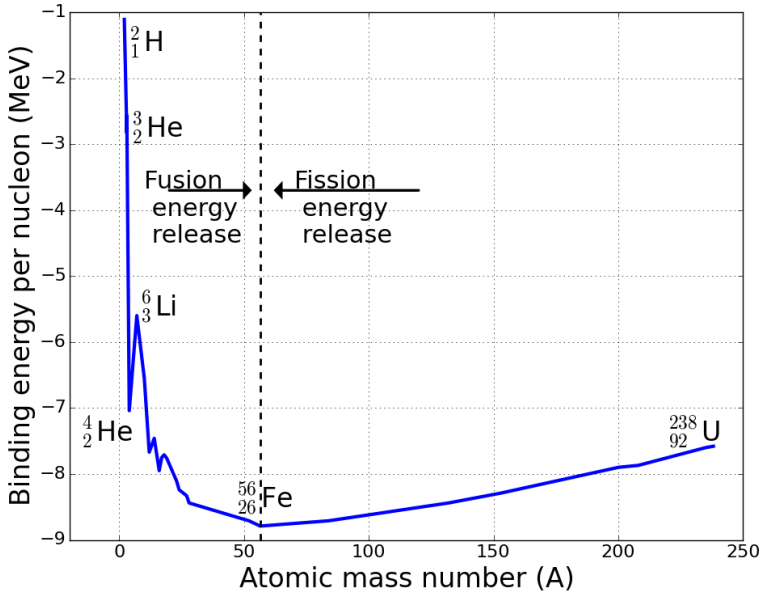

Figure 1.1: Binding energy per nucleon as a function of atomic mass. On the left lie the lighter atoms with potential fusion energy, while on the right lie the heavy elements with potential fission energy. The most stable element, iron ('Fe'), lies at the bottom of curve and releases no energy from fusion or fission. (Data taken from [1])

A plasma at such extraordinarily high temperature cannot be confined in any solid vessel. Fortunately there are other schemes of plasma confinement. The natural example of a working fusion reactor is the sun, a giant plasma which is confined by its own gravity. This principle is known as *gravitational confinement*. Ever since the first stars were ignited, approximately 100 million years after the big bang [10], gravitationally confined fusion has been the driving mechanism for almost all visible light and matter in the known universe. In this sense, all of our energy comes from fusion. The fusion process in the solar core, which involves different reactions than those in terrestrial fusion experiments, occurs at a lower temperature of $\sim 1.5keV$ but with density as high as $10^{30}m^{-3}$ (a factor of 10^5 higher than atmospheric density at sea level), and a confinement time of roughly $30,000$ years [11].

There are two common approaches to terrestrial fusion production. One approach is *inertial confinement*, where fusion conditions are created by rapid compression and are sustained for only a fraction of a second. This principle was proven successful with the invention of the hydrogen bomb, initialized by a fission bomb. Efforts to scale down this approach for energy production

are presently focused on replacing the fission bomb with a set of converging laser beams, as in the National Ignition Facility at the Lawrence Livermore National Laboratory. More information on inertial confinement fusion can be found in an introduction Pfalzner [12] or in the detailed text by Atzeni and Meyer-Ter-Vehn [13]

The second, more common approach toward fusion energy relies on the concept of *magnetic confinement*, sustaining a lower density plasma over a much longer reaction time. Several magnetic confinement schemes have been developed, all of which utilize the tendency of charged particles to move along magnetic field lines due to the Lorentz force. Using this principle, the plasma may be confined in vacuum at high temperature $\sim 10keV$ and moderate density $\sim 10^{20}m^{-3}$. At these conditions, the Lawson requirement demands a confinement time of at least 5 seconds. The present research is concerned with a magnetic confinement device called a tokamak, which will be introduced shortly.

A major challenge of magnetic confinement is the phenomenon of magnetohydrodynamic (MHD) instabilities, which make the Lawson condition difficult to achieve. A familiar example of a general (non-magnetic) fluid instability is constructed by balancing a heavy fluid *over* a lighter fluid (for example vinegar over oil). If undisturbed, the two fluids can theoretically be held in balance. The tentative equilibrium is unstable because the slightest perturbation will cause a sudden turbulent mixing of the two fluids (salad dressing!), known as a Rayleigh-Taylor instability. To understand the analogous instabilities that appear in a tokamak, we must first introduce some basic properties of a plasma.

1.2 Properties of Plasma

Plasma (from Greek): Moldable substance [14]

In physics, *plasma* refers to the fourth state of matter, after solid, liquid and gas. When a solid material is heated beyond a critical temperature, its crystalline structure melts away to form an approximately incompressible fluid called a liquid. Further heating destroys the molecular bonds, giving rise to a more compressible fluid called gas. Analogously, plasma forms from a gas when the atoms become hot enough to separate into freely moving negatively charged electrons and positively charged nuclei called ions.

Fundamentally, a plasma is a *collection of charged particles*, an ionized gas. While ordinary gas

is a collection of particles dominated by collisional interactions, rather like billiard balls, the charged particles in a plasma are dominated by electromagnetic interactions. This interaction is complicated by virtue of its longer range, as well as the possibility of repulsion by like-particles or attraction by opposites. External electric and magnetic forces introduce additional complexity.

Rather than tracking the distribution of individual particles, it is often convenient to model the plasma as a combination of two co-mingling oppositely-charged fluids. While in reality the plasma may consist of multiple species, as in the case of $D-T$ fusion, this *two-fluid* description is a more manageable initial model from a theory standpoint. Further simplicity is obtained by assuming that the two fluids have sufficient interaction to be described as a single homogenous *magnetohydrodynamic* (MHD) fluid. The MHD fluid conducts electricity and may be molded by electric and magnetic fields.

The models described above, clearly derived in an introductory textbook by Bellan [15], each facilitate the study of different features of plasma. For a more concrete look at this state of matter called plasma, consider some familiar terrestrial phenomena. Lightning, for example, occurs when so much electrostatic potential has built up between the clouds and the Earth's surface that a channel of air is momentarily ionized by a bolt of electric current. Another dramatic example is the aurora, which is seen when plasma from solar wind gets trapped in Earth's dipole-like magnetic field and is channeled to the poles, glowing as it collides with the atmosphere in the form of northern or southern lights.

Less dramatic but equally important is the ionosphere, a layer of plasma in the upper atmosphere. Early radar and communication systems such as ham radio and shortwave broadcasts were developed by reflecting radio waves off of the ionosphere. More recent applications of plasma include fluorescent lighting, plasma television, and surface coating/etching for computer chips. These applications all developed in the 20th century out of the study of plasma and its unique properties. For more details on basic plasma phenomena, we recommend the recently published textbook by Fitzpatrick [16].

The next section describes how these unique electromagnetic properties of plasma are conducive to magnetic confinement, and more specifically the operating principles of the leading candidate for a fusion reactor; the tokamak.

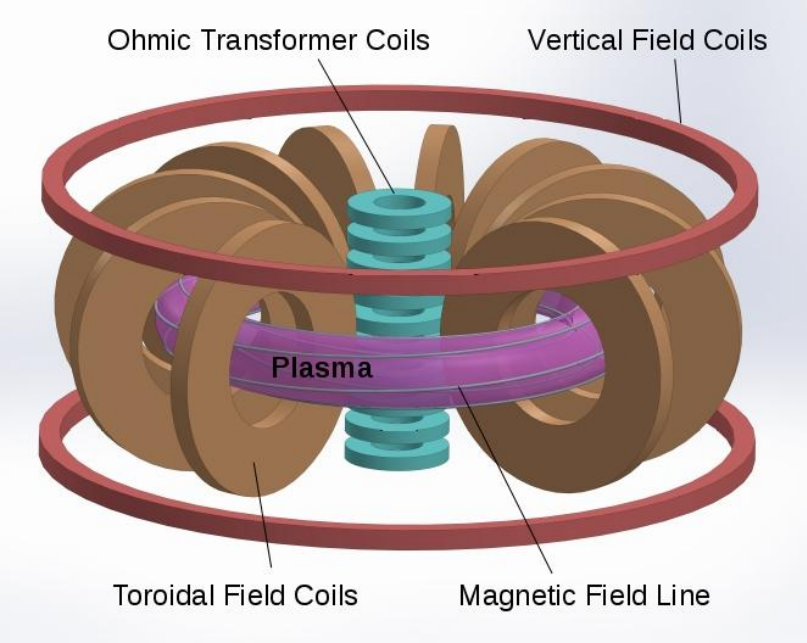

Figure 1.2: Schematic of a tokamak fusion reactor. (Figure courtesy of Dr. T. M. Roberts)

1.3 Magnetic Confinement and the Tokamak

Tokamak (Russian acronym): Toroidal chamber with magnetic coils [6]

A tokamak starts up by acting as a transformer, with the secondary coil replaced by a ring of plasma current, thereby ionizing the gas in the chamber and raising the temperature by collisional (Ohmic) heating. Auxiliary heating systems, such as electromagnetic radiation (resonant with the electron and ion cyclotron frequencies) and beams of neutral particles, are then applied to further heat the plasma to fusion temperatures. The schematic in Figure 1.2 shows the main features of a tokamak, including the Ohmic transformer coil which generates the plasma current, and the additional toroidal field and vertical field coils required for plasma stability. Invented in the Soviet Union during the 1950-1960s, the tokamak combines beneficial aspects of several other early devices developed primarily in the United States and England. To understand the operation of a tokamak, it is instructive to follow the pros and cons of these other experiments.

Utilizing the tendency of plasma to move along the magnetic field lines, a cylindrical column of plasma is mostly confined by an axial magnetic field, except at the ends of the cylinder. A simple solution to this obstacle is obtained by increasing the magnetic field strength at the ends to form a *magnetic mirror*, so that the accelerated orbital motion perpendicular to the field near the ends

causes the particles to be reflected back toward the center. Unfortunately, particles moving quickly along the field lines with very little perpendicular cyclotron motion always manage to escape out of the ends of the cylinder. Even at high temperature where the plasma is less collisional, a finite number of inter-particle collisions always ensures that some particles continually get knocked onto an escape trajectory.

Another class of magnetically confined fusion devices was considered based on the *pinch* effect; a self-induced ($J \times B$) inward force of a current-carrying conductor. The pinch approach requires rapid compression and is inherently pulsed, but has potential to achieve higher density and temperature. Two common types of pinch devices are the theta-pinch and the z-pinch, associated respectively with an azimuthal current (and axial field) and an axial current (and azimuthal field). The theta-pinch, pioneered by the Scylla experiment at the Los Alamos National Laboratory, has relatively good stability properties but no confinement at the ends. The z-pinch, made famous by the ZETA experiment at the UK Harwell Laboratory, has potential for better confinement but suffers from the creatively named *sausage instability*, in which local sections of the plasma column become increasingly compressed until they are completely pinched.

The tokamak is a toroidal device that combines properties of a theta-pinch and a z-pinch. It was invented in the 1950s by Soviet scientists Andrei Sakharov and Igor Tamm, independently of the western efforts. To avoid a sausage instability, the tokamak has an axial field (in the toroidal direction) which counters the compressional force. Compressing the column requires compressing the magnetic field lines as well. The equilibrium additionally requires a vertical field, to counter pressure and current forces that act to expand the ring of plasma outward. Although not heated by rapid compression as in the pinch devices, Ohmic heating boosted the tokamak potential for fusion far beyond other early experiments. While initially skeptical of the Soviet results, a delegation of British scientists traveled to Moscow in 1968 with a newly developed laser diagnostic system, and confirmed that the tokamak did indeed achieve a temperature of around $1keV$ (or $\sim 10^7 K$). This advantage led the international fusion research community to heavily invest in the study of tokamaks, and in the construction of the *ITER* experiment, expected to be completed in the next decade or so and provide the first demonstration of net energy gain from a fusion reactor.

Despite consistently dominating the race for fusion, a tokamak reactor at high current and pressure still suffers from a host of MHD instabilities, on a variety of length and time scales. With the additional stabilizing fields, the sausage instability was replaced by the infamous *kink* instability,

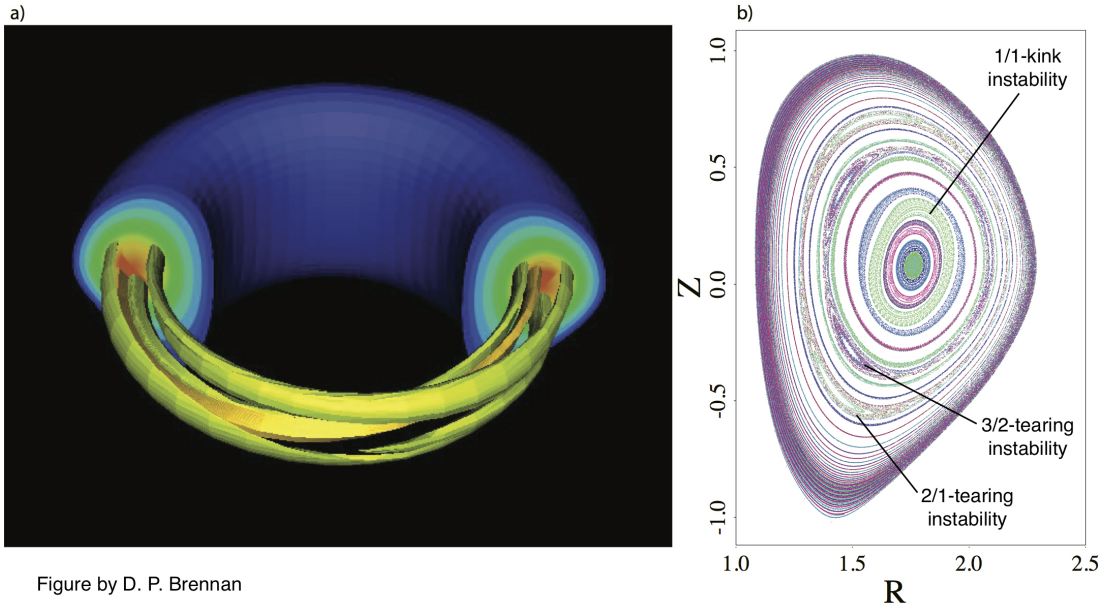

Figure 1.3: Magnetic surfaces showing a 1/1 kink instability in the core surrounded by a 3/2 tearing instability a) in a realistic nonlinear extended MHD simulation of the DIII-D tokamak, with an ideal-wall boundary condition. In b) is shown a Poincaré surface of the cross-section. (Figure courtesy of Dr. D. P. Brennan)

which deforms the entire plasma into a helical pattern going around the torus. In a chamber with resistive walls, the growth rate of a kink - typically on the order of microseconds - is slowed by wall eddy currents. Growing on the resistive decay time of the wall - typically on the order of milliseconds - this instability is known as the *resistive-wall-mode* (RWM). In addition to bulk deformation governed by wall resistivity, plasma resistivity introduces additional localized internal instabilities that tear and reconnect the magnetic field-line structure, changing the magnetic topology. This process occurs at resonant plasma surfaces, typically on a time scale of tens of milliseconds, and is known as a *tearing mode* (TM). In reality these different phenomena coexist as part of the general MHD behavior observed in a tokamak. Figure 1.3 depicts a simulation of a MHD instability in a DIII-D model with an ideal-wall boundary condition, showing a mode that exhibits combined kink and tearing behavior. This thesis is concerned with the stability of a system which exhibits coupled TM-RWM behavior, resulting in a combined MHD mode that is less stable than either the TM or the RWM individually.

The ITER device must robustly control these large scale MHD instabilities to avoid severe damage caused by large (mega-amp) currents striking the vacuum chamber wall. According to the official

ITER website [17], the central transformer coil must be strong enough to withstand forces equivalent to twice the thrust of the Space Shuttle at take-off (60 meganewtons, or over 6,000 tonnes). Ensuring robust control of MHD instabilities is one of the major challenges to be addressed in the experiment. In the words of Edward Teller, known for his role in the creation of the hydrogen bomb,

The fusion is easy; control is hard. [18]

Columbia University's HBT-EP team specializes in understanding and controlling MHD instabilities [3, 19–26]. The experiment includes several unique features. Movable conducting shells within the vacuum vessel are used to examine the extent of passive wall stabilization [27]. The closer the wall is to the plasma, the stronger the image currents that counteract the MHD instabilities. In addition to this passive stabilization, active feedback control of MHD instabilities is implemented using a high resolution array of magnetic sensors and control coils [28]. Since the mode stability is strongly affected by plasma rotation, as will be discussed extensively in this thesis, a bias probe is used for active rotation control [29]. A shaping coil has recently been installed to modify the shape of the plasma cross-section, predicted in this thesis to impact both the stability and the nature of observed instabilities. These features have largely motivated the present study, which demonstrates a new model for calculating MHD stability as well as a new approach for optimizing the plasma shape in a system with rotation and/or feedback control.

1.4 Thesis Outline

The remainder of this thesis is organized as follows:

- **Background on Resistive-Magnetohydrodynamic Stability with a Resistive Wall**: Motivates the study of non-ideal MHD instabilities. We begin with a discussion of basic concepts in ideal-MHD stability, followed by a discussion of how non-ideal effects such as wall resistivity and plasma resistivity can change the nature of the instability and introduce new timescales into the system. The addition of non-ideal effects leads to a discussion of bulk plasma *rotation*, which plays a key role in stabilizing the plasma in a tokamak. We introduce a framework of four different stability limits (referred to as the '4-β' framework of Brennan and Finn [4]) used to define domains of plasma behavior in response to rotation and/or externally applied feedback control.

- **Review of the High-β Reduced-MHD Model**: Reviews the typical comparative scaling of different plasma properties in a tokamak, and how they are used to define a reduced model that facilitates a simplified stability analysis. Using a step-function equilibrium profile in cylindrical geometry, we compare a single-mode dispersion relation for a low-β ideal-MHD instability driven by a current-gradient versus that of a high-β ideal-MHD instability driven by both a current-gradient and the combined effect of a pressure-gradient and magnetic-field curvature. We explain how the growth rate of this instability is slowed by the presence of a surrounding conducting wall, and how the β-limit increases in the idealized case of a perfectly conducting wall. Lastly we introduce a resistive resonant plasma layer into the high-β reduced-MHD formulation, further changing the stability properties of the system. This analytic model is used as a platform for understanding the 4-β framework of MHD stability.

- **Toroidal Extension of the Reduced-MHD Model**: Extends the reduced-MHD model with two mode harmonics coupled by toroidal curvature, included at first order in the inverse aspect ratio. This preliminary model is developed to analytically demonstrate the effect of geometric mode-coupling, which is central to this thesis.

- **Shaped Sharp-Boundary Model with Plasma and Wall Resistivity**: Contains the details of the new model, including descriptions of the sharp-boundary geometry, equilibrium, perturbed plasma response, perturbed vacuum response, resistive wall, resistive resonant surfaces and perturbed energy balance. The computational methods are also discussed.

- **Shaping Studies with the Sharp-Boundary Model**: Presents output of the sharp-boundary model. Initial benchmarking for a circular cross-section plasma shows how the resulting growth rate trends are consistent with previous work. The main results show how the stability limits, associated with the onset of mode growth, change as plasma shaping parameters are varied. Rotational stabilization is demonstrated, and the space of stability without rotation is compared with the space of rotational stabilizability.

- **Conclusion**: Summarizes the main results of this thesis and discusses possible directions for future research based on this work.

- **Appendices**

- **Toroidal Flux Coordinate Representations**: Describes flux coordinates in a torus, and relations used in the evaluation of generalized coordinates.
- **Code Manual**: Presents the structure of the Python code implementation of the sharp-boundary model, and provides examples of how to use it.

Chapter 2

Background on Resistive-Magnetohydrodynamic Stability with a Resistive Wall

Fusion power in a tokamak increases with β, the ratio of the volume-averaged plasma pressure (p) to magnetic-field (B) pressure:

$$\beta \equiv \frac{p}{B^2/2\mu_0}. \tag{2.1}$$

Unfortunately, increasing β beyond a critical value, known as the β-*limit*, drives magnetohydrodynamic (MHD) - not necessarily ideal MHD - instabilities that can destroy the plasma confinement. Stabilization methods include but are not limited to plasma rotation [5, 30–39] and feedback control [4, 19, 20, 40–48]. The aim of this thesis is to explore the extent to which bulk plasma rotation can raise the MHD β-limit of a resistive plasma surrounded by a resistive wall in shaped toroidal geometry.

In order to understand the effect of tokamak geometry on MHD stability, we first review general concepts of instabilities in the perfectly conducting fluid described by the *ideal*-MHD equations [49]. Considering equilibria that are destabilized at a finite β-limit, Section 2.2 explains how the presence of plasma resistivity and wall resistivity allows for stabilization of MHD modes by bulk plasma rotation. Section 2.3 describes the 4-β limit approach for evaluating the extent to which the plasma

can be stabilized by rotation and/or feedback control. Lastly, in Section 2.4 we briefly present the main results of this thesis and motivate the following chapters.

2.1 Ideal-Magnetohydrodynamic Stability

Starting from fundamental kinetic equations, the MHD model is obtained by velocity-space averaging over a distribution of electrons and ions, and combining the two resulting sets of fluid equations into a single fluid. The model is designed to capture low-frequency macroscopic behavior on the scale of the system size. Following the derivation in the seminal textbook by Freidberg [49], the *ideal*-MHD model is derived based upon three broad assumptions: (1) High collisionality, (2) small ion gyro radius and (3) small resistivity. In order to eliminate high-frequency short-wavelength phenomena, the derivation starts out with the preliminary neglect of the displacement current and net charge terms in Maxwell's equations, so that the dominant behavior is non-relativistic and quasi-neutral. This implies characteristic frequencies much lower than the electron plasma frequency and characteristic length scales much longer than the Debye length. Assuming high collision frequency compared to the characteristic time scale of interest implies that both the electrons and ions have time to equilibrate to a Maxwellian distribution. In this case viscosity can be neglected. Small ion gyro radius compared to the characteristic length scale implies that the electron Hall effect and diamagnetic drift can be neglected from Ohm's law. Finally, neglecting resistivity leads to the ideal form of Ohm's law $\boldsymbol{E}+\boldsymbol{v}\times\boldsymbol{B}=0$. Additional worthwhile discussions on MHD are found in textbooks by Bateman [49] and Bellan [15].

The assumptions above lead to a single-fluid model, with momentum carried by the ions and conserved energy combining both the electron and ion fluid contributions. An important implication of the ideal-Ohm's law is that the magnetic flux is 'frozen' to the plasma, so that the magnetic field-line topology is preserved. The inclusion of certain non-ideal effects such as resistivity or electron inertia in Ohm's law permits magnetic reconnection, associated in a tokamak with *tearing instabilities* that can grow into magnetic islands. This effect is captured in the present study with the inclusion of plasma resistivity, localized to resonant surfaces where the non-ideal physics dominates. To be specific, we will make use of the constant-ψ visco-resistive formulation [50, 51], which assumes that resistivity and viscosity dominate over inertia in a thin tearing layer of constant magnetic flux ψ. The bulk plasma outside of the tearing layer is still taken to obey the laws of ideal-MHD. This

method of incorporating non-ideal effects will be central to the present formulation.

The ideal-MHD boundary conditions are discussed chapter 3 of Reference [49]. In a model that allows surface currents at the plasma boundary, the plasma terminates in a corresponding jump in the tangential magnetic field. This leads to a jump in the magnetic pressure, which is balanced by a jump in the fluid pressure. In this case the ideal-MHD conditions at the plasma boundary become

$$\hat{\boldsymbol{n}}\cdot\boldsymbol{B}|_{S_p} = 0. \tag{2.2}$$

$$(\hat{\boldsymbol{n}}\times\boldsymbol{E} - (\hat{\boldsymbol{n}}\cdot\boldsymbol{v})\boldsymbol{B})_{S_p} = 0, \tag{2.3}$$

$$[\![p + B^2/2\mu_0]\!]_{S_p} = 0. \tag{2.4}$$

Here $[\![\cdot]\!]$ represents a jump across the plasma boundary S_p and $\hat{\boldsymbol{n}}$ is the unit vector normal to the boundary. These conditions can be used to construct a *sharp-boundary model* of a plasma, where the bulk plasma current is confined to the plasma boundary. As detailed in Chapter 5 of this thesis, the present study extends the sharp-boundary equilibrium to include non-ideal effects such as plasma resistivity and wall resistivity, which modify the stability of the dominant MHD mode.

The properties of MHD equilibrium, governed by the momentum equation $0 = \boldsymbol{J}\times\boldsymbol{B} - \boldsymbol{\nabla}P$ along with Ampere's law and $\boldsymbol{\nabla}\cdot\boldsymbol{B} = 0$, are detailed by Freidberg for various configurations throughout chapters 4-7 of Reference [49]. Skipping to the *perturbed* equilibrium, discussed in chapter 8 of Reference [49], the driving forces behind MHD instabilities can be analyzed by linearizing the MHD momentum equation about an equilibrium:

$$\rho_0\frac{\partial^2\boldsymbol{\xi}}{\partial t^2} = \frac{1}{\mu_0}(\boldsymbol{\nabla}\times\boldsymbol{B})\times\boldsymbol{B}_1 + \frac{1}{\mu_0}(\boldsymbol{\nabla}\times\boldsymbol{B}_1)\times\boldsymbol{B} - \boldsymbol{\nabla}p_1 \equiv \boldsymbol{F}(\boldsymbol{\xi}). \tag{2.5}$$

Here $\boldsymbol{\xi} = \int \delta\boldsymbol{v}dt$ is the perturbed plasma displacement away from equilibrium, $\boldsymbol{B}_1$ is the perturbed magnetic field and p_1 is the perturbed pressure. $\boldsymbol{F}(\boldsymbol{\xi})$ is called the MHD *force operator*. This form leads to a concise expression for the total (kinetic + potential) perturbed energy

$$\delta K + \delta W = \frac{1}{2}\int d^3x \left(\rho_0\dot{\boldsymbol{\xi}}^2 - \boldsymbol{\xi}^*\cdot\boldsymbol{F}(\boldsymbol{\xi})\right). \tag{2.6}$$

The system is unstable if the perturbed potential energy δW is negative. One method of evaluating the perturbed energy is an eigen-mode analysis, with a time dependent displacement $\boldsymbol{\xi} \propto e^{\gamma t}$, so

that the growth rate γ and corresponding mode structure $\boldsymbol{\xi}$ are given by the dominant eigenvalue and eigenvector of the system. The growth rate of ideal instabilities is characterized by the Alfvén time $\tau_A = L\sqrt{\mu_0\rho}/B$, where L is the system length scale and ρ is the plasma density. In the absence of energy dissipation it can be shown that the force operator is self-adjoint, and hence that the perturbed energy is purely real (with no imaginary component). Since γ^2 is real, the transition from stable to unstable modes must pass through $\gamma^2 = 0$. The growth rate γ is thus either purely real, representing a growing or decaying mode, or purely imaginary, representing a marginally stable rotating mode. As will become apparent, the introduction of non-ideal effects will permit complex stability transitions, with growing or damped rotating modes subject to the influence of plasma rotation.

As described in Reference [49] under the discussion of the *extended energy principle*, the inclusion of surface currents on the plasma boundary allows the perturbed potential energy to be written as a sum of the vacuum, plasma and *surface* energy,

$$\delta W_V = \frac{1}{2}\int_{vacuum} d^3x \frac{1}{\mu_0}|\delta\boldsymbol{B}|^2, \tag{2.7}$$

$$\delta W_P = \frac{1}{2}\int_{plasma} d^3x \left\{ \frac{1}{\mu_0}|\delta\boldsymbol{B}_\perp|^2 + \frac{1}{\mu_0}\left|\delta\boldsymbol{B}_\parallel - \frac{\mu_0\boldsymbol{\xi}\cdot\boldsymbol{\nabla}p}{B^2}\boldsymbol{B}\right|^2 + \Gamma p\,|\boldsymbol{\nabla}\cdot\boldsymbol{\xi}|^2 + \frac{\boldsymbol{J}\times\boldsymbol{B}}{B^2}\boldsymbol{B}\times\boldsymbol{\xi}\cdot\delta\boldsymbol{B} - 2(\boldsymbol{\xi}\cdot\boldsymbol{\nabla}p)(\boldsymbol{\xi}\cdot\boldsymbol{\kappa})\right\}, \tag{2.8}$$

and

$$\delta W_S = \frac{1}{2}\int_{surface} d\boldsymbol{S}\cdot\left[\!\left[\boldsymbol{\nabla}\left(p + \frac{1}{2\mu_0}B^2\right)\right]\!\right](\hat{\boldsymbol{n}}\cdot\boldsymbol{\xi})^2. \tag{2.9}$$

The vacuum energy is positive definite and therefore stabilizing. The plasma energy is written in terms of five components, each attributed to different physical mechanisms. The first three, which are positive definite, represent the shear-Alfvén, fast/compressional-Alfvén, and sound wave. The last two terms, which can be destabilizing, are associated with current and pressure driven instabilities. The surface energy, associated with a surface current at the plasma boundary, can be positive or negative depending upon the balance of the fluid pressure and the magnetic pressure.

In a tokamak, the dominant ideal mode typically wraps helically around the torus, and is characterized in a Fourier basis according to the convention $e^{i(m\theta - n\phi)}$ in terms of the poloidal and toroidal angles, θ and ϕ. Figure 2.1 depicts a toroidal instability characterized by - but not limited to -

Figure 2.1: Typical toroidal MHD instability characterized by a $m/n = 3/1$-kink, traversing the toroidal direction 3 times for each poloidal orbit. (Figure courtesy of Dr. J. P. Levesque)

a $m/n = 3/1$-kink, traversing the toroidal direction 3 times for each poloidal orbit. The poloidal (m) harmonics are coupled by the toroidal curvature and cross-sectional shape of the plasma. This geometric mode-coupling plays an important role in the resulting mode structure and stability.

Note the dependence of the perturbed plasma energy δW_P on the pressure-gradient/curvature driven component $-2(\boldsymbol{\xi}\cdot\boldsymbol{\nabla}p)(\boldsymbol{\xi}\cdot\boldsymbol{\kappa})$, which has a destabilizing effect when the pressure gradient is aligned with the curvature. The effect of the toroidal curvature is depicted in Figures 2.2a and 2.2b, which respectively show an overhead view of a torus and a shaped cross-section. The sign of the pressure/curvature contribution can be seen to switch from positive (stabilizing) to negative (destabilizing) as a field line transitions from the inboard to the outboard side of the torus. The curvature of the shaped plasma cross-section, not expressed in Figures 2.2a and 2.2b, also contributes to the total curvature. An important aspect of tokamak design is the minimization of the so called *bad* curvature, aligned with the pressure gradient, by shaping the plasma cross-section. The present study aims to develop a methodology for shape optimization, including additional non-ideal (dissipative) physics to be discussed next.

2.2 Rotational Stabilization

An central aspect in the present study is the *stability limit*, where the mode goes from stable (negative growth rate) to unstable (positive growth rate). Since any instability, even slowly growing, can eventually lead to a disruption which destroys the plasma, it is important to map out the space of parameters which permit stable operation. Rather than trying to reduce the growth rates, it is preferable to use stabilization methods such as rotation and feedback control to extend the stability

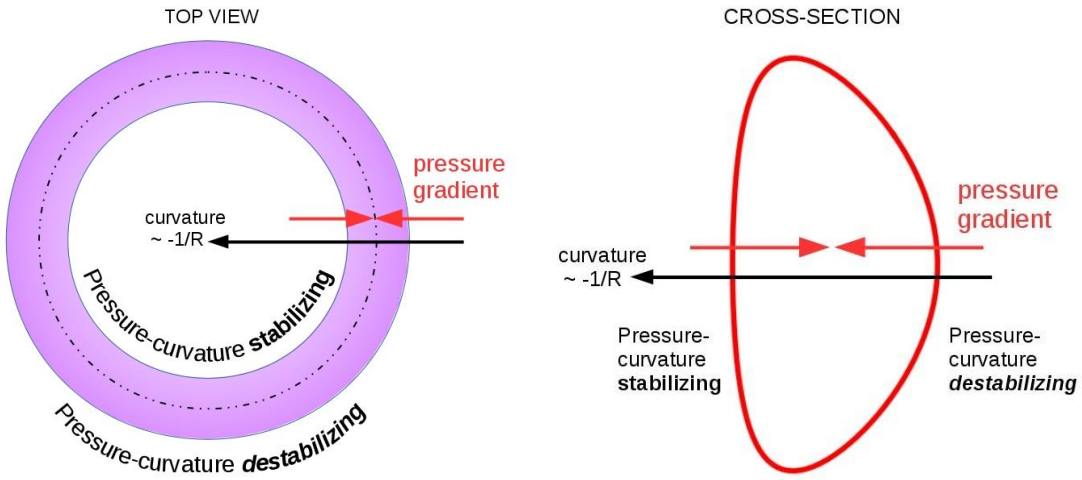

(a) (b)

Figure 2.2: The direction of the pressure gradient versus the toroidal radius of curvature in an (a) overhead view of a toroidal plasma and a (b) side view of the cross-section. The combined pressure-curvature effect is destabilizing when the pressure gradient and curvature vector are aligned.

limits. The goal of this approach is to extend the stable operational domain for plasma confinement. As previously mentioned, a particular stability parameter of interest is β, the volume-averaged ratio of the plasma pressure to the magnetic pressure. The stable domain in this study will refer to the β-domain which permits stable operation with respect to the linear onset of the least stable MHD mode. This least stable mode combines effects of plasma resistivity and wall resistivity, and is destabilized as β is raised beyond a critical value denoted β_{rp-rw}, referred to as the *resistive-plasma resistive-wall limit*. The *stabilizable* domain will refer to the maximum value of β_{rp-rw} in the presence of rotation.

One way to understand the physics of rotational stabilization is by thinking of the least stable mode, associated with the β_{rp-rw} limit, as a product of two geometrically coupled modes; a TM with finite flux at the tearing layers and zero flux at the wall, and a RWM with finite flux at the wall and zero flux at the tearing layers [4]. Any system of two coupled modes exhibits a mode interaction which depends upon the proximity of the γ_c roots in the complex plane. Plasma rotation in the present plasma-wall system produces a relative phase-shift of the complex roots which changes the coupling of the two modes. This effect tends to raise the β_{rp-rw} when the tearing layer and the wall have comparable timescales, with similar rotation timescales. Rotational stabilization has been verified experimentally [30–32] and explained theoretically using a number of dissipation mechanisms

including sound wave damping [33], resistivity [5, 34] and viscosity [35, 36], as well as kinetic effects such as the resonance between mode rotation and the precession drift frequency of trapped particles [38, 39].

The physics of rotational stabilization begs the question, to what extent can rotation stabilize the plasma and how are the bounds affected by different plasma parameters? To help address this question, this study investigates how rotational stabilization is affected by the plasma cross-sectional shaping in axisymmetric toroidal geometry. The answer to this question is addressed using a framework of four β limits, calculated *without* rotation, that are used to evaluate the rotationally stabilizable domain. The following sections of this chapter introduce the 4-β approach of Brennan and Finn [4] to MHD stability analysis, followed by background material that motivates the key ideas in this study, and lastly a summary of the main discoveries.

2.3 The 4-β Framework

The study examines the linear onset of MHD instabilities with a broad poloidal harmonic spectrum and fixed toroidal harmonic n=1, in a plasma that is stable at zero β and destabilized at finite β. Following Brennan and Finn [4], four β-limits calculated *without* rotation or feedback control are used to evaluate the extent to which rotation or feedback control can raise the least stable limit in a resistive plasma surrounded by a resistive wall. Starting with an ideal-plasma ideal-wall (ip-iw) system, raising β produces a kink mode that goes unstable at a relatively high limit, denoted β_{ip-iw}, with a fast growth rate characterized by the Alfvén timescale τ_A. Wall resistivity allows the perturbed magnetic flux to penetrate the wall on a resistive timescale τ_w, introducing a slower growing instability known as the resistive wall mode (RWM), which goes unstable at a lower *ideal-plasma resistive-wall* (ip-rw) limit $\beta_{ip-rw} < \beta_{ip-iw}$. Similarly, plasma resistivity in a system with an ideal wall introduces yet another non-ideal instability known as the tearing mode (TM), which grows on a tearing timescale τ_t, and is also destabilized at a lower *resistive-plasma ideal-wall* (rp-iw) limit $\beta_{rp-iw} < \beta_{ip-iw}$. Lastly, a toroidal system containing both wall resistivity and plasma resistivity goes unstable at a *resistive-plasma resistive-wall* (rp-rw) limit β_{rp-rw}, below the other three limits. The least stable mode appears above β_{rp-rw} and grows on a timescale that depends upon both τ_w and τ_t, coupling the tearing and the resistive-wall processes by their comparable timescales as well as their similar physics and their mutually inductive perturbed currents. Rather

than referring to separate modes, the present unified approach suggests that common designations such as kink, RWM and TM should be thought of as referring to the dominant MHD mode which transitions through qualitatively different domains of the parameter space. This unified approach was pioneered in a cylindrical study by Finn [52] and a toroidal circular cross-section study by Betti [37], who independently developed models to study MHD stability over a range of β, encompassing both TM and RWM behavior. The approach allows the dominant mode behavior to smoothly transitions at each of the limits described above:

1. resistive-plasma resistive-wall limit β_{rp-rw}
2. resistive-plasma ideal-wall limit β_{rp-iw}
3. ideal-plasma resistive-wall limit β_{ip-rw}
4. ideal-plasma ideal-wall limit β_{ip-iw}

For a circular cross-section tokamak, a typical β-limit ordering in this 4-β analysis was found to be $\beta_{rp-rw} < \beta_{rp-iw} < \beta_{ip-rw} < \beta_{ip-iw}$ in both the cylindrical model by Finn [52] and the high aspect-ratio toroidal model by Betti [37]. Building upon the 4-β approach, Brennan and Finn [4] constructed a cylindrical model with feedback control, to show that the plasma response to rotation and/or feedback control is characterized by the four β domains associated with the four abovementioned β-limits calculated *without* rotation or feedback. With cylindrical geometry that typically satisfies the β-limit ordering mentioned above, the study by Brennan and Finn indicates that the β_{rp-rw} can be raised by rotation up to the next limit β_{rp-iw}. Richardson, Finn and Delzanno [53] found that the same ordering also applies in a typical reversed field pinch, with the current density parameter $\lambda_0 \equiv \boldsymbol{J}\cdot\boldsymbol{B}/B^2(r=0)$ in place of β. In a feedback control system with complex normal sensors and real tangential sensors, the imaginary component of the normal-field gain can emulate the effect of wall rotation [43]. This fake rotating shell approach, used by Reference [43] to show that a resistive wall between the plasma and the feedback array (or another wall) can behave like an ideal wall in the presence of feedback, has a similar effect to toroidal plasma rotation in the opposite direction, with exact equivalence in a cylinder [48]. While feedback with complex tangential and normal field gains can further stabilize the mode, the present study focuses on the domain of *rotational stabilizability*, or equivalently the domain of feedback control with imaginary normal-field gain. Rotational stabilizability refers here to the maximum extent to which rigid plasma

rotation, at moderate rates comparable with τ_w or τ_t, can raise the β-limit of the least stable mode. A general rule first demonstrated in the present study, is that the domain of rotational stabilizability is bounded by the lowest ideal β-limit, which can be given by either β_{rp-iw} or β_{ip-rw}. This rule was examined for the specific case of varying wall distance in studies by Finn [52] and Betti [37]. This finding has implications for the type of ensuing linear mode behavior. In the common terminology, $\beta_{rp-iw} < \beta_{ip-rw}$ implies rotational stabilization up to the linear onset of a TM-dominated instability, whereas the reverse case $\beta_{ip-rw} < \beta_{rp-iw}$ implies rotational stabilization up to the linear onset of a RWM-dominated instability. We conjecture that the nature of the linear β-limit (β_{rp-iw} or β_{ip-rw}) determines the dominant type of non-linear behavior (TM or RWM) observed in experiments.

2.4 Main Thesis Results

This thesis presents the first shaping study of a non-ideal MHD mode including the effects of plasma and wall resistivity across wide range of plasma parameters. The rotationally stabilizable β-domain is shown to be significantly affected by the geometric mode-coupling induced by shaped toroidal geometry. In the past, geometric mode-coupling effects of cross-sectional shaping in toroidal geometry have been studied separately for ideal-plasma (kink) modes, and for resistive-plasma (tearing) modes. Early shaping studies focused on the ideal external kink instability, applying a sharp-boundary model with no rational surfaces and no wall. Using a sharp-boundary model with high aspect-ratio and elliptical cross-section, Freidberg and Haas [54] found maximum stability for a height to width ratio of 2.2. An extension by Freidberg and Grossmann [2] to a more general shape showed triangularity to be destabilizing in the absence of elongation.

Including internal rational surfaces in a diffuse plasma profile, a number of ideal-plasma numerical shaping studies of the DIII-D experiment were undertaken by Lazarus et. al. [55], Turnbull et. al. [56] and Kessel et. al. [57] for the ideal-wall case, and by Ferron et. al. [58] for the no-wall case. Similar studies were conducted by Menard et. al. [59], Miller et. al. [60] and Turnbull et. al. [61], to test for stability in a low aspect-ratio tokamak around the construction time of the NSTX experiment. These numerical studies all suggested that cross-sectional shaping - most notably a combination of elongation and triangularity - can help raise the stability limit, but included too few data points to discern an optimal shape or to analyze the physics trends from shaping. In contrast to the domain dominated by the external kink resonance, analytic studies by Bondeson and Bussac

[62] and by Lutjens, Bondeson and Vlad [63] showed that the *internal* kink mode, with toroidal number $n = 1$ and low poloidal m-numbers (typically $m = 2$), is *destabilized* by vertical elongation. More extensive models by Eriksson and Wahlberg [64] and by Martynov, Graves and Sauter [65] showed that triangularity, on the other hand, stabilizes the internal kink. Shaping studies focused on resistive plasma behavior showed that the TM is generally stabilized by both elongation and triangularity. An analytic model known as the T7 code was developed by Fitzpatrick et. al. [66], and recently benchmarked by Ham et. al. [67] with the MARS-F code. A neoclassical-TM model by Kruger et. al. [68], based on non-linear Rutherford theory, showed that shaping effects are strongly dependent on the aspect-ratio and magnetic shear.

To explore the effects of plasma shaping on the stability and rotational stabilizability of resistive-plasma resistive wall modes, we have developed a shaped sharp-boundary model in toroidal geometry including resistive resonant surfaces and a resistive wall. The model is based on a study by Fitzpatrick [69] which incorporated tearing surfaces into a sharp-boundary formulation to examine the effects of shaping on error-field response, without toroidal curvature or a resistive wall. To generalize the geometry in the present model we incorporate toroidal curvature, based on an ideal stability model by Freidberg and Grossmann [2], retained up to first order in an expansion in the inverse aspect-ratio ϵ. An additional extension to up-down asymmetry allows the model to capture the shape of a single-null diverted plasma. The development of a resistive wall boundary condition facilitates the generalization of the Brennan-Finn [4] 4-β analysis to shaped toroidal geometry. Using the 4-β framework, the new sharp-boundary model reveals qualitative trends of stability and rotational stabilizability over a broad range of β, safety factor, wall radius, elongation, triangularity and up-down asymmetry.

The main result discovered using this sharp-boundary model is that plasma shaping can cause an interchange of rp-iw and ip-rw β-limits, modifying the β-limit ordering from $\beta_{rp-rw} < \beta_{rp-iw} < \beta_{ip-rw} < \beta_{ip-iw}$ to $\beta_{rp-rw} < \beta_{ip-rw} < \beta_{rp-iw} < \beta_{ip-iw}$. While β_{rp-rw} is always lowest and β_{ip-iw} sets the upper bound, there is no constraint on the order of the two middle limits β_{rp-iw} and β_{ip-rw}. For circular cross-section, an interchange of β_{rp-iw} and β_{ip-rw} was observed by varying the wall radius in stability studies by Finn [52] and Betti [37]. The present study reaffirms the mode interchange induced by wall radius, and goes on to demonstrate likewise interchanges by varying the safety factor, elongation and triangularity. This discovery shows that different domains of the tokamak parameter space exhibit rotational stabilization bounded by either TM or RWM type

behavior. An optimal shape for stabilizability by rotation - or an equivalent feedback with imaginary normal-field gain - was found to typically reside in a window around the transition from TM-limited to RWM-limited domains, i.e. $\beta_{rp-iw} = \beta_{ip-rw}$. We emphasize that, rather than an exhaustive optimization over the parameters space, the study builds a qualitative understanding of how plasma shaping affects the domains of MHD stability and rotational stabilizability. While comparison with experiment would require diffuse current and pressure profiles, the sharp-boundary model makes it convenient to change a single parameter at a time and to examine the resulting trends. Resulting qualitative observations are intended to improve the interpretation of existing experiments as well as to guide larger codes in the optimization of future tokamak devices.

Before proceeding to the new sharp-boundary model (Chapter 5) and main results of this study (Chapter 6), we construct a series of simple analytic models to develop an intuition for the physics of the different stability limits in a system with both plasma and wall resistivity. Chapter 3 presents an overview of the *high-β reduced-MHD model*, which applies typical tokamak scaling expansions to simplify the linear stability analysis of MHD modes. We introduce central concepts in MHD stability such as current-drive, pressure-drive and wall resistivity. Adding resistive resonant plasma layers, we examine how the 4-β limits compare in existing cylinder models. Chapter 4 then presents a new extension of the reduced-MHD model with first order toroidal curvature, used to analytically demonstrate the effects of geometric mode coupling.

Chapter 3

Review of the High-β Reduced-MHD Model

This chapter introduces the high-β reduced-MHD model, starting with the ideal form and then separately adding wall resistivity followed by plasma resistivity in order to explain the physics effects of each feature. In its original form, the low-β reduced-MHD model was developed by a variety of authors [70–73] in the 1970's as an analytic tool for qualitative study of MHD stability in a tokamak. The model utilized the typical tokamak scalings, which originally involved relatively low-β, to substantially simplify the analysis of current-driven MHD modes. Strauss[1] [74] subsequently generalized the reduced-MHD model with a high-β scaling that accounted for both current and pressure in driving MHD instabilities. An introduction to low-β reduced-MHD, with $\beta \sim \epsilon^2$, is found in a textbook by Kadomtsev [75]. The high-β version with $\beta \sim \epsilon$ is presented in a textbook by Hazeltine and Meiss [76], under the section describing a flute reduction of the shear-Alfvén law.

In either case (low or high β), the model describes an incompressible plasma with a uniform axial magnetic guide-field B_0 that is much larger than the cross-sectional field $B_\perp$, with $q \sim 1$. This scale separation allows the MHD equations to be expanded in $B_\perp/B_0 \ll 1$. While the field ordering is independent of the geometry, the scaling is motivated in toroidal geometry by the inverse aspect ratio ϵ, often used in expansions for a high aspect-ratio torus. This ordering in toroidal geometry implies that $k_\parallel/k_\perp \sim a/R = \epsilon$ and hence that the compressional Alfvén frequency is much larger than the

[1] We wish to take this opportunity to acknowledge Hank Strauss for his ongoing interest in the present work and eagerness to discuss it at conferences over the past few years.

shear-Alfvén frequency. In the interest of studying the slower timescale phenomena associated with the shear Alfvén mode, the compressional modes are assumed to have been equilibrated. The focus on perpendicular dynamics allows the plasma perturbation to be described by three scalar variables; (i) magnetic flux ψ, (ii) stream function ϕ and (iii) pressure p.

This chapter begins with a general derivation of the high-β reduced-MHD model. A series of step-function profile models is then constructed, adding one feature at a time in order to illustrate different physics. We start in Section 3.1 with the Shafranov model [70] of a zero-β current-driven ideal external kink instability. Adding a pressure jump coinciding with the current jump, Section 3.2 presents an extension to high-β and show how increasing β can destabilize a mode that is stable at zero β. The critical value for the onset of instability is called the β-limit.

The combined current/pressure step-function profile is further extended with *non-ideal effects* in two stages. First, in Section 3.3 we include the stabilizing effect of a conducting wall concentric to the ideal plasma. The case of a perfectly conducting wall produces a higher β-limit than the resistive-wall case. Secondly, in Section 3.4 we include a resistive-plasma layer between the current/pressure step and the wall, following a formulation by Finn [5]. We refer to this formulation as the *3-layer* model (the three layers being (i) the current/pressure step, (ii) the resonant plasma layer and (iii) the conducting wall). As with the conducting wall, the case of an ideal resonant plasma layer produces a higher β-limit than the case of a resistive resonant plasma layer. We show how the presence of both plasma and wall resistivity produces the least stable β-limit, referred to as the *resistive-plasma resistive-wall limit*, or β_{rp-rw}.

A property of the 3-layer model is that taking the resonant plasma layer to be ideal (perfectly conducting) eliminates the plasma coupling to the wall. To avoid this limitation, which is unique to the step-function cylindrical model with the resonant layer beyond the current and pressure gradients, Brennan and Finn [4] created an extended version with the pressure step between the resonant plasma layer and the wall, thus driving the resistive-wall instability even when the resonant plasma layer is taken to be ideal, and emulating the type of coupling observed in toroidal geometry. This formulation, which we present in Section 3.5 and refer to as the *4-layer* model (referring to the (i) current-step, (ii) resonant plasma layer, (iii) pressure-step and (iv) conducting wall) was used by Brennan and Finn as a basis for understanding how a resistive-plasma surrounded by a resistive-wall responds to rotation and/or feedback control.

As discussed in the previous chapter, the plasma response can be analyzed with the help of the

ideal β-limits, achieved by taking an ideal resonant plasma layer and/or an ideal conducting wall. This approach is referred to as the '4-β' framework, based on the four β-limits β_{rp-rw}, β_{rp-iw}, β_{ip-rw} and β_{ip-iw}, calculated *without* rotation or feedback. The 4-β framework will be used throughout this thesis to evaluate the bounds for stabilizability by rotation, or by an equivalent feedback control with imaginary normal-field gain.

Reduced-MHD Ordering

The high-β model assumes the following ordering:

$$B_0 \sim 1, \qquad \boldsymbol{B}_\perp \sim v_\perp \sim p \sim \epsilon. \tag{3.1}$$

This scale separation leads to a separation in parallel and perpendicular dynamics, with $k_\parallel/k_\perp \sim \epsilon$ leading to

$$\boldsymbol{\nabla}_\perp \sim 1, \qquad \partial_z \sim \partial_t \sim \epsilon, \tag{3.2}$$

Having also assumed that the parallel dynamics act on a fast timescale and have been equilibrated, we find that

$$\hat{\boldsymbol{b}}\cdot\boldsymbol{\nabla} = \partial_z + \frac{1}{B_0}\boldsymbol{B}_\perp\cdot\boldsymbol{\nabla}_\perp \sim \epsilon, \qquad D_t = \partial_t + \boldsymbol{v}_\perp\cdot\boldsymbol{\nabla}_\perp \sim \epsilon, \tag{3.3}$$

for the field-aligned derivative and the convective time derivative, respectively. With the ordering laid out, the separation of axial and perpendicular length scales leads to the set of perpendicular flow and field requirements

$$\boldsymbol{\nabla}_\perp\cdot\boldsymbol{v}_\perp = 0, \qquad \boldsymbol{\nabla}_\perp\cdot\boldsymbol{B}_\perp = 0, \tag{3.4}$$

eliminating parallel dynamics but maintaining flute-like current and pressure driven instabilities that are of primary concern in this model. This allows the flow to be described by a scalar stream function and similarly the magnetic field to be described by a scalar magnetic potential:

$$\boldsymbol{v}_\perp = \boldsymbol{\nabla}_\perp\times(\phi\hat{\boldsymbol{b}}_0), \qquad \boldsymbol{B}_\perp = \boldsymbol{\nabla}_\perp\times(\psi\hat{\boldsymbol{b}}_0). \tag{3.5}$$

Using Ampere's law, the parallel current may be written in terms of the flux function as

$$\boldsymbol{J}_\parallel = -\hat{\boldsymbol{b}}_0\nabla_\perp^2\psi. \tag{3.6}$$

Preliminary Equations

In contrast with the low-β derivation which neglects the destabilizing effect of the pressure gradient, the following high-β derivation based on section 7.4 of Hazeltine and Meiss [76] includes both current and pressure gradients, both of which play an important role in driving instabilities. Before reduction, the MHD momentum can be rewritten, using Ampere's law, as

$$\rho \frac{D\boldsymbol{v}}{Dt} = -\boldsymbol{\nabla}_\perp \left(p + \frac{B^2}{2} \right) + B^2 \boldsymbol{\kappa}, \tag{3.7}$$

a balance of the total pressure (fluid and magnetic) and the tension from field-line curvature $\boldsymbol{\kappa} \equiv \hat{\boldsymbol{b}} \cdot \boldsymbol{\nabla} \hat{\boldsymbol{b}}$. The curvature is dominated by the toroidal component $\boldsymbol{\kappa}_0 = \hat{\boldsymbol{b}}_0 \cdot \boldsymbol{\nabla} \hat{\boldsymbol{b}}_0 = -\hat{\boldsymbol{R}}/R \sim \epsilon$, based on the dominant guide field direction is $\hat{\boldsymbol{b}}_0 = \hat{\boldsymbol{e}}_z$. Crossing the equation above with the dominant curvature $\boldsymbol{\kappa}_0$ produces

$$-\boldsymbol{\kappa}_0 \times \boldsymbol{\nabla}_\perp B^2 = 2\boldsymbol{\kappa}_0 \times \left(\boldsymbol{\nabla}_\perp p + \rho_0 \frac{D\boldsymbol{v}}{Dt} \right), \tag{3.8}$$

to be used in the vorticity equation addressed next. Obtained by operating $\hat{\boldsymbol{b}}_0 \cdot \boldsymbol{\nabla}_\perp \times$ on the momentum equation, the vorticity equation becomes equivalent to the *reduced shear-Alfvén law*:

$$-\rho_0 \nabla_\perp^2 \frac{D\phi}{Dt} = -B_0^2 \hat{\boldsymbol{b}} \cdot \boldsymbol{\nabla} \left(\frac{J_\parallel}{B_0} \right) + 2\hat{\boldsymbol{b}}_0 \cdot \boldsymbol{\kappa}_0 \times \left(\boldsymbol{\nabla}_\perp p + \rho_0 \frac{D\boldsymbol{v}}{Dt} \right). \tag{3.9}$$

In addition, the classic form of the reduced ideal-MHD formulation requires the ideal induction equation and the combined energy and mass conservation equation, written as

$$\frac{D\psi}{Dt} = \boldsymbol{B}_\perp \cdot \boldsymbol{\nabla}_\perp \phi, \tag{3.10}$$

$$\frac{Dp}{Dt} = \frac{\partial p}{\partial t} + (\boldsymbol{\nabla}_\perp \phi \times \hat{\boldsymbol{b}}_0) \cdot \boldsymbol{\nabla}_\perp p = 0, \tag{3.11}$$

Ohm's law will be modified from its ideal form later on, with the addition of resistivity.

Cylindrical Linearized Form

As in section 7.5 of Hazeltine and Meiss [76], the following analysis makes use of the cylindrical curvature expression

$$\boldsymbol{\kappa} \approx -\frac{B_\theta^2}{r B_0^2} \hat{\boldsymbol{e}}_r, \tag{3.12}$$

noting that strict application of the high-β ordering makes this $O(\epsilon^2)$ term negligible. It is kept in the interest of studying the effects of pressure/curvature drive in simple cylindrical geometry near marginal stability. Note that second term on the right hand side of Equation (3.9), $2\hat{\boldsymbol{b}}_0\cdot\boldsymbol{\kappa}_0\times\rho_0 D\boldsymbol{v}/Dt$, shown in Reference [76] to be associated with pressure anisotropy, becomes $O(\epsilon^4)$ in the cylindrical limit and is therefore neglected.

Linearized based on a periodic cylindrical mode structure $e^{i(m\theta-nz/R)+\gamma t}$, with $\hat{\boldsymbol{b}}_0=\hat{\boldsymbol{e}}_z$, Equations (3.9)-(3.11) above become

$$-\rho_0\gamma_D\nabla_\perp^2\phi=-iF(r)\nabla_\perp^2\psi+\frac{im}{r}J_\parallel'(r)-\frac{2B_\theta^2}{rB_0^2}\frac{im}{r}p, \tag{3.13}$$

$$\gamma_D\psi=iF(r)\phi, \tag{3.14}$$

$$\gamma_D p=-\left(\frac{im}{r}\phi\right)p'(r). \tag{3.15}$$

Here $D_t\rightarrow\gamma_D=\gamma+i\Omega$ is the Doppler shifted growth rate in the presence of slow plasma rotation $\Omega\ll\tau_A^{-1}$, and

$$F(r)\equiv\boldsymbol{k}\cdot\boldsymbol{B}=\frac{B_\theta(r)}{r}(m-nq(r)). \tag{3.16}$$

Combining the linearized equations above, we recover the form used in References [5] and [4], namely the *cylindrical* high-β reduced-MHD equation

$$\boxed{\frac{\gamma_D^2}{F(r)}\boldsymbol{\nabla}_\perp\cdot\left(\rho\boldsymbol{\nabla}_\perp\left(\frac{\psi}{F(r)}\right)\right)=-\boldsymbol{\nabla}_\perp^2\psi+\frac{mJ_\parallel'(r)}{rF(r)}\psi+\frac{m^2B_\theta^2}{r^3F^2(r)}\frac{p'(r)}{B_0^2/2}\psi}. \tag{3.17}$$

3.1 Shafranov Model: Ideal Current-Driven Instability

The Shafranov step-function cylindrical current profile with zero β [70] is useful for gaining a basic intuition for the stability of an ideal kink mode. The model uses a circular cross-section of radius 'a' and a step-function current $J_z(r)=2H(a-r)$ and plasma density $\rho(r)=\rho_0H(a-r)$, surrounded by vacuum. With a constant guide field B_0, this produces an equilibrium poloidal field distribution of

$$B_\theta(r)=B_{\theta0}\begin{cases}r, & r<a\\ a^2r^{-1}, & r>a\end{cases} \tag{3.18}$$

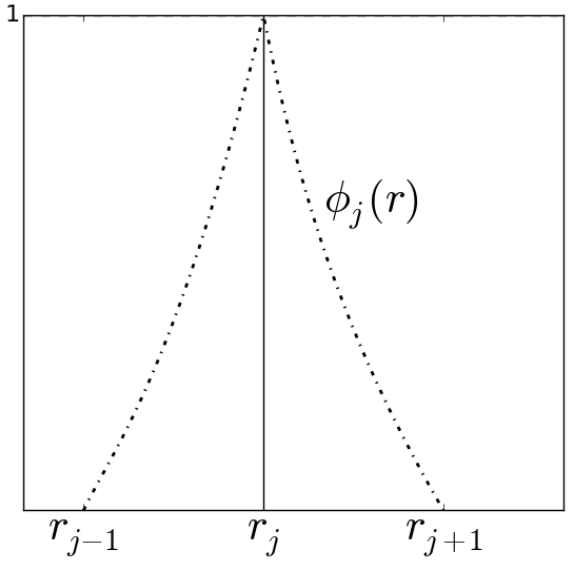

Figure 3.1: A tent-like basis function consisting of cylindrical Laplace solutions $r^{\pm m}$, used to describe a mode located at r_j with boundary conditions at r_{j-1} and r_{j+1}.

and related safety factor and $\boldsymbol{k}\cdot\boldsymbol{B}$ function are given by

$$q(r) = \begin{cases} q_0, & r < a \\ (r/a)^2 q_0, & r > a \end{cases}, \qquad F(r) = \begin{cases} m - nq_0, & r < a \\ (a/r)^2 m - nq_0, & r > a \end{cases}. \tag{3.19}$$

With ρ and F both constant for $r < a$, and $\rho = 0$ for $r > a$, the magnetic flux Equation (3.17) for a single Fourier harmonic reduces to the cylindrical Laplace equation

$$\frac{1}{r}\frac{d}{dr}\left(r\frac{d\psi}{dr}\right) - \frac{m^2}{r^2}\psi = 0, \tag{3.20}$$

almost everywhere (excluding the current step $r = a$). Using the r^m and r^{-m} solutions to the equation above, it is convenient to construct a general basis function

$$\phi_j = \begin{cases} \dfrac{(r/r_{j-1})^m - (r/r_{j-1})^{-m}}{(r_j/r_{j-1})^m - (r_j/r_{j-1})^{-m}}, & r_{j-1} < r < r_j \\ \dfrac{(r/r_{j+1})^m - (r/r_{j+1})^{-m}}{(r_j/r_{j+1})^m - (r_j/r_{j+1})^{-m}}, & r_j < r < r_{j+1} \end{cases}, \tag{3.21}$$

to describe a mode located at r_j with boundary conditions at r_{j-1} and r_{j+1}. Two special cases are the domains $(0, r_1)$ and (r_n, ∞), where the components of ϕ_j reduce to

$$\phi_1 = \begin{cases} (r/a)^m, & 0 < r < r_1 \\ \dfrac{(r/r_2)^m - (r/r_2)^{-m}}{(r_1/r_2)^m - (r_1/r_2)^{-m}}, & r_1 < r < r_2 \end{cases}, \tag{3.22}$$

and

$$\phi_n = \begin{cases} \dfrac{(r/r_{n-1})^m - (r/r_{n-1})^{-m}}{(r_n/r_{n-1})^m - (r_n/r_{n-1})^{-m}}, & r_{n-1} < r < r_n \\ (r/r_n)^{-m}, & r_n < r < \infty \end{cases}. \tag{3.23}$$

In the present case where $r_0 = 0$, $r_1 = a$ and $r_2 \to \infty$, there is only one simplified basis function describing the solution

$$\psi(r) = \psi_a \phi(r), \qquad \phi(r) = \begin{cases} (r/a)^m, & r < a \\ (r/a)^{-m}, & r > a \end{cases}. \tag{3.24}$$

Here the mode amplitude ψ_a is arbitrary since there is only a single mode. The tent-like basis function, depicted in 3.1, will become useful as additional discontinuities in ψ' are introduced to described non-ideal physics. In terms of the current-drive parameter and $F_a = \boldsymbol{k}\cdot\boldsymbol{B}(r = a)$,

$$A = \frac{2m}{F_a}, \qquad F_a = m - nq_0, \tag{3.25}$$

the current-step boundary condition is written as

$$a\psi'(a+) - \left(1 + \left(\frac{\tau_A \gamma_D}{F_a}\right)^2\right) a\psi'(a-) = -A\psi_a. \tag{3.26}$$

Here $\gamma_D = \gamma + i\Omega$ again is the Doppler shifted growth rate. Plugging the solution from Equation (3.24) into the boundary condition above, and neglecting rotation, yields the growth rate expression

$$\boxed{(\tau_A \gamma)^2 = \frac{F_a^2}{m}(A - 2m) = -2(m - nq_0)(m - 1 - nq_0)}, \tag{3.27}$$

in units of Alfvén time τ_A. This is the textbook form for a current-driven external kink mode in a cylindrical step-function profile, as expressed by Kadomtsev [75]. For $\Omega = 0$, the mode is unstable

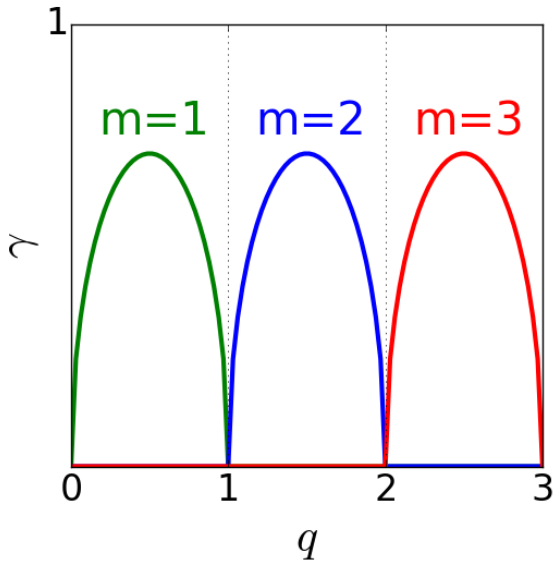

Figure 3.2: Growth rate 'domes' of the ideal current-driven external kink versus edge safety factor, for fixed toroidal harmonic $n = 1$ and different poloidal m-harmonics in a cylindrical current-step system.

for positive growth rate $\gamma > 0$, which occurs in the range

$$m - 1 < nq_0 < m, \tag{3.28}$$

as depicted by the ideal 'domes' in Figure 3.2, for fixed $n = 1$ and different m numbers. In Reference [70], Shafranov shows additionally that if the step-function current is replaced with a smoothly decreasing current profile, the amplitude of the growth rate decreases as m increases, with gaps of stability between each ideal dome, implying that the most dangerous instabilities in this cylindrical formulation are the low-m ideal kink modes. The stability limits, given by the point of marginal stability $\gamma = 0$, are described simply by $nq_0 < m - 1$ from below and $nq_0 > m$ from above.

3.2 Ideal High-β Instability Driven by Both Current and Pressure

Finite pressure always adds a destabilizing effect to the ideal kink. This can be observed by adding a pressure step coinciding with the current step, so that the drive term in Equation 3.17 now includes

both a current-drive A (Equation (3.25)) and a pressure-drive $B\beta$ term, given by

$$A = \frac{2m}{F_a}, \qquad B = \frac{m^2}{F_a^2}. \tag{3.29}$$

With a combined current/pressure step-function profile, the form of the solution is the same as in the previous section. The resulting growth rate

$$\boxed{(\tau_A \gamma_D)^2 = \frac{F_a^2}{m}\left(A + B\beta - 2m\right) = -2(m - nq_0)(m - 1 - nq_0) + m\beta}, \tag{3.30}$$

is destabilized with increasing $\beta \equiv 2p_0/B_0^2$. Taking zero rotation and a safety factor $nq_0 < m - 1$ that corresponds to a stable equilibrium at $\beta = 0$, and increasing β until $\gamma = 0$ reveals the β-limit for a current and pressure driven ideal external kink mode, which we will refer to as the *non-resonant no-wall* limit:

$$\boxed{\beta_{nr-nw} = \frac{1}{B}\left(-A + 2m\right) = \frac{2}{m}(m - nq_0)(m - 1 - nq_0)}. \tag{3.31}$$

Non-resonant here refers to the absence of resonant plasma surfaces, to be included later on. As shown by Finn [52], the relation between the β-limit and q_0 is analogous to the zero-β marginal stability condition in Equation (3.28). The β-limit curves for each m-number are the inverse of the domes observed in Figure 3.2.

3.3 Current/Pressure Step Surrounded by a Resistive Wall

As discussed in Chapter 2, the addition of a conducting wall slows the growth of the external ideal kink. In the case of a perfectly conducting wall, the mode can be stabilized up to a higher β-limit. With the inclusion of resistivity, the induced eddy currents in the wall can decay on the L/R time of the wall, thus allowing the mode to grow. A major benefit of the reduced-MHD formulation is the convenient addition of physics through boundary conditions. A thin conducting layer with dissipation time τ_w and radius r_w outside of the plasma requires that

$$\left[\frac{r\psi'}{\psi}\right]_{r_{w-}}^{r_{w+}} = \gamma\tau_w, \tag{3.32}$$

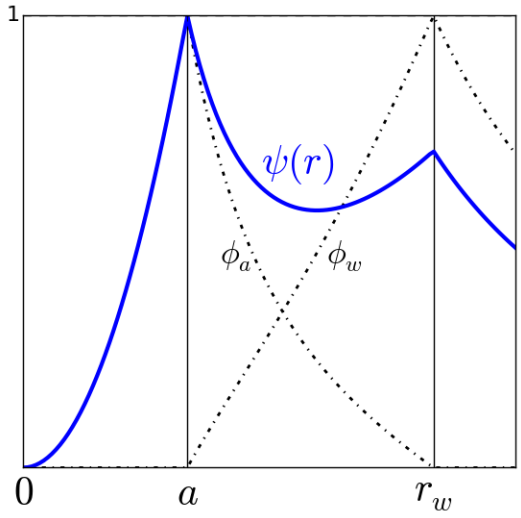

Figure 3.3: The flux distribution $\psi(r)$ (solid blue line) expressed as a linear combination of two tent-like basis functions: $\psi = \alpha_a \phi_a(r) + \alpha_w \phi_w(r)$.

in addition to the plasma current/pressure step boundary condition in Equation (3.26). Note that the wall growth rate is not Doppler shifted since the wall is stationary. With two boundary conditions, we use the tent-like basis function defined in Equation (3.21) to express the solution as

$$\psi = \psi_a(r) + \psi_w(r) = \alpha_a \phi_a(r) + \alpha_w \phi_w(r), \tag{3.33}$$

in terms of two mode amplitudes α_a and α_w. This basis set is depicted in Figure 3.3. In order to later make use of this tent function basis method in more complicated systems, we define several geometric factors that will be repeated. The positively defined geometric coupling factors are

$$R_k^+ \equiv (r_k/r_{k+1})^m + (r_k/r_{k+1})^{-m}, \tag{3.34}$$

$$R_k^- \equiv (r_k/r_{k+1})^m - (r_k/r_{k+1})^{-m}, \tag{3.35}$$

defining the positive geometric coupling between radius r_k and the next neighboring radius r_{k+1}, going radially outward. In the case where $r_{k+1} \to \infty$, we get the simplification $R_k^+/R_k^- \to 1$. Next we use these to define the self-inductance and mutual inductance expressions used by Brennan and

Finn [4] to describe changes in components of ψ':

$$\delta_j \equiv \left[r\phi_j'\right]_{r_j-}^{r_j+}, \tag{3.36}$$

$$k_{j,j+1} \equiv -r\phi_j'(r_{j+1}) > 0, \tag{3.37}$$

$$k_{j+1,j} \equiv r\phi_{j+1}'(r_j) > 0. \tag{3.38}$$

In the present system, these geometric coupling and inductance factors are given by

$$R_a^+ \equiv (r_w/a)^m + (r_w/a)^{-m}, \tag{3.39}$$

$$R_a^- \equiv (r_w/a)^m - (r_w/a)^{-m}, \tag{3.40}$$

and

$$\delta_a = -m\left(\frac{R_a^+}{R_a^-} + 1\right) = \delta_w, \tag{3.41}$$

$$k_{aw} = \frac{2m}{R_a^-} = k_{wa}. \tag{3.42}$$

Now plugging the expression for the perturbed flux in Equation (3.33) into the boundary conditions in Equations (3.26) and (3.32) yields a coupled dispersion relation

$$\begin{bmatrix} \Delta_A - \frac{m}{F_a^2}(\gamma_D\tau_A)^2 & L_{wa} \\ L_{aw} & \Delta_w - \gamma\tau_w \end{bmatrix} \begin{bmatrix} \alpha_A \\ \alpha_w \end{bmatrix} = 0. \tag{3.43}$$

In terms of the self and mutual inductance factors defined above, the matrix coefficients are given by

$$\Delta_a = A + B\beta + \delta_a, \qquad L_{wa} = k_{wa}, \tag{3.44}$$

$$L_{aw} = k_{aw}, \qquad \Delta_w = \delta_w. \tag{3.45}$$

While there is only one combined least stable mode, the system in this form can be interpreted as a set of coupled modes, with the modes defined on the diagonal and the mode-coupling resulting from the off-diagonal terms. The first 'mode' is the ideal plasma mode (or conjugate pair including a stable and unstable root) characterized by the Alfvén time τ_A, similar to the no-wall expression

in Equation (3.30). The second 'mode' is a wall mode characterized by the wall time τ_w. For comparison with Equation (3.30), we take the determinant of the matrix above, arriving at a cubic dispersion relation

$$(\tau_A\gamma_D)^2 = \frac{F_a^2}{m}\left(\Delta_a - \frac{L_{aw}L_{wa}}{\Delta_w - \gamma\tau_w}\right) = \frac{F_a^2}{m}\left(A + B\beta + \delta_a - \frac{k_{aw}k_{wa}}{\delta_w - \gamma\tau_w}\right). \tag{3.46}$$

Note that near marginal stability ($\gamma = 0$), with no rotation, $\tau_A^2\gamma^2 \ll \tau_w\gamma$ implies that the dispersion relation is governed by the wall time and hence that the inertial term $\tau_A^2\gamma^2$ can be neglected. Setting $\gamma = 0$ leads to the marginal stability condition

$$\Delta_a\Delta_w - L_{aw}L_{wa} = 0. \tag{3.47}$$

Note that this condition is independent of the inertial time τ_A as well as the wall time τ_w. In the absence of plasma rotation, these timescales affect the growth rate of the mode but not the stability limit. From the expression above we obtain the *non-resonant resistive-wall* β-limit

$$\boxed{\beta_{nr-rw} = \frac{1}{B}\left(-A + \left[\frac{k_{aw}k_{wa}}{\delta_w} - \delta_a\right]\right) = \frac{1}{B}\left(-A + 2m\right) = \beta_{nr-nw}}. \tag{3.48}$$

In the absence of rotation, we find that the non-resonant resistive-wall limit is identical to the non-resonant no-wall limit found in Equation (3.31). The *non-resonant ideal-wall* condition is obtained by taking $\tau_w \to \infty$ before setting $\gamma = 0$. This eliminates the wall 'mode' amplitude ($\alpha_w = 0$), resulting in

$$\boxed{\beta_{nr-iw} = \frac{1}{B}\left(-A - \delta_a\right) = \frac{1}{B}\left(-A + 2m\frac{1}{1-(a/r_w)^{2m}}\right)}. \tag{3.49}$$

When $r_w \to \infty$, the expression above reduces to the non-resonant no-wall β-limit in Equation (3.31) (or equivalently to the non-resonant resistive-wall β-limit in Equation (3.48)). For finite ideal wall radius $a < r_w < \infty$, the factor that multiplies the $2m$ in the expression above is greater than unity, implying that the effect of the ideal wall is to raise the β-limit. The non-resonant ideal-wall β-limit increases as the wall approaches the plasma. In this simplified cylindrical model, bringing the wall all the way up to the plasma surface ($r_w \to a$) completely stabilizes the mode, that is the $\beta_{nr-iw} \to \infty$.

In order to additionally capture the effect of a tearing instability in a relatively simple formulation, the next section extends this system with a resistive resonant plasma layer.

3.4 3-Layer Finn Model: Current/Pressure Step, Tearing Layer, Resistive Wall

The high-β model was extended by Finn [5, 52] to include a resistive plasma between the current/-pressure step and the wall. At a resonant surface, a tearing layer introduces yet another timescale τ_t. This additional layer introduces a boundary condition similar to that of the thin resistive wall:

$$\left[\frac{r\psi'}{\psi}\right]_{r_{w-}}^{r_{w+}} = \gamma\tau_w, \tag{3.50}$$

$$\left[\frac{r\psi'}{\psi}\right]_{r_{t-}}^{r_{t+}} = \gamma_D\tau_t, \tag{3.51}$$

The jump across the tearing layer is characterized in general by a parameter $\Delta(\gamma, \tau_t)$ which depends upon the layer physics. Different tearing regimes are discussed in detail in a paper by Cole and Fitzpatrick [77]. The present formulation considers a typical regime known as the constant-ψ visco-resistive regime [50, 51]. In this form the tearing layer condition conveniently reduces to the same form as the thin wall condition, except that the growth rate $\gamma_D = \gamma + i\Omega$ is Doppler shifted due to bulk plasma flow in the axial direction. Here $\Omega = \boldsymbol{k}\cdot\boldsymbol{v} = k_z v_z$ is the cylindrical equivalent to toroidal rotation. Another important difference between the tearing condition and the wall condition will appear in multi-mode calculations in shaped toroidal geometry, where the jump across the tearing layer affects only the resonant component of the perturbed field, in contrast with the wall which affects all harmonic components.

Neglecting inertia at the outset, since we are primarily interested in the stability limits, the current/pressure step condition from Equation (3.26) reduces to the compact form

$$\left[\frac{r\psi'}{\psi}\right]_{a_-}^{a_+} = -(A + B\beta) \tag{3.52}$$

With a constant safety factor q_0 inside the current/pressure step, the q-profile in the vacuum increases quadratically as in Equation (3.19). Thinking of the vacuum region up to the wall as a cold plasma extending beyond the bulk equilibrium current, the tearing radius is set according to the resonant condition $q(r) = m/n$, resulting in

$$r_t = a\sqrt{\frac{m}{nq_0}}. \tag{3.53}$$

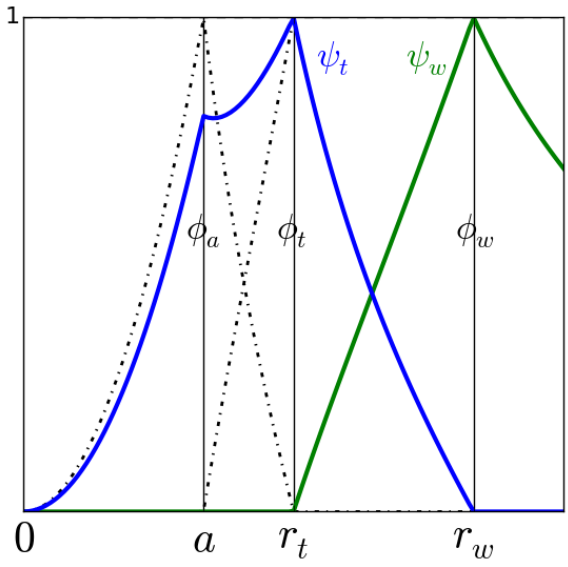

Figure 3.4: A basis of tent functions for the three-layer model; current/pressure step a with separate tearing layer r_t and resistive-wall r_w.

A resistive-plasma resistive-wall dispersion relation is now derived and evaluated by formulating the problem as a system of two coupled modes; a resistive wall mode (RWM) having finite flux at the wall and zero flux at the tearing layer, and a tearing mode (TM) have finite flux at the resistive plasma layer and zero flux at the wall. It should be emphasized, however, that this approach allows both phenomena to coexist, to each dominate different domains of the MHD parameter space, and to become coupled when their timescales are comparable.

The two dissipative boundary conditions in Equations (3.32) and (3.51) motivate a description of the flux function as a superposition of a tearing mode ψ_t and a wall mode ψ_w, as

$$\psi(r) = \alpha_t \psi_t(r) + \alpha_w \psi_w(r), \tag{3.54}$$

where the constants α_t and α_w are the mode amplitudes. Using the tent function form defined in Equation (3.21), the tearing and wall modes are expressed in a basis of three tent functions

$$\psi_t = c_a \phi_a(r) + \phi_t(r), \tag{3.55}$$

$$\psi_w = \phi_w(r), \tag{3.56}$$

corresponding to the three boundary conditions in Equations (3.32), (3.51) and (3.52). This basis is depicted in Figure 3.4. The third amplitude parameter c_a is required to span the solution space with three boundary conditions. As in the previous section, we use Equations (3.36)-(3.38) to define concise expressions for the self-inductance and mutual-inductance parameters

$$\delta_a \equiv [r\phi_a']_{a-}^{a+} = -m\left(\frac{R_a^+}{R_a^-} + 1\right), \tag{3.57}$$

$$\delta_t \equiv [r\phi_t']_{r_t-}^{r_t+} = -m\left(\frac{R_t^+}{R_t^-} + \frac{R_a^+}{R_a^-}\right), \tag{3.58}$$

$$\delta_w \equiv [r\phi_w']_{r_w-}^{r_w+} = -m\left(1 + \frac{R_t^+}{R_t^-}\right), \tag{3.59}$$

$$k_{at} \equiv -(r\phi_a')_{r_t-} = m\frac{2}{R_a^-} = (r\phi_t')_{a+} \equiv k_{ta}, \tag{3.60}$$

and

$$k_{tw} \equiv -(r\phi_t')_{r_w} = m\frac{2}{R_t^-} = (r\phi_w')_{r_t} \equiv k_{wt}. \tag{3.61}$$

Here we have made use of the R^+ and R^- notation defined in Equations (3.34) and (3.35). Plugging the perturbed flux function, in its tent function basis form, into the three boundary conditions in Equations (3.50)-(3.52) yields a dispersion relation

$$\begin{bmatrix} \Delta_t - \gamma_D\tau_t & L_{wt} \\ L_{tw} & \Delta_w - \gamma\tau_w \end{bmatrix} \begin{bmatrix} \alpha_t \\ \alpha_w \end{bmatrix} = 0, \tag{3.62}$$

similar to the previous section dispersion relation in Equation (3.43), but now describing a mode that consists of a tearing component and a wall component. The diagonal coefficients describe the separate tearing 'mode' and wall 'mode' components

$$\Delta_t \equiv [r\psi_t']_{r_t-}^{r_t+} = \frac{-k_{ta}k_{at}}{\delta_a + A + B\beta} + \delta_t, \qquad \Delta_w \equiv [r\psi_w']_{r_w-}^{r_w+} = \delta_w, \tag{3.63}$$

and the off-diagonal components describing the tearing-wall coupling

$$L_{tw} \equiv (-r\psi_t')_{r_w-} = k_{tw}, \qquad L_{wt} \equiv (r\psi_w')_{r_t+} = k_{wt}. \tag{3.64}$$

The eigenvalues are found by equating the determinant to zero, and are thus independent of the

basis amplitudes α_t and α_w:

$$\boxed{\gamma^2 + \left(-\frac{\Delta_t}{\tau_t} - \frac{\Delta_w}{\tau_w} + i\Omega\right)\gamma + \frac{1}{\tau_t\tau_w}\left(\Delta_t\Delta_w - L_{tw}L_{wt} - i\Omega\tau_t\Delta_w\right) = 0}. \tag{3.65}$$

The relevant growth rate for the stability limit is the most positive eigenvalue, corresponding to the least stable mode.

Analytic β Limits at Zero Rotation

The stability limits are found by solving the dispersion relation in Equation (3.65) with $\gamma = 0$. For finite τ_t and τ_w, and no rotation ($\Omega = 0$), the marginal stability condition

$$\Delta_t\Delta_w - L_{tw}L_{wt} = 0, \tag{3.66}$$

results in the resistive-plasma resistive-wall β-limit

$$\boxed{\beta_{rp-rw} = \frac{1}{B}\left(-A - \delta_a + \frac{k_{ta}k_{at}\delta_w}{\delta_t\delta_w - k_{tw}k_{wt}}\right)}. \tag{3.67}$$

Returning to Equation (3.65), the resistive-plasma ideal-wall condition is obtained by taking $\tau_w \to \infty$ before setting $\gamma = 0$, keeping finite τ_t and $\Omega = 0$. We obtain the condition

$$\Delta_t = 0, \tag{3.68}$$

resulting in the resistive-plasma ideal-wall limit

$$\boxed{\beta_{rp-iw} = \frac{1}{B}\left(-A - \delta_a + \frac{k_{ta}k_{at}}{\delta_t}\right)}. \tag{3.69}$$

which depends on the coupling to the tearing layer. In the ideal-plasma resistive-wall limit $\tau_t \to \infty$ (with finite τ_t), on the other hand, the condition $\Delta_w = 0$ analogous to Equation (3.68) provides no β-limit since Δ_w in Equation (3.63) is independent of β. This means that in the 3-layer model, there is no β-drive on the wall mode in the ideal-plasma limit. The ideal-plasma β-limit occurs when

$$\Delta_t \to \infty, \tag{3.70}$$

independently of the wall. Since the resonant plasma layer in this model separates the driving current/pressure step from the wall, an ideal-plasma boundary condition $\psi = 0$ completely decouples the wall from the plasma. The resulting ideal-plasma limit is given independently of the wall properties by

$$\boxed{\beta_{ip-rw} = \beta_{ip-iw} = \frac{1}{B}\left(-A - \delta_a\right)}, \tag{3.71}$$

describing both the ideal-plasma resistive-wall and the ideal-plasma ideal-wall limits.

While these cylindrical single-mode models are meant to develop an intuition for the nature of the different β-limits, it is important to keep in mind that in more realistic geometry the tearing and resistive-wall instabilities are both driven and geometrically coupled through a spectrum of harmonics, thus causing the ideal-plasma limits to depend on wall properties such as conductivity and position. As will be seen in the multi-mode sharp-boundary calculations, all four β limits exist despite the similar setup with the resonant layer in between the driving current/pressure layer and the wall. The next section compares the β-limits of the 3-layer model with a *4-layer* model by Brennan and Finn [4], which introduces a pressure jump in between the resonant layer and the wall (separate from the current jump) in order to guarantee that, even in cylindrical geometry, the wall mode is driven in the ideal-plasma limit. This double-step equilibrium profile can be thought of as a proxy for the multi-harmonic coupling that occurs in shaped toroidal geometry.

3.5 4-Layer Brennan-Finn Model: Current Step, Tearing Layer, Pressure Step, Resistive Wall

In the previous section, we demonstrated how a tearing layer located outside of the current/pressure driving layer completely decouples the wall from the current/pressure-drive in the ideal plasma limit ($\tau_t \to \infty$). In that case the ideal-plasma limit is independent of wall properties (conductivity and position). In order to produce distinct β_{ip-rw} and β_{ip-rw} limits in a cylindrical formulation, the version by Brennan and Finn [4], referred to here as the *4-layer* model, includes four distinct boundary conditions, located (going radially outward) at the current-step a_1, tearing layer r_t, pressure-step a_2 and resistive wall r_w.

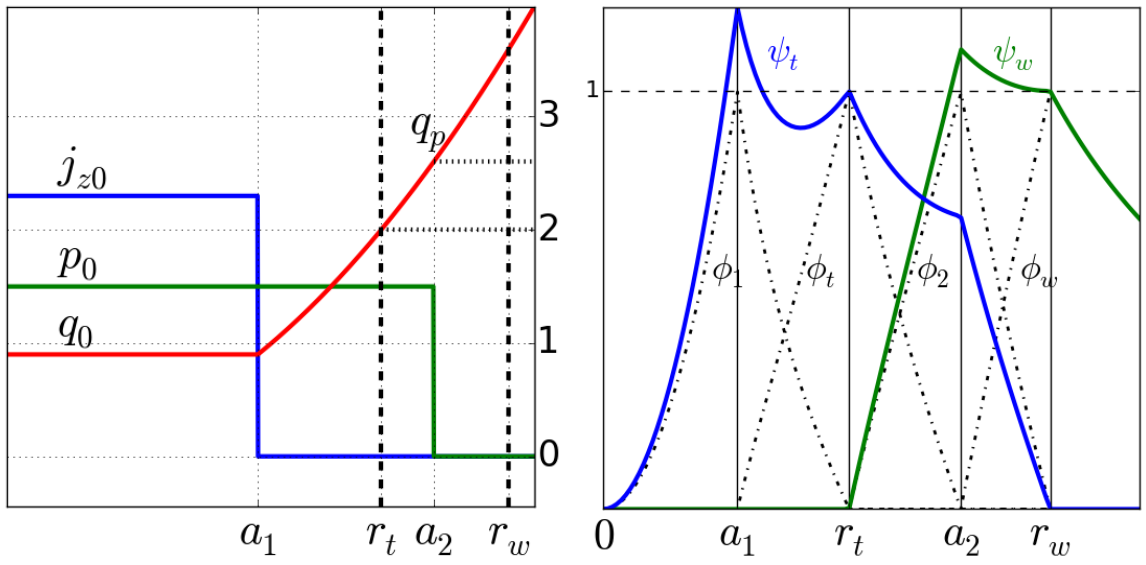

(a) (b)

Figure 3.5: (a) The Brennan-Finn double-step equilibrium with tearing layer and resistive wall. (b) A basis of tent functions for the Brennan-Finn 4-layer model; current step a_1, tearing layer r_t, pressure step a_2 and resistive-wall r_w. This 4-layer profile is designed to provide coupling to the wall mode, despite the cylindrical single-mode analysis, in the ideal-plasma limit.

The double-step profile, depicted in Figure 3.5a, requires four boundary conditions

$$\left[\frac{r\psi'}{\psi}\right]_{a_{1-}}^{a_{1+}} = -A, \qquad \left[\frac{r\psi'}{\psi}\right]_{a_{2-}}^{a_{2+}} = -B\beta, \tag{3.72}$$

$$\left[\frac{r\psi'}{\psi}\right]_{r_{t-}}^{r_{t+}} = \gamma_D \tau_t, \qquad \left[\frac{r\psi'}{\psi}\right]_{r_{w-}}^{r_{w+}} = \gamma \tau_w. \tag{3.73}$$

As in the 3-layer model, the perturbed flux is written as a superposition of a tearing and a wall mode as $\psi(r) = \alpha_t \psi_t(r) + \alpha_w \psi_w(r)$, and each boundary condition has a corresponding tent-like basis function to span the solution space:

$$\psi_t(r) = c_1\phi_1(r) + \phi_t(r) + c_2\phi_2(r), \tag{3.74}$$

$$\psi_w(r) = c_3\phi_2(r) + \phi_w(r). \tag{3.75}$$

The general form of the j_{th} tent-like basis function ϕ_j is defined in Equation (3.21). In the notation of Brennan and Finn, $r_1 = a_1$, $r_2 = r_t$, $r_2 = a_2$, $r_3 = r_w$ and $r_4 = r_c$. The corresponding basis of four tent functions is depicted in Figure 3.5b. The three constants c_1, c_2, c_3 are determined by the

current and pressure boundary conditions in Equation (3.72), which becomes three conditions due to the independence of α_t and α_w. The self and mutual inductance terms are defined in the same notation as in Equations (3.57)-(3.61) of the previous section. With the groundwork laid out above, it is straightforward to express the dispersion coefficients

$$\Delta_t \equiv [r\psi_t']_{r_t-}^{r_t+} = c_1 k_{1t} + \delta_t + c_2 k_{2t}, \tag{3.76}$$

$$\Delta_w \equiv [r\psi_w']_{r_w-}^{r_w+} = c_3 k_{2w} + \delta_w, \tag{3.77}$$

$$L_{tw} \equiv -r_w \psi_t'(r_{w-}) = c_2 k_{2w}, \tag{3.78}$$

$$L_{wt} \equiv r_t \psi_w'(r_{t+}) = c_3 k_{2t}, \tag{3.79}$$

in terms of the basis function amplitudes

$$c_1 = \frac{-k_{t1}}{A+\delta_1}, \qquad c_2 = \frac{-k_{t2}}{B\beta+\delta_2}, \qquad c_3 = \frac{-k_{w2}}{B\beta+\delta_2}. \tag{3.80}$$

Once again the growth rate is found by solving the quadratic dispersion relation in Equation (3.65).

Analytic β Limits at Zero Rotation

We follow the same process as in the previous section to determine the stability limits. Starting with the resistive-plasma resistive-wall β-limit, setting $\gamma = 0$ for finite values of τ_t and τ_w and $\Omega = 0$ leads to the condition $\Delta_t\Delta_w - L_{tw}L_{wt} = 0$, resulting in the limit

$$\boxed{\beta_{rp-rw} = \frac{1}{B}\left[-\delta_2 + \frac{k_{w2}k_{2w}\left(\delta_t - \frac{k_{t1}k_{1t}}{A+\delta_1}\right) + k_{t2}k_{2t}\delta_w}{\delta_w\left(\delta_t - \frac{k_{t1}k_{1t}}{A+\delta_1}\right)}\right]}. \tag{3.81}$$

Next, taking $\tau_w \to \infty$ with finite τ_t, the resulting condition $\Delta_t = 0$ produces the resistive-plasma ideal-wall limit

$$\boxed{\beta_{rp-iw} = \frac{1}{B}\left(-\delta_2 + \frac{k_{t2}k_{2t}}{\delta_t - \frac{k_{t1}k_{1t}}{A+\delta_1}}\right)}. \tag{3.82}$$

Now taking $\tau_t \to \infty$, keeping τ_w finite, produces a similar condition $\Delta_w = 0$ and a corresponding ideal-plasma resistive-wall limit

$$\boxed{\beta_{ip-rw} = \frac{1}{B}\left(-\delta_2 + \frac{k_{w2}k_{2w}}{\delta_w}\right)}. \tag{3.83}$$

We emphasize that in the 4-layer version of Brennan and Finn, the rp-iw and ip-rw limits are generated by similar conditions $\Delta_t = 0$ and $\Delta_w = 0$, respectively, because the pressure step outside of the resonant plasma layer independently drives an instability at the wall. Now taking both $\tau_w \to \infty$ and $\tau_t \to \infty$, the condition $\Delta_w, \Delta_t \to \infty$ produces a distinct ideal-plasma ideal-wall limit

$$\boxed{\beta_{ip-iw} \to \frac{-\delta_2}{B}}. \tag{3.84}$$

3.6 4-β Limit Ordering Transitions due to Wall Position and Safety Factor

Reference [4] used the fixed radii $a_1 = 0.5$, $a_2 = 0.8$ and $r_w = 1$, and selected the values $q_0 = 0.9$, $m = 2$ and $n = 1$ to drive a strong tearing response at $r_t = a_1\sqrt{m/nq_0} = 0.79$. The dissipation times $\tau_w = 10^3$ and $\tau_t = 10^4$ (in Alfvén time units) were selected to be sufficiently close for coupling on a similar timescale but distinct enough to differentiate the TM from the RWM. Initially rotation is set to zero. Plotting the growth rate for the four combinations of finite or very large (scaled by 10^8) dissipation times produces the curves shown in Figure 3.6, with crossings from stable $\gamma < 0$ to unstable $\gamma > 0$ at four distinct β values. Note the following convention which will continue throughout this work: The dashed versus solid line denotes a resistive-plasma versus ideal-plasma, while blue versus red denotes a resistive-wall versus ideal-wall. It is important to keep in mind that, with no plasma rotation, each of the four β limits is independent of the actual values of the dissipation times. In order to understand how mode transitions occur, Figures 3.7a and 3.7b gradually increase τ_w and τ_t, respectively, with the other timescale fixed. It is clear that while the growth rates change with the dissipation times, the point of marginal stability is fixed for any finite dissipation time. Only as the dissipation time becomes very large, there is a sharp knee in the growth rate curve and a matching knee of the stable eigenvalue that rises to join it. In the limit of an infinite dissipation time, meaning a perfect shielding condition, the two knees form a continuous

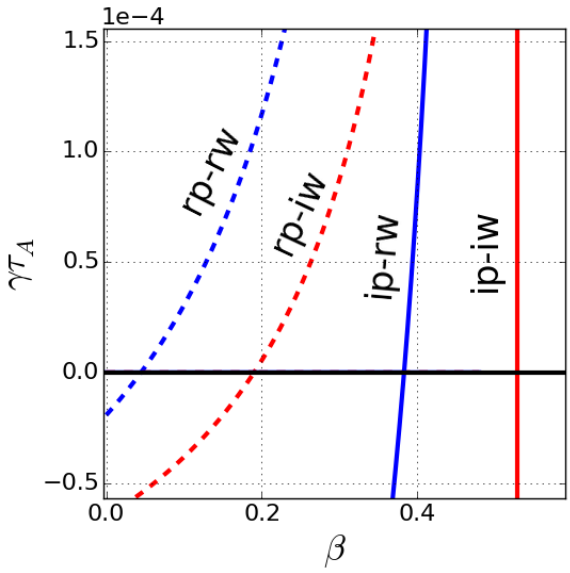

Figure 3.6: Brennan-Finn 4-layer model growth rates of the four modes, with $a_1 = 0.5$, $a_2 = 0.8$, $r_w = 1$, $q_0 = 0.9$, $m = 2$, $n = 1$ and $r_t = a_1\sqrt{m/nq_0} = 0.79$. The resistive timescales are $\tau_w = 10^3$ and $\tau_t = 10^4$, and the ideal timescales are $\tau_w = 10^{11}$ and $\tau_t = 10^{12}$.

line, which is also independent of the actual dissipation times.

While in reality neither plasma nor wall is perfectly conducting, the higher stability limits provide important information about rp-rw mode stabilizability under the influence of rotation or feedback control. For example Figure 3.8 shows how rotation raises the rp-rw β-limit up to the rp-iw limit. As discussed in the previous chapter, this stabilizing effect can be attributed to a Doppler shift between the TM and the RWM. When the plasma is stationary, perturbations penetrate the wall as the wall eddy currents decay. As the plasma rotates, the perturbation becomes out of phase with the decaying eddy currents, effectively extending the wall decay time in the plasma frame.

The β-limit ordering associated with the typical Brennan-Finn parameters,

$$\beta_{rp-rw} < \beta_{rp-iw} < \beta_{ip-rw} < \beta_{ip-iw} \tag{3.85}$$

implies that the rp-rw limit can be raised by rotation up to the rp-iw limit. However, if the wall radius r_w is brought close enough to the plasma, the rp-iw limit may become higher than the ip-rw limit. Raising q_0 in this model can have a similar effect. In this case the rotational stabilization of the rp-rw mode is bounded by the ip-rw limit. Figure 3.9 demonstrates the $r_w - q_0$ parameter space

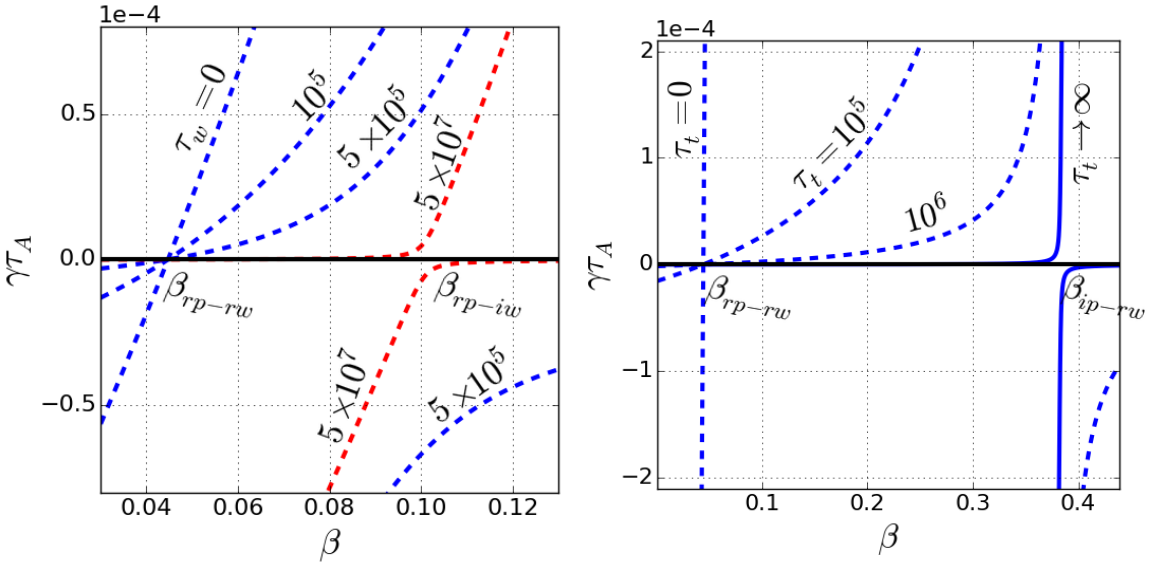

Figure 3.7: Mode transition of rp-rw to (a) rp-iw by taking large τ_w and to (b) ip-rw by taking large τ_t. Up to the mode transition, the points of marginal stability are independent of the dissipation times. (Dashed: resistive-plasma. Solid: ideal-plasma. Blue: resistive-wall. Red: ideal-wall)

associated with the different orderings $\beta_{rp-iw} < \beta_{ip-rw}$ and $\beta_{rp-iw} < \beta_{ip-rw}$. Here $q_p = q(a_2)$, the safety factor at the pressure step, is also shown for comparison with the internal (current-step) safety factor $q_0 = q(a_1)$. The two domains are determined analytically by the expression

$$\beta_{rp-iw} = \boxed{\frac{1}{B}\frac{k_{t2}k_{2t}}{\delta_t - \frac{k_{1t}k_{t1}}{A+\delta_1}} = \frac{1}{B}\frac{k_{2w}k_{w2}}{\delta_w}} = \beta_{ip-rw}. \tag{3.86}$$

As discussed in the previous chapter, rotational stabilization requires dissipation in both the plasma and the wall, and is shown above to be generally bounded by the first ideal limit; either the rp-iw or ip-rw limit. In this way the ideal β-limits characterize the rotationally stabilizable domain. This key observation will be further explored in the context of the sharp-boundary model, where similar transitions in the β-limit ordering are found to be induced by plasma shaping.

The study by Brennan and Finn [4] showed good qualitative agreement between these analytically derived limits of the reduced-MHD model and a full resistive-MHD code (both in cylindrical geometry). Thus the reduced-MHD formulation with a step-function profile is a useful tool for developing a qualitative intuition for the physics of MHD stability limits in the presence of plasma and

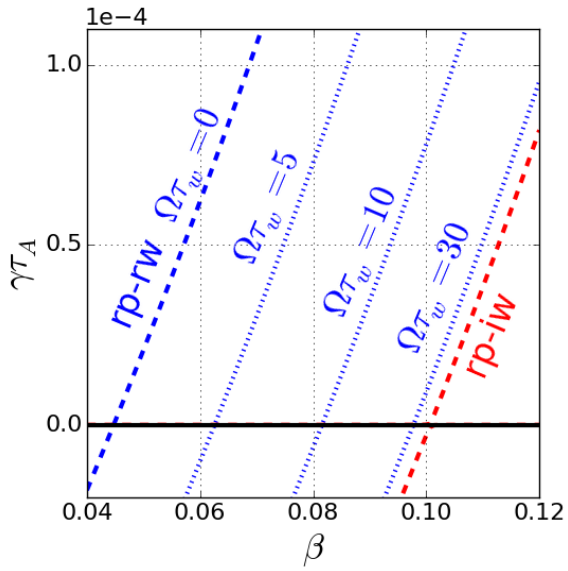

Figure 3.8: The rp-rw β-limit is increased by rotation up to the rp-iw limit.

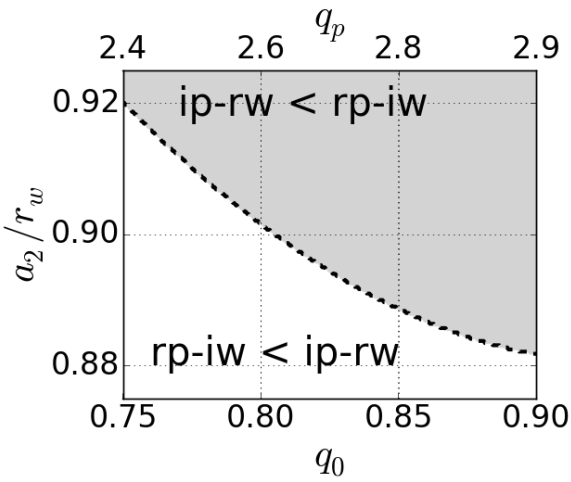

Figure 3.9: The $r_w - q_0$ parameter space associated with the different β-limit orderings.

wall resistivity. We emphasize again that this unified approach to MHD instabilities encompasses a combination of tearing and wall properties, both of which can play a part in the least stable mode limit. As discussed in the previous chapter, rotational stabilization is a general effect exhibited in the presence of wall resistivity and a variety of dissipative plasma properties including sound wave damping [33], resistivity [5, 34] and viscosity [35, 36], as well as kinetic effects such as the resonance between mode rotation and the precession drift frequency of trapped particles [38, 39]. The key

feature of all of these systems is the generation of two coupled roots in the complex plane, which destabilize the system through coupling when the wall and plasma phenomena occur on comparable timescale, and can become stabilized by the decoupling effect of plasma rotation with respect to the wall.

As shown above, setting a pressure step between the tearing layer and the wall guarantees coupling to the wall mode even in the ideal plasma limit, despite the cylindrical single-harmonic configuration. The next chapter first introduces a *2-layer* version in which the current-step, pressure-step and tearing layer are all combined, maintaining a resistive wall outside. In this degenerate formulation the mode is completely stabilized in the ideal-plasma limit, similar to the case of a close-in ideal wall derived in Section 3.3 above. The 2-layer version is then extended with *toroidal curvature* which geometrically couples two different Fourier harmonics, allowing the non-resonant harmonic to penetrate the resonant layer and to thus couple to the wall even in the limit of an ideal-plasma limit.

Chapter 4

Toroidal Extension of the Reduced-MHD Model

This chapter provides an analytic basis for understanding the effects of geometric mode-coupling in a system with both plasma and wall resistivity. In the reduced-MHD model presented in the previous chapter, the stability analysis of a perturbation with a single Fourier harmonic reduces to two coupled resistive layers, namely the tearing layer and the wall. The perturbations are driven unstable by the equilibrium current gradient and pressure gradient.

We begin this chapter by introducing a 2-layer cylindrical model and compare its β-limits with those obtained in the previous chapter for the 3-layer (Finn [5]) and 4-layer (Brennan-Finn [4]) cylindrical models. Starting with a the 3-layer model profile with a combined current/pressure step, tearing layer and a resistive wall, the 2-layer model is obtained by approximating the tearing layer to be just outside of the current/pressure step, while fixing the safety factor at both the current/pressure step (q_0) and the tearing radius ($q(r_t) = m/n$) to avoid a resonant singularity. This change in the model is motivated by the sharp-boundary model presented in the next chapter, where taking $r_t \to a_+$ conveniently reduces the number of integration regions. This setup with $r_t \to a_+$ imitates the situation in a real diverted plasma where $q \to \infty$ sharply at the diverted surface as many resonant layers are packed closely together. In a circular cylinder, the degenerate combination of the current/pressure step with the tearing layer just outside leads to an infinite β-limit when the plasma is ideal ($\tau_t \to \infty$). A similar effect is observed in the previous chapter example

(Section 3.3) of a perfectly conducting wall close to the plasma, with no intermediate vacuum region. In toroidal geometry, an ideal resonant layer only shields its corresponding resonant harmonic, unlike a perfectly conducting wall, allowing other components of the mode to grow.

This chapter presents an extended 2-mode model which incorporates first-order toroidal curvature that geometrically couples two poloidal mode harmonics. We use this extended model to show analytically that the addition of toroidal curvature introduces two finite ideal-plasma limits (ip-rw and ip-iw). These two finite limits are attributed to the harmonic coupling introduced in non-cylindrical geometry. The finiteness is due to β-drive on the non-resonant component of the mode. The formulation of the toroidal curvature and the resulting sideband harmonic coupling is based on unpublished notes by J. M. Finn, reminiscent of coupled tearing mode theory such as the work of Connor et. al. [78]. The setup is designed to include the minimal features required to analytically evaluate how the β-limits are affected by geometric mode-coupling, which is a central topic in this thesis.

4.1 2-Layer Model: Current/Pressure/Tearing Layer and a Resistive Wall

We begin with a cylindrical formulation, which will be referred to as the *2-layer* model, modifying the 3-layer model of the previous chapter (Section 3.4). Recall that the tearing layer radius in the 3-layer model is located at rational values of the safety factor $q(r_t) = m/n$. A quadratic profile beyond the current-step resulted in $r_t = a\sqrt{m/(nq_0)}$, with q_0 being the safety factor at the current step. In the present 2-layer version, in order to separate qualitative effect of the tearing layer physics from the model q-profile, the tearing layer is set just outside of the plasma edge

$$r_t \to a_+. \tag{4.1}$$

Taking the corresponding limit $\psi'(r_{t-}) \to \psi'(a_+)$ allows the tearing boundary condition above and the current/pressure step boundary condition (3.26) to be combined:

$$\begin{aligned}\Delta_t &= \psi'(r_{t+}) - \psi'(r_{t-}) \\ &= \psi'(r_{t+}) - \psi'(a_+) \\ &= \psi'(r_{t+}) - [\psi'(a_-) - (A + B\beta)] \\ &= \delta_{at} + A + B\beta, \end{aligned} \tag{4.2}$$

where

$$\delta_{at} \equiv [\psi']_{a_-}^{r_{t+}} \tag{4.3}$$

In addition we require the resistive wall boundary condition

$$\left[\frac{r\psi'}{\psi}\right]_{r_{w-}}^{r_{w+}} = \gamma\tau_w. \tag{4.4}$$

In both boundary conditions the inertial term $\tau_A^2\gamma_D^2$ has been neglected, as in the previous chapter, having no bearing near points of marginal stability ($\gamma = 0$) with zero rotation. Continuing with the previous chapter notation (Equation (3.29)), the current-drive and pressure-drive coefficients are

$$A = \frac{2m}{m - nq_0}, \qquad B = \frac{m^2}{(m - nq_0)^2}. \tag{4.5}$$

The perturbed flux is again expressed as a superposition of a tearing and a wall component as $\psi(r) = \alpha_t\psi_t(r) + \alpha_w\psi_w(r)$, as depicted in Figure 4.1. In this simplified 2-layer formulation are each described by a single tent-like basis function, as defined in the previous chapter Equation (3.21) and repeated here for convenience:

$$\phi_j = \begin{cases} \dfrac{(r/r_{j-1})^m - (r/r_{j-1})^{-m}}{(r_j/r_{j-1})^m - (r_j/r_{j-1})^{-m}}, & r_{j-1} < r < r_j \\ \dfrac{(r/r_{j+1})^m - (r/r_{j+1})^{-m}}{(r_j/r_{j+1})^m - (r_j/r_{j+1})^{-m}}, & r_j < r < r_{j+1} \end{cases}.$$

This is the basis function used for a mode located at r_j with boundary conditions at $r_{j-1} < r_j$ and $r_{j+1} > r_j$. Plugging this solution into the tearing and wall boundary conditions, Equations (4.2) and (4.4), produces a matrix equation and dispersion relation of the same form as in the 3-layer and

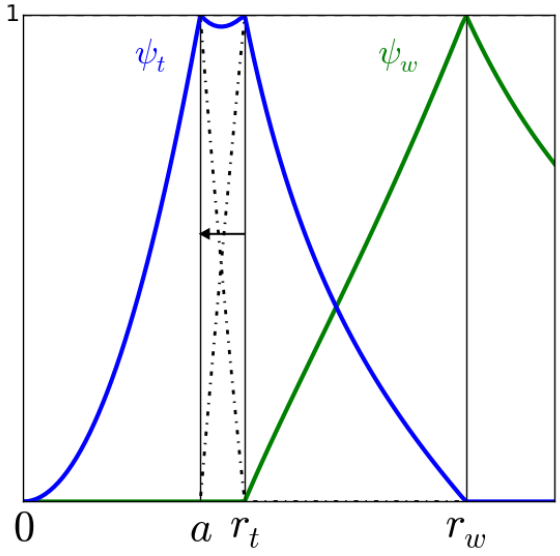

Figure 4.1: A basis of tent functions for the 2-layer model; a current/pressure/tearing layer at $r_t \to a$ and a resistive-wall at r_w.

4-layer models, repeated here for convenience:

$$\begin{bmatrix} \Delta_t - \gamma_D \tau_t & L_{wt} \\ L_{tw} & \Delta_w - \gamma \tau_w \end{bmatrix} \begin{bmatrix} \alpha_t \\ \alpha_w \end{bmatrix} = 0,$$

$$\gamma^2 + \left(-\frac{\Delta_t}{\tau_t} - \frac{\Delta_w}{\tau_w} + i\Omega \right) \gamma + \frac{1}{\tau_t \tau_w} \left(\Delta_t \Delta_w - L_{tw} L_{wt} - i\Omega \tau_t \Delta_w \right) = 0.$$

The diagonal components represent the separate tearing and wall contributions, while the off-diagonal components couple the two. We make use of the $R^{\pm}$ notation defined in Equations (3.34) and (3.35), which we remind the reader to be

$$R_k^+ \equiv (r_k/r_{k+1})^m + (r_k/r_{k+1})^{-m},$$
$$R_k^- \equiv (r_k/r_{k+1})^m - (r_k/r_{k+1})^{-m},$$

These positive geometric constants described the coupling between the radius r_k and the next neighboring radius r_{k+1}, going radially outward. In these terms, the boundary conditions in Equations

(4.2) and (4.4) produce the new dispersion relation coefficients for the 2-layer model, found to be

$$\Delta_t = \delta_{at} + (A + B\beta) = -m\left(\frac{R_t^+}{R_t^-} + 1\right) + A + B\beta, \tag{4.6}$$

$$\Delta_w = [r\psi_w']_{r_w} = -m\left(1 + \frac{2}{R_t^-}\right), \tag{4.7}$$

$$L_{tw} = [r\psi_t']_{r_w} = \frac{2m}{R_t^-}, \tag{4.8}$$

$$L_{wt} = [r\psi_w']_{r_t} = \frac{2m}{R_t^-}. \tag{4.9}$$

Analytic β Limits at Zero Rotation

Recall that the β-limits in the 4-β framework are found by solving the marginal stability condition $\gamma = 0$ at zero rotation ($\Omega = 0$). For finite values of τ_t and τ_w and $\Omega = 0$, the condition $\Delta_t\Delta_w - L_{tw}L_{wt} = 0$ results in the resistive-plasma resistive-wall limit

$$\boxed{\beta_{rp-rw} = \frac{1}{B}\left(-A - \delta_{at} + \frac{L_{tw}L_{wt}}{\Delta_w}\right)}. \tag{4.10}$$

Next, taking the ideal-wall case $\tau_w \to \infty$, with finite τ_t, reduces the dispersion condition to $\Delta_t = 0$, leading to a resistive-plasma ideal-wall limit

$$\boxed{\beta_{rp-iw} = \frac{1}{B}\left(-A - \delta_{at}\right)}. \tag{4.11}$$

On the other hand, taking an ideal-plasma $\tau_t \to \infty$ with finite τ_w, the analogous condition $\Delta_w = 0$ provides no β-limit since Δ_w is independent of β. As in the 3-layer model, we instead find that the ideal-plasma β-limit occurs where $\Delta_t \to \infty$. Unlike the 3-layer model, however, this condition in the 2-layer model leads to infinite stabilization of the ideal-plasma limits:

$$\boxed{\beta_{ip-rw} = \beta_{ip-iw} = \infty}. \tag{4.12}$$

In this cylindrical step-function profile, a perfectly conducting tearing layer adjacent to the plasma edge completely stabilizes the mode up to infinite β, similar to the close-in ideal-wall formulation in the non-resonant Shafranov model, described in Section 3.3 of the previous chapter. Furthermore

the perfect shielding of the mode completely disconnects it from the wall, and hence the effect is independent of whether the wall is resistive or ideal. As soon demonstrated in the two-harmonic toroidal extension, the shielding at a resonant surface does not affect *non-resonant* harmonics, which can drive a response at the wall even in the ideal-plasma limit.

4.2 Comparison of β-Limits in the Different Reduced-MHD Models

As discussed above, the 2-layer model positions the tearing radius r_t just outside of the current/pressure step a, keeping fixed q_0 and $q(r_t) = m/n$. In the context of the sharp-boundary model presented in the next chapter, this assumption reduces the number of domains of integration, thereby simplifying the solution and reducing computational costs.

We now analyze the error in the resistive-plasma limits, β_{rp-rw} and β_{rp-iw}, introduced in the 2-layer model by the approximation of $r_t \to a_+$. This is taken in comparison with the 3-layer model, where the tearing layer is positioned according to the q-profile at $r_t = a\sqrt{m/(nq_0)}$. Focusing on the parameter range addressed by Brennan and Finn [4], we fix $m = 2$ and $n = 1$, with the safety factor at the current/pressure step ranging around $q_0 = 0.9$. This leads in the 3-layer model to $r_t/a \sim \sqrt{2}$, compared to the 2-layer model where by definition $r_t/a = 1$. In the 3-layer model, taking $r_t \to a$ involves taking $q_0 \to m/n$, introducing a singularity that destabilizes the mode so that it becomes unstable even at $\beta = 0$. In this case $\beta_{rp-rw} \to 0$ for the 3-layer model, with a finite limit for the 2-layer model, so that the over-estimation error of the 2-layer model becomes infinitely large. In addition to avoiding the singularity, the 2-layer $r_t \to a_+$ approximation is stabilizing because placing a resistive surface beyond of the current/pressure gradient reduces some of the current/pressure drive in same fashion as a resistive wall. That is why the ideal-plasma limits in the 2-layer model are completely stabilized ($\beta_{ip-rw} = \beta_{ip-iw} = \infty$), and thus not considered in the 3-layer model comparison below.

Figure 4.2a shows that in the range discussed above the 2-layer model overestimates the $m = 2$ mode β_{rp-rw} limit, relative to the 3-layer model, by approximately $45\% - 100\%$ relative to a $42\% - 60\%$ difference in the tearing radius compared to $r_t/a = 1$. In this calculation the resistive wall is positioned at $r_w/a = 2.0$, beyond the tearing radius. For the ideal-wall case, Figure 4.2b shows a smaller error of $35\% - 75\%$ with the same $42\% - 60\%$ difference in tearing radius compared

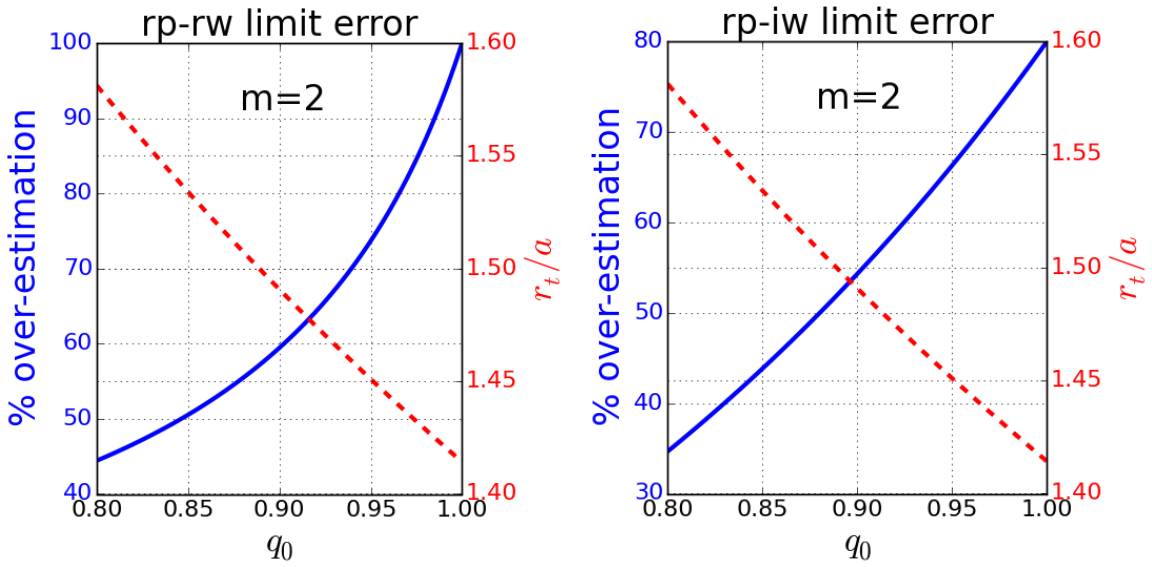

(a) (b)

Figure 4.2: Overestimation of the $m = 2$ mode resistive-plasma β-limits in the 2-layer model, where $r_t/a = 1$, compared to the 3-layer model where $r_t = a\sqrt{m/nq_0}$, for (a) β_{rp-rw} and (b) β_{rp-iw}. Here $n = 1$ and $r_w/a = 2.0$.

to $r_t/a = 1$.

Next considering an $m = 3$ mode, with a farther tearing radius (but still in the range $r_t < r_w = 2.0a$) in the same range of q_0, Figure 4.3a shows the 2-layer model to overestimates β_{rp-rw} limit by a much lower amount relative to the $m = 2$ mode; approximately $5.5\% - 6\%$ relative to a $73\% - 93\%$ difference in the tearing radius compared to $r_t/a = 1$. The ideal-wall case, plotted in Figure 4.2b, again shows a smaller error of $0.6\% - 4.3\%$ with the same $73\% - 93\%$ difference in tearing radius compared to $r_t/a = 1$.

We conclude that the error in the resistive-plasma β-limits for the dominant mode is comparable with the relative shift in the tearing radius. The error for the sub-dominant modes is smaller by an order of magnitude. While these effects carry over to the similar approximation made in the sharp-boundary model, we expect the total impact on the resistive-plasma limits to be reduced with the addition of a large spectrum of coupled poloidal harmonics. Furthermore, as we demonstrate in the two-harmonic reduced model later in this chapter, toroidal curvature introduces finite ideal-plasma limits in a 2-layer system due to the effect of geometric mode-coupling. Thus in shaped toroidal geometry the effect of the $r_t \to a_+$ approximation is expected to be less significant than in the cylindrical case.

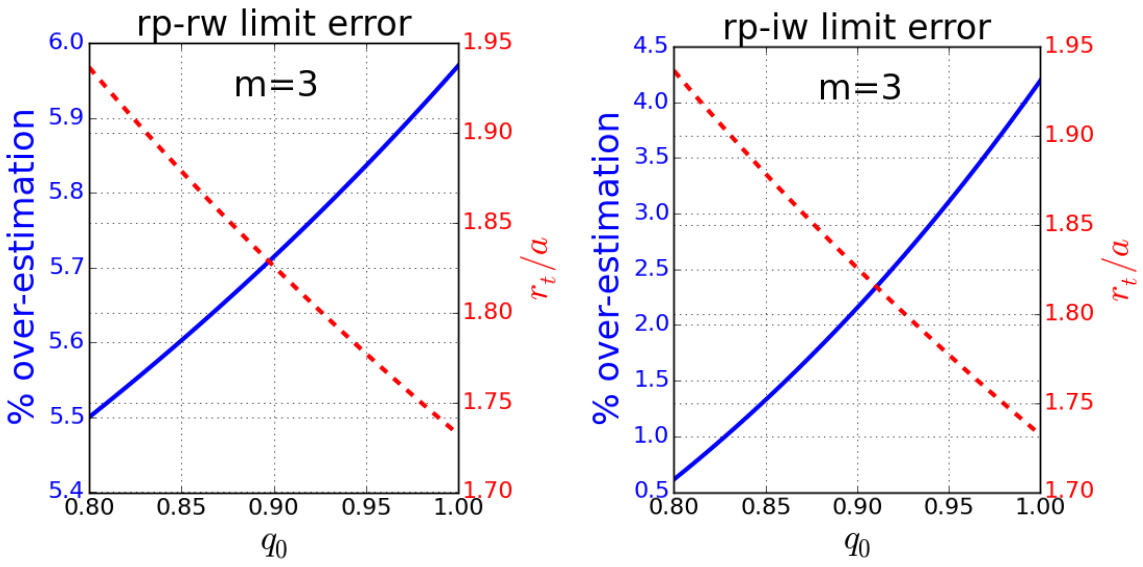

(a) (b)

Figure 4.3: Overestimation of the $m = 3$ mode resistive-plasma β-limits in the 2-layer model, where $r_t/a = 1$, compared to the 3-layer model where $r_t = a\sqrt{m/nq_0}$, for (a) β_{rp-rw} and (b) β_{rp-iw}. Here $n = 1$ and $r_w/a = 2.0$.

Summary of 4-Layer, 3-Layer and 2-Layer Cylindrical Models

We summarize differences in the β-limits obtained in the 2-layer, 3-layer and 4-layer models, compared in Table 4.1 below. For conciseness we define the repeated parameter $A_t \equiv k_{t1}k_{1t}/(A + \delta_1)$, which combines the current drive A with the coupling of the current step to the tearing layer. The β-limit comparison in Table 4.1 highlights the reason for the 4-layer profile in the model by Brennan and Finn [4], where a pressure step separates the tearing layer and the wall. In the 3-layer model, with the pressure step combined with the current step *before* the tearing layer, the ideal-plasma case where $\tau_t \to \infty$ completely disconnects the current drive and pressure drive from the wall, making the two ideal-plasma limits identical and independent of the wall properties. In the 2-layer model, the two identical ideal-plasma limits are increased up to ∞ as the perfectly shielding tearing surface approaches the current/pressure step, similar to the close-in ideal-wall effect discussed in Section 3.3. As demonstrated in the next section, toroidal geometry introduces additional degrees of freedom via harmonic coupling, which allows the wall mode to be driven unstable by a secondary harmonic even when the first is perfectly shielded by a corresponding resonant layer. This effect plays a crucial role in the sharp-boundary model presented in Chapter 5.

	4-Layer Model	3-Layer Model	2-Layer Model
$B\beta_{rp-rw}$	$-\delta_2 + \frac{k_{w2}k_{2w}(\delta_t - A_t) + k_{t2}k_{2t}\delta_w}{\delta_w(\delta_t - A_t)}$	$-\delta_a - A + \frac{k_{ta}k_{at}\delta_w}{\delta_t\delta_w - k_{tw}k_{wt}}$	$-\delta_{at} + A + \frac{k_{ta}k_{at}}{\delta_w}$
$B\beta_{rp-iw}$	$-\delta_2 + \frac{k_{t2}k_{2t}}{\delta_t - A_t}$	$-\delta_a - A + \frac{k_{ta}k_{at}}{\delta_t}$	$-\delta_{at} + A$
$B\beta_{ip-rw}$	$-\delta_2 + \frac{k_{w2}k_{2w}}{\delta_w}$	$-\delta_a - A$	∞
$B\beta_{ip-iw}$	$-\delta_2$	(same as above)	∞

Table 4.1: Analytic β-limits (multiplied by the pressure-drive parameter B) in different versions of the reduced-MHD model. The 4-layer model is the Brennan-Finn formulation [4] with a separate layer for the current step, tearing layer, pressure step and wall (in this radial order going outward). The 3-layer model is the Finn formulation [5] with a combined current/pressure step, followed by a tearing layer and a wall. The 2-layer model has a combined current/pressure/tearing layer, followed by a resistive wall.

4.3 Two-Harmonic Reduced-MHD Formulation

We now present a toroidal extension of the 2-layer reduced-MHD model described above, in order to build an intuition for geometric mode-coupling and its effect on the β-limits. The extension includes two poloidal mode harmonics that are geometrically coupled by first-order toroidal curvature, while retaining the benefit of being completely analytic.

Curvature in a Torus

In the 4-layer (Brennan-Finn) model described in Section 3.5, the surface curvature associated with the pressure drive in Equation (3.17) appears as a constant

$$\kappa_p = -\frac{B_\theta^2(r)}{B_0^2}\frac{1}{r}\bigg|_{r=a} = -\frac{a}{R_0^2 q_0^2}. \tag{4.13}$$

Fourier harmonics in a cylinder are orthogonal, so that the stability of each harmonic is analyzed independently. Coupling between neighboring harmonics is introduced by toroidal curvature, with

the normal component given by

$$\begin{aligned}\kappa_t \cdot \hat{\boldsymbol{e}}_r &= -\frac{1}{R(a,\theta)}\cos\theta = -\frac{1}{R_0}\frac{\cos\theta}{1+a/R_0\cos\theta} \\ &\approx -\frac{1}{R_0}\left(\cos\theta - a/R_0\cos^2\theta\right). \end{aligned} \tag{4.14}$$

Applying a flux surface average $< f > \equiv < f/R > / < 1/R >$, the total (poloidal plus toroidal) average curvature becomes

$$\kappa_0 = < (\boldsymbol{\kappa}_p + \boldsymbol{\kappa}_t)\cdot\hat{\boldsymbol{e}}_r > = -\frac{a}{R_0^2 q_0^2}(1-q_0^2), \tag{4.15}$$

in agreement with the Mercier criterion $q_0^2 > 1$ if $p'(r) < 0$ (a necessary stability condition explained in detail by Bateman [79]). Brennan and Finn [4] kept $q_0 < 1$ while ignoring the resonant $m = 1$ mode in order to study the destabilizing effect of a pressure gradient on an $m = 2$ mode and its corresponding β-limits. To similarly ensure that the present model incorporates the pressure jump as a *destabilizing* effect, we assume that $\kappa_0 = -|\kappa_0| < 0$, independent of the value of q_0. Thus the magnitude of the total surface curvature is written as

$$\kappa(\theta) = -|\kappa_0|(1+\kappa_1\cos\theta), \tag{4.16}$$

considering only the $m \pm 1$ coupling introduced by the $\cos\theta$ term and neglecting the $m \pm 2$ coupling from the smaller $(a/R_0)\cos^2\theta$ term. Here the positive toroidal curvature parameter is defined by

$$\kappa_1 \equiv \frac{1/R_0}{|\kappa_0|}. \tag{4.17}$$

Relative to the average curvature magnitude which scales as $|\kappa_0| \sim \epsilon^2$, the toroidal term $\kappa_1 \sim \epsilon^{-1}$ is the dominant contribution to the curvature and thus plays an important role in the pressure drive. This varying curvature term replaces $-B_\theta^2/(aB_0^2)$ in Equation (3.17), to introduce sideband coupling $(m \pm 1)$ of poloidal harmonics.

Two-Harmonic Reduced-MHD Equation

In a two-harmonic system, the perturbed magnetic flux is written as a sum of two basis functions

$$\psi = \alpha_1 \psi_1 e^{im_1\theta} + \alpha_2 \psi_2 e^{im_2\theta}, \tag{4.18}$$

corresponding to the *two different poloidal harmonics* m_1 and $m_2 = m_1 + 1$. Including the first-order toroidal curvature from Equation (4.16) above, the perturbed flux in the reduced-MHD Equation (3.17) includes the possibility of multiple harmonic components ψ_j satisfying

$$\begin{aligned} 0 &= \sum_{j=1,2} F_j(r) \left[\nabla_\perp^2 - \left(\frac{mj'(r)}{rF_j(r)} + \frac{2m_j^2|\kappa_0|(1+\kappa_1\cos\theta)p'(r)}{B_0^2 r F_j^2(r)} \right) \right] \psi_j \\ &= \sum_{j=1,2} F_j(r) \left[\nabla_\perp^2 + \frac{D_j}{a}\delta(r-a) + \frac{m_j^2}{aF_j^2}\beta\kappa_1\cos(\theta)\delta(r-a) \right] \psi_j. \end{aligned} \tag{4.19}$$

Here $|\kappa_0|$ is absorbed into β. The combined current/pressure drive on each harmonic is given by

$$D_1 = \frac{2m_1}{F_1} + \frac{m_1^2}{F_1^2}\beta, \tag{4.20}$$

$$D_2 = \frac{2m_2}{F_2} + \frac{m_2^2}{F_2^2}\beta, \tag{4.21}$$

with each $\boldsymbol{k}\cdot\boldsymbol{B}$ term given by

$$F_1 = F_1(a) = \frac{B_\theta(a)}{a}\left[m_1 - nq(a)\right] = m_1 - nq_a, \tag{4.22}$$

$$F_2 = F_2(a) = \frac{B_\theta(a)}{a}\left[m_2 - nq(a)\right] = m_2 - nq_a. \tag{4.23}$$

Each of these basis functions has both a tearing and a wall component. The reduced-MHD equation is now expanded in the two Fourier harmonics:

$$\begin{aligned} 0 =& \alpha_1\psi_1 e^{im_1\theta} F_1(r) \left[\frac{1}{r\psi_1}\frac{d}{dr}\left(r\frac{d}{dr}\psi_1 \right) - \frac{m_1^2}{r^2\psi_1} + \frac{D_1}{a}\delta(r-a) + \frac{m_1^2}{aF_1^2}\kappa_1\frac{1}{2}\left(e^{i\theta}+e^{-i\theta}\right)\delta(r-a) \right] \\ &+ \alpha_2\psi_2 e^{im_2\theta} F_2(r) \left[\frac{1}{r\psi_2}\frac{d}{dr}\left(r\frac{d}{dr}\psi_2 \right) - \frac{m_2^2}{r^2\psi_2} + \frac{D_2}{a}\delta(r-a) + \frac{m_2^2}{aF_2^2}\kappa_1\frac{1}{2}\left(e^{i\theta}+e^{-i\theta}\right)\delta(r-a) \right]. \end{aligned} \tag{4.24}$$

The cosine was replaced here with the complex exponents expression in order to conveniently derive the coupling which comes from $e^{i\theta(m\pm1)}$. The two harmonics are coupled by the toroidal curvature variation $\kappa_1\cos(\theta)$, and return to two uncoupled equations when $\kappa_1 = 0$. Fourier inversion for each harmonic produces two coupled equations

$$m_1: \quad 0 = \alpha_1\psi_1 F_1(r)\left[\frac{1}{r\psi_1}\frac{d}{dr}\left(r\frac{d}{dr}\psi_1\right) - \frac{m_1^2}{r^2\psi_1} + \frac{D_1}{a}\delta(r-a)\right] + \alpha_2\psi_2\frac{1}{2}\frac{m_1^2}{aF_2}\kappa_1\delta(r-a), \quad (4.25)$$

$$m_2: \quad 0 = \alpha_2\psi_2 F_2(r)\left[\frac{r}{r\psi_2}\frac{d}{dr}\left(r\frac{d}{dr}\psi_2\right) - \frac{m_2^2}{r^2\psi_2} + \frac{D_2}{a}\delta(r-a)\right] + \alpha_1\psi_1\frac{1}{2}\frac{m_2^2}{aF_1}\kappa_1\delta(r-a). \quad (4.26)$$

Dividing line one by F_1 and line two by F_2, and radially integrating across the combined current/-pressure jump yields

$$m_1: \quad 0 = \alpha_1\psi_1(a)\left(\left[\frac{r\psi_1'}{\psi_1}\right]_{a_-}^{a_+} + D_1\right) + \alpha_2\psi_2(a)B_{12}\kappa_1, \quad (4.27)$$

$$m_2: \quad 0 = +\alpha_1\psi_1(a)B_{21}\kappa_1 + \alpha_2\psi_2(a)\left(\left[\frac{r\psi_2'}{\psi_2}\right]_{a_-}^{a_+} + D_2\right), \quad (4.28)$$

with the off-diagonal pressure drive components defined by

$$B_{12} \equiv \frac{1}{2}\frac{m_2^2}{F_1F_2}\beta, \qquad B_{21} \equiv \frac{1}{2}\frac{m_1^2}{F_1F_2}\beta. \quad (4.29)$$

In the simplified profile where $r_{t-} \to a_+$, the current/pressure jump can be written in terms of the tearing layer condition and the total flux across the combined current/pressure/tearing layer:

$$\begin{aligned}[\psi']_{a_-}^{a_+} &= \psi'(r_{t-}) - \psi'(a_-) \\ &= [\psi'(r_{t-}) - \psi'(r_{t+})] + [\psi'(r_{t+}) - \psi'(a_-)] \\ &= -\frac{\psi(a)}{a}\gamma_D\tau_t + [\psi']_{a_-}^{r_{t+}}.\end{aligned}$$

This combined boundary condition matches Fitzpatrick's formulation [69] used in the sharp-boundary model. The total flux jump across the combined current/pressure/tearing layer of each harmonic depends on the outer vacuum solution and boundary conditions.

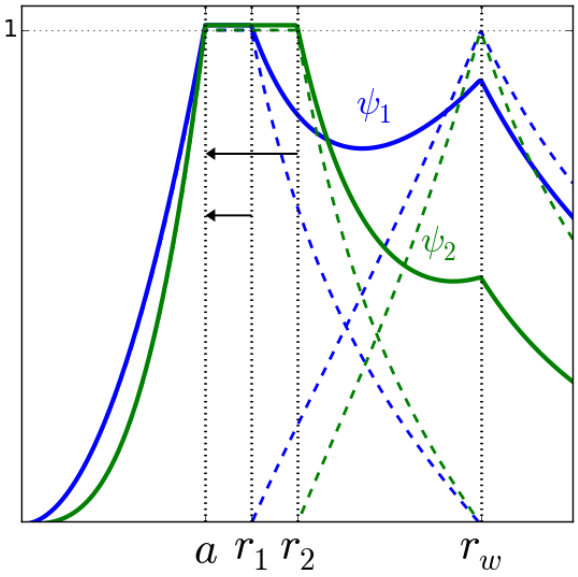

Figure 4.4: Flux functions of the two-harmonic model depicted in a basis of tent functions.

Two-Harmonic Vacuum Solution in a Basis of Tent Functions

As in the single mode case, the vacuum flux solutions are a linear combination of r^m and r^{-m} for each harmonic. These are conveniently expressed in a basis of tent functions with a separate wall mode and tearing mode for each harmonic, as depicted in Figure 4.4. In this basis each harmonic component ψ_j is broken down into a combined plasma-tearing mode function $\phi_{j,a}$ and a wall mode function $\phi_{j,w}$:

$$\psi_1 = \phi_{1,a}(r) + \psi_{1,w}\phi_{1,w}(r), \tag{4.30}$$

$$\psi_2 = \phi_{2,a}(r) + \psi_{2,w}\phi_{2,w}(r). \tag{4.31}$$

Note that the flux amplitude of each mode is normalized to unity at the combined current/pressure/tearing layer, while at the wall $\psi_{j,w}$ is free to be determined by the corresponding wall boundary condition. Each of the tent-like basis functions $\phi_{j,a}$ and $\phi_{j,w}$ is expressed according to the tent function defined in Equation (3.21), now with respect to its corresponding harmonic m_j and its radius r_k:

$$\phi_{j,k} \equiv \begin{cases} \dfrac{(r/r_{k-1})^{m_j} - (r/r_{k-1})^{-m_j}}{(r_k/r_{k-1})^{m_j} - (r_k/r_{k-1})^{-m_j}}, & r_{k-1} < r < r_k \\ \dfrac{(r/r_{k+1})^{m_j} - (r/r_{k+1})^{-m_j}}{(r_k/r_{k+1})^{m_j} - (r_k/r_{k+1})^{-m_j}}, & r_k < r < r_{k+1} \end{cases}. \tag{4.32}$$

Similarly the positive geometric coefficients $R^{\pm}$ defined in Equations (3.34) and (3.35) are similarly generalized to an arbitrary harmonic m_j and radius r_k:

$$R^{\pm}_{j,k} \equiv (r_k/r_{k+1})^{m_j} \pm (r_k/r_{k+1})^{-m_j}, . \tag{4.33}$$

This allows for a concise formulation of the self inductance coefficients

$$\delta_{j,a} \equiv \left[r\phi'_{j,a}\right]_{a-}^{r_{j+}} = -m_j \left(\frac{R^+_{j,a}}{R^-_{j,a}} + 1\right), \tag{4.34}$$

$$\delta_{j,w} \equiv \left[r\phi'_{j,w}\right]_{r_{w-}}^{r_{w+}} = -m_j \left(1 + \frac{R^+_{j,a}}{R^-_{j,a}}\right), \tag{4.35}$$

which turn out to be equal for $r = a$ and $r = r_w$, and the mutual inductance coefficients which also agree:

$$k_{j,aw} \equiv -r\phi'_{j,a}(r_{w-}) = \frac{2m_j}{R^-_{j,a}} = r\phi'_{j,w}(r_{a+}) \equiv k_{j,wa}. \tag{4.36}$$

Boundary Conditions and Dispersion Relation

The outer solution for the total flux jump across the combined plasma-tearing surface, in terms of the geometric coefficients above, is given by

$$\left[\frac{r\psi'_1}{\psi_1}\right]_{a-}^{r_{1+}} = \delta_{1,a} + \psi_{1,w}k_{1,wa}, \tag{4.37}$$

$$\left[\frac{r\psi'_2}{\psi_2}\right]_{a-}^{r_{2+}} = \delta_{2,a} + \psi_{2,w}k_{2,wa}. \tag{4.38}$$

The amplitudes at the wall are determined by the resistive wall boundary conditions

$$\gamma\tau_w = \left[\frac{r\psi'_1}{\psi_1}\right]_{r_{w-}}^{r_{w+}} = \frac{k_{1,aw}}{\psi_{1,w}} + \delta_{1,w}, \tag{4.39}$$

$$\gamma\tau_w = \left[\frac{r\psi'_2}{\psi_2}\right]_{r_{w-}}^{r_{w+}} = \frac{k_{2,aw}}{\psi_{2,w}} + \delta_{2,w}, \tag{4.40}$$

which yield

$$\psi_{1,w} = \frac{k_{1,aw}}{\gamma\tau_w - \delta_{1,w}}, \qquad \psi_{2,w} = \frac{k_{2,aw}}{\gamma\tau_w - \delta_{2,w}}. \tag{4.41}$$

Plugging these wall amplitudes back into the outer solution in Equations (4.37) and (4.38) produces

$$\left[\frac{r\psi_1'}{\psi_1}\right]_{a-}^{r_{1+}} = \delta_{1,a} + \frac{k_{1,aw}k_{1,wa}}{\gamma\tau_w - \delta_{1,w}}, \tag{4.42}$$

$$\left[\frac{r\psi_2'}{\psi_2}\right]_{a-}^{r_{2+}} = \delta_{2,a} + \frac{k_{2,aw}k_{2,wa}}{\gamma\tau_w - \delta_{2,w}}, \tag{4.43}$$

which completes the eigenvalue system. Denoting the wall-coupling terms by

$$l_1 \equiv k_{1,aw}k_{1,wa}, \qquad l_2 \equiv k_{2,aw}k_{2,wa}, \tag{4.44}$$

and the combined current/pressure drive and geometric terms by

$$\Delta_1 = D_1 + \delta_{1,a}, \qquad \Delta_2 = D_2 + \delta_{2,a}, \tag{4.45}$$

the coupled two-harmonic resistive-wall system is found to be

$$\begin{bmatrix} \gamma\tau_1 - \left(\Delta_1 + \frac{l_1}{\gamma\tau_w - \delta_{1,w}}\right) & -\kappa_1 B_{12} \\ -\kappa_1 B_{21} & \gamma\tau_2 - \left(\Delta_2 + \frac{l_2}{\gamma\tau_w - \delta_{2,w}}\right) \end{bmatrix} \begin{bmatrix} \alpha_1 \\ \alpha_2 \end{bmatrix} = 0. \tag{4.46}$$

The geometric parameters $l_1, l_2, \delta_{1,w}, \delta_{2,w}$ quantify the coupling of the tearing layers to the wall, the diagonal terms Δ_1 and Δ_2 drive the uncoupled ideal-plasma modes, and the off-diagonal components B_{12} and B_{21} represent the pressure-drive created by mode-coupling. The toroidal coupling terms, although each dependent upon the sign of F_1 and F_2, will only appear in the dispersion relation as the product $B_{12}B_{21}$ and are thus always *destabilizing*.

Observe that the form above is conducive to analysis of the ideal wall limit $\tau_w \to \infty$. Alternately multiplying out the $\gamma\tau_w$ terms from the denominator reveals a complicated eigenvalue structure (in comparison with the single-mode problem presented in Equation (3.62)) with off-diagonal γ components,

$$\begin{bmatrix} (\gamma\tau_1 - \Delta_1)(\gamma\tau_w - \delta_{1,w}) - l_1 & -\kappa_1 B_{12}(\gamma\tau_w - \delta_{1,w}) \\ -\kappa_1 B_{21}(\gamma\tau_w - \delta_{2,w}) & (\gamma\tau_2 - \Delta_2)(\gamma\tau_w - \delta_{2,w}) - l_2 \end{bmatrix} \begin{bmatrix} \alpha_1 \\ \alpha_2 \end{bmatrix} = 0, \tag{4.47}$$

which leads to yields a fourth order polynomial. Dividing through by the $\gamma\tau_1$ and $\gamma\tau_2$ terms produces

a third form

$$\begin{bmatrix} (\gamma\tau_w - \delta_{1,w}) - \frac{l_1}{\gamma\tau_1 - \Delta_1} & -\kappa_1 B_{12} \frac{\gamma\tau_w - \delta_{1,w}}{\gamma\tau_1 - \Delta_1} \\ -\kappa_1 B_{21} \frac{\gamma\tau_w - \delta_{2,w}}{\gamma\tau_2 - \Delta_2} & (\gamma\tau_w - \delta_{2,w}) - \frac{l_2}{\gamma\tau_2 - \Delta_2} \end{bmatrix} \begin{bmatrix} \alpha_1 \\ \alpha_2 \end{bmatrix} = 0, \tag{4.48}$$

which is conducive to studying the respective ideal plasma limits $\tau_1 \to \infty$ and $\tau_2 \to \infty$. These different forms of the dispersion relation are useful for analytically calculating the different β-limits.

4.4 Analysis of the Two-Harmonic β-Limits with Zero Rotation

The coupled system has six β-limits

$$\beta_{r1-r2-rw}, \quad \beta_{i1-r2-rw}, \quad \beta_{r1-i2-rw}, \quad \beta_{r1-r2-iw}, \quad \beta_{i1-r2-iw}, \quad \beta_{r1-i2-iw},$$

not necessarily in order. This list excludes the limit β_{i1-i2} which is completely stable (i.e. $\beta_{crit} \to \infty$) independently of the wall, since the ideal surfaces at the plasma edge completely disconnect the plasma from the wall, similar to the Section 3.3 example of an ideal-wall adjacent to the plasma surface. Only this list of finite β-limits is considered below.

Ideal-Wall Limits

The β-limits are once again obtained by solving for the $\gamma = 0$ case in the dispersion relation shown above (in any of its forms described in Equations (4.46)-(4.48)), with $\Omega = 0$. We begin this time with the ideal-wall case $\tau_w \to \infty$. Taking two different ideal-plasma limits $\tau_j \to \infty$, one for each harmonic $j = 1$ or $j = 2$, the marginal stability conditions are found to correspond to the respective solutions

$$\Delta_2 = 0 \qquad \text{or} \qquad \Delta_1 = 0. \tag{4.49}$$

The ideal-plasma limit $\tau_1 \to \infty$ is taken keeping the other tearing time τ_2 finite, and vice versa. Note that the two harmonic solution are uncoupled in these ideal-plasma ideal-wall limits. These

conditions result in the two ideal-wall β-limits:

$$\boxed{\beta_{i1-r2-iw} = \frac{1}{B_2}\left(-A_2 - \delta_{2,a}\right) \equiv \beta_1}, \tag{4.50}$$

and

$$\boxed{\beta_{r1-i2-iw} = \frac{1}{B_1}\left(-A_1 - \delta_{1,a}\right) \equiv \beta_2}. \tag{4.51}$$

Here the total drive coefficients D_j from Equations (4.20) and (4.21) are broken down into the β-independent (positive) pressure-drive coefficients are

$$B_1 = \frac{m_1^2}{F_1^2}, \qquad B_2 = \frac{m_2^2}{F_2^2}, \tag{4.52}$$

and the current drive coefficients are

$$A_1 = \frac{2m_1}{F_1}, \qquad A_2 = \frac{2m_2}{F_2}. \tag{4.53}$$

The geometric factor, $-\delta_{j,a}$, is always positive and therefore stabilizing. The sign of of the current-drive term $-A_j$ goes like $-(m_j - nq_0)$, so that it is stabilizing for $q_0 > m_j/n$ (when the tearing surface effectively lies inside the plasma) and destabilizing otherwise, in agreement with single-mode external kink theory.

The resistive-plasma ideal-wall limits can be expressed in terms of the two ideal-plasma ideal-wall limits by

$$0 = \left[1 - \left(\frac{\kappa_1}{2}\right)^2\right]\beta^2 - (\beta_1 + \beta_2)\beta + \beta_1\beta_2. \tag{4.54}$$

While typical values of $\kappa_1 \approx 2$ will simplify the analysis of the equation above, no special behavior is associated with this point. In the absence of toroidal curvature, $\kappa_1 = 0$, the equation above can be rewritten as

$$0 = (\beta - \beta_1)(\beta - \beta_2), \tag{4.55}$$

showing that the uncoupled resistive-plasma ideal-wall limit $\beta_{r1-r2-iw}$ is identical to the ideal limits, or rather the smaller of the two. This is because the ideal-m_1 mode is limited by the resistive-m_2 component and vice versa. Around more typical values of the toroidal curvature parameter, $\kappa_1 \approx 2$,

the coupled mode is given by

$$\boxed{\beta_{r1-r2-iw} = \frac{\beta_1\beta_2}{\beta_1+\beta_2} < \beta_1, \beta_2}. \tag{4.56}$$

Hence mode-coupling from toroidal curvature destabilizes the resistive plasma mode. This ordering holds also for $\kappa_1 \neq 2$, with $\beta_{r1-r2-iw}$ given by the smaller of the two quadratic roots of Equation (4.54).

Resistive-Wall Limits

Using the two ideal-plasma ideal-wall limits from Equations (4.50) and (4.51), the two ideal-plasma resistive-wall limits can be expressed as

$$\boxed{\beta_{i1-r2-rw} = \beta_1 - L_{2w} \equiv \tilde{\beta}_1}, \tag{4.57}$$

and

$$\boxed{\beta_{r1-i2-rw} = \beta_2 - L_{1w} \equiv \tilde{\beta}_2}. \tag{4.58}$$

Here the (positive) wall coupling coefficients are given by

$$L_{1,w} = -\frac{l_1}{\delta_{1b}B_1}, \qquad L_{2,w} = -\frac{l_2}{\delta_{2b}B_2}. \tag{4.59}$$

Since $L_{j,w} > 0$, the resistive-wall modes are less stable than their ideal-wall counterparts. Similar to the ideal-wall case, the resistive-plasma resistive-wall mode can be expressed in terms of the two ideal-plasma resistive-wall limits:

$$0 = \left[1 - \left(\frac{\kappa_1}{2}\right)^2\right]\beta^2 - (\tilde{\beta}_1 + \tilde{\beta}_2)\beta + \tilde{\beta}_1\tilde{\beta}_2. \tag{4.60}$$

As in the ideal-wall case, setting $\kappa_1 = 0$ makes the uncoupled resistive-plasma limit identical to the smaller of the two ideal-plasma limits. Again considering $\kappa_1 \approx 2$ (which simplifies the analysis but does not mark any special behavior) yields the destabilized coupled resistive-plasma mode

$$\boxed{\beta_{r1-r2-rw} = \frac{\tilde{\beta}_1\tilde{\beta}_2}{\tilde{\beta}_1+\tilde{\beta}_2} < \tilde{\beta}_1, \tilde{\beta}_2}. \tag{4.61}$$

The β-ordering relations in Equations (4.56) and (4.61) are general for any q_0, r_w, m_1 and m_2. As with all stability limits, they are also independent of the timescales τ_w, τ_1 and τ_2. In parallel with the single-mode case, no clear ordering appears in the relation of the resistive-plasma ideal-wall limit $\beta_{r1-r2-iw}$ and the two ideal-plasma resistive-wall limits $\beta_{i1-r2-rw}$ and $\beta_{r1-i2-rw}$.

Having analytically demonstrated the destabilizing effect of harmonic coupling in a toroidal resistive-plasma resistive-wall system, we now discuss some examples that demonstrate the similarity between this two-harmonic 2-layer model and the single-harmonic 4-layer model of Brennan and Finn [4] discussed in the previous chapter.

4.5 4-β Limit Ordering Transitions due to Toroidal Curvature

In the interest of comparison with the four β-limits of Brennan and Finn [4], we set the r_2 surface to be extremely resistive, fixing $\tau_2 \ll \tau_1$, representing a cold edge layer that serves only to introduce harmonic coupling. The four beta limits are then obtained by varying τ_1 and τ_w, so that

$$\beta_{rp-rw} \equiv \beta_{r1-r2-rw}, \quad \beta_{rp-iw} \equiv \beta_{r1-r2-iw}, \quad \beta_{ip-rw} \equiv \beta_{i1-r2-rw}, \quad \beta_{ip-iw} \equiv \beta_{i1-r2-iw}. \quad (4.62)$$

Figure 4.5a plots the four growth rate curves versus β, for fixed $q_a = q_0 = 3.5$ and $\kappa_1 = 2.5$, demonstrating behavior similar to the four β-limits found in the Brennan-Finn 4-layer model. The equilibrium radii are set to $a = 0.8$ and $r_w = 1.0$, according to the values in Reference [4]. The wall-time is $\tau_w = 10^3$ and the two tearing times are $\tau_1 = 10^4$ and $\tau_2 = 1$, recalling that τ_2 represents a cold edge layer included for the sake of mode-coupling. The two poloidal harmonics are $m_1 = 2$ and $m_2 = 3$, and the toroidal harmonic is $n = 1$. As observed on a log scale, the four branches have distinct points of marginal stability but all converge to the ip-iw curve at large γ. While neglecting inertia causes the growth rate curve to asymptote to infinity at the ip-iw limit, the β-limits remain unaffected. Note that the constant-ψ approximation [50, 51] only applies at low γ near marginal stability, but is irrelevant at large γ where no reconnection takes place. Figure 4.5b shows that a similar set of limits is obtained by varying q_a, with $\beta = 0.4$ fixed just below the rp-rw limit observed in Figure 4.5a. The analogy between the β and q_a limits stems from the similar destabilizing effect of the pressure and current gradients. With the introduction of shaping in the sharp-boundary model,

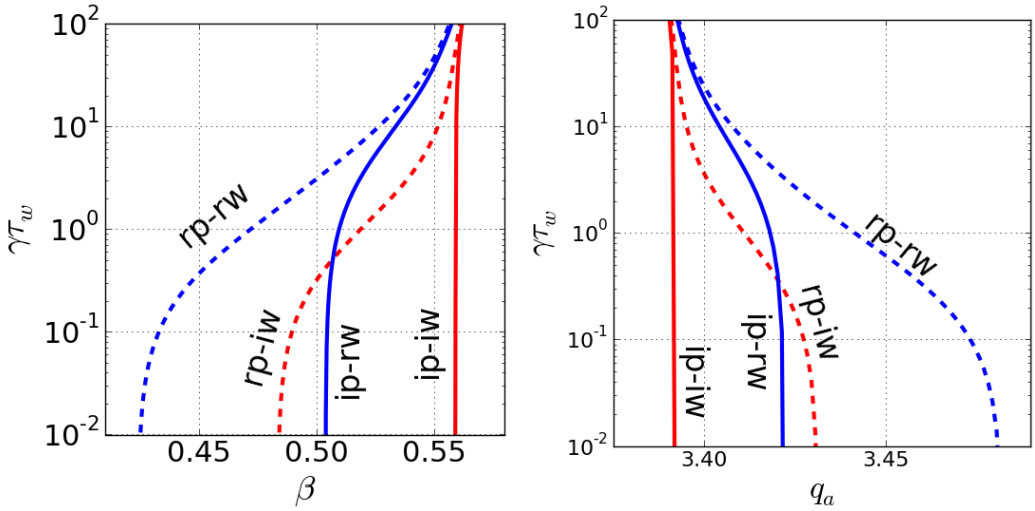

Figure 4.5: Growth rate curves of the four beta regimes with toroidal coupling parameter $\kappa_1 = 2.5$, (a) fixed $q_a = 3.5$ and varied β, and analogously (b) fixed $\beta = 0.4$ and varied q_a.

the β-q_a stability space will become more complicated.

Figure 4.6 shows how the critical β values (where $\gamma = 0$) of the four regimes change with the toroidal coupling parameter κ_1, with fixed $q_a = 3.5$. In the cylindrical limit $\kappa_1 \to 0$, where the two harmonics are uncoupled, there are only two ideal-plasma modes ip-rw and ip-iw. As κ_1 increases, the two resistive limits are driven unstable due to mode-coupling. Recall that the stabilizing effect of average toroidal curvature is neglected in this model, so that the two ideal-plasma modes are observed to be independent of the toroidal curvature variation.

This chapter has demonstrated how a 2-layer model can be extended with first-order toroidal curvature effects that couple neighboring poloidal harmonics. The resulting geometric mode coupling is analytically shown to lower the resistive-plasma β-limits and to introduce finite ideal-plasma β-limits, reproducing the four distinct β-limits that appear in the 4-layer Brennan-Finn model discussed in the previous chapter. Having developed an intuition for the effects of geometric mode coupling using an analytic construction, we next turn to the sharp-boundary model which explores the 4-β limits in shaped toroidal geometry.

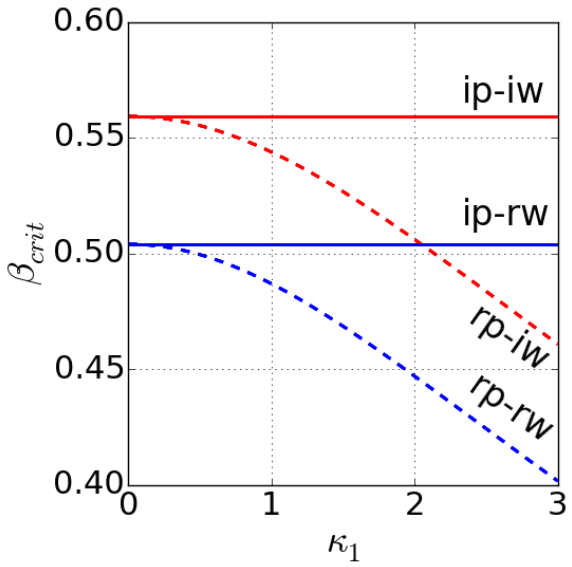

Figure 4.6: Critical-β versus toroidal coupling parameter κ_1 for the four branches, with fixed $q_a = 3.5$. As κ_1 increases from zero, each of the two ideal-plasma modes (ip-rw and ip-iw) splits into an ideal-plasma and a resistive-plasma mode.

Chapter 5

Shaped Sharp-Boundary Model with Plasma and Wall Resistivity

A sharp-boundary tokamak equilibrium consists of a skin-current, representing the plasma boundary, which results in a discontinuity in the tangential magnetic field. The jump in magnetic pressure across the plasma boundary is balanced by a jump in the fluid pressure, which follows a step function profile. The sharp-boundary model makes it convenient to scan individual equilibrium parameters - defined at the plasma boundary - without having to adjust the entire plasma profile. The present formulation builds on a resistive-MHD sharp-boundary model developed by Fitzpatrick [69] to study the effect of plasma shaping on error-field response. This formulation does not apply the reduced-MHD expansion utilized in previous chapters. We extend the geometry in Reference [69] with $O(\epsilon)$ toroidal curvature based on an ideal-MHD model by Freidberg and Grossmann [2], and also generalized with up-down asymmetry to emulate a single-null diverted plasma. Lastly, the addition of a resistive wall facilitates the study of coupled tearing-wall effects in shaped toroidal geometry.

The perturbed field response is solved by numerically integrating the vacuum-like magnetic potential, subject to boundary conditions at three surfaces:

1. The plasma boundary obeys the standard ideal MHD conditions of sharp-boundary theory [2, 54, 69, 80–84], enforcing ideal Ohm's law on either side of the perturbed boundary. A derivation is found in the textbook by Freidberg [49].

2. The tearing layers, following Fitzpatrick [69], are set just outside of the sharp plasma boundary

where the presence of a poloidal field produces a finite safety factor q. The external region can be thought of as a cold plasma with no equilibrium current and a vacuum-like q-profile, as portrayed by Finn [5]. Compacting the resonant layers near the plasma boundary imitates a diverted plasma where $q \to \infty$ at an x-point. This simplification reduces the number of outer regions of integration without qualitatively modifying the tearing layer physics. While the model is constructed to accept any tearing layer regime, present calculations apply a constant-ψ visco-resistive [50, 51] layer condition similar to a thin resistive wall with a perturbed current driven only by a resonant perturbation.

3. A resistive thin-wall boundary condition, conformal to a flux surface, is constructed similarly to the tearing boundary condition but incorporating all poloidal harmonics rather than just a resonant component.

Using the solution of the linear perturbed field problem, the perturbed energy problem is formulated as a multi-mode dispersion relation. Present calculations use 45 poloidal harmonics ($-22 < m < 22$), comparable with the number used in References [69] and [2], and a single toroidal harmonic $n = 1$. The growth rate and mode structure of the dominant mode are found by numerically solving the resulting non-linear eigenvalue problem (i.e. contains different powers of γ multiplying the system matrices, as discussed later on). A similar method was implemented by Betti [37] for a step-function profile in a circular cross-section torus. The dominant eigenvalue is found to be real for a stationary plasma, whereas an imaginary (rotating) component is introduced in the presence of bulk plasma rotation, which tends to have a stabilizing effect on the least stable mode. As discussed in Chapter 2, bulk plasma rotation can be imitated by a feedback control system with imaginary normal-field gains, making the study of rotational effects relevant despite the low rotation frequencies predicted for future devices such as ITER. By including only the necessary ingredients for studying rotational effects on tearing and resistive wall physics in shaped toroidal geometry, the sharp-boundary model facilitates broad qualitative scans, intended to gain physical insight and to guide the investigation of larger quantitative codes.

The sharp-boundary model is now described, starting with the equilibrium geometry (Section 5.1) and equilibrium pressure balance (Section 5.2). The perturbed field response is then detailed in Section 5.3, including the non-ideal effects of the resistive wall and the tearing layer. Finally, Section 5.4 describes how the dispersion relation is constructed and solved for the least stable growth rate

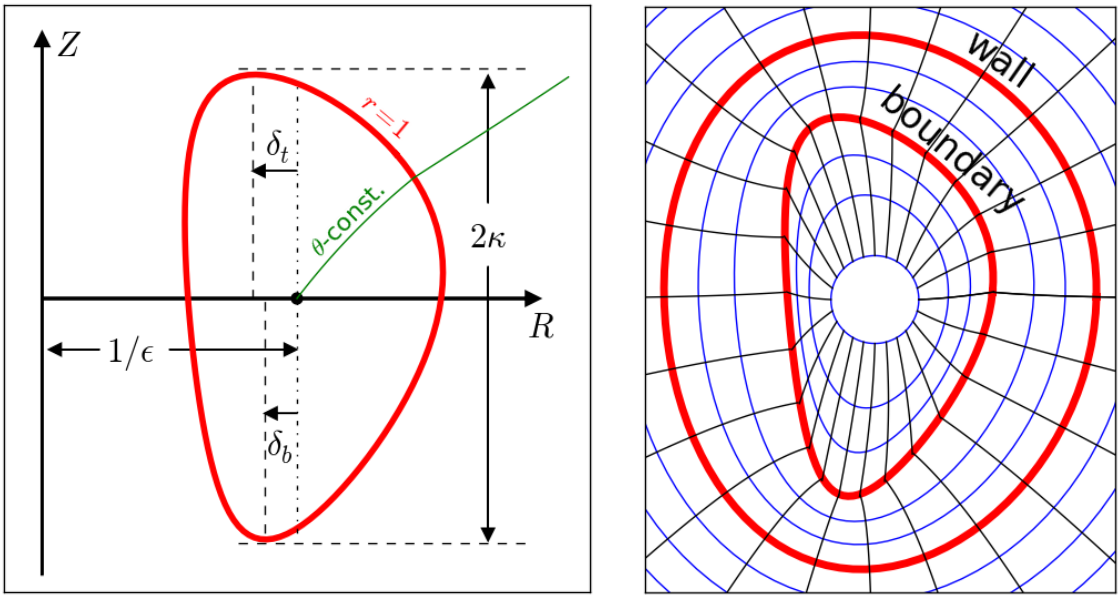

(a) (b)

Figure 5.1: (a) Plasma cross-sectional coordinates, normalized by the minor radius in the case of a circular cross-section, with the boundary defined by $r = 1$. The curved surface of constant angle-like coordinate θ is shown in green. The shape is characterized by elongation $\kappa = 1.8$, top triangularity $\delta_t = 0.35$ and bottom triangularity $\delta_b = 0.26$, parametrized by Equation (5.3) values $\kappa = 1.8$, $\delta_x = 0.14$ and $\delta_y = -0.07$. (b) Flux surfaces of constant r (blue), surfaces of constant θ (black), a resistive plasma boundary defined by $r = 1$ (red) and a resistive wall (red). The coordinates (r, θ) are the Grad-Shafranov solution described in the text. The coordinates begin at a finite innermost surface $r_0 = 0.3$ to avoid numerical issues near $r = 0$.

and its corresponding mode structure.

5.1 Equilibrium Geometry

Boundary Parametrization

The model uses a set of right-handed cylindrical polar coordinates (R, ϕ, Z), with length scales normalized by a, the minor radius in the case of a circular cross-section. To describe a shaped cross-section, R and Z are related to the curvilinear coordinates r and θ, representing a radial coordinate relative to the magnetic axis $r = 0$ and a poloidal angle-like coordinate θ in the cross-sectional plane.

The plasma boundary $r = 1$ is parametrized by

$$R_a(\theta) = 1/\epsilon + \cos(\theta) + \delta_x \cos(2\theta) - \delta_y \sin(2\theta), \tag{5.1}$$

$$Z_a(\theta) = \kappa \sin(\theta) - \delta_x \sin(2\theta) - \delta_y \cos(2\theta), \tag{5.2}$$

independent of the toroidal angle of symmetry ϕ. Throughout the thesis, subscript 'a' denotes a function evaluated at the plasma boundary $r = 1$. This generalizes the geometry from Reference [69] to include up-down asymmetry, allowing for single-null diverted plasmas. Figure 5.1a depicts these coordinates for a typical shaped cross-section. As detailed below, the radial extension $(R(r,\theta), Z(r,\theta))$ is obtained from a high aspect-ratio expansion of the Grad-Shafranov equation, following Connor and Hastie [85]. The interior plasma (r,θ) coordinates are constructed by assuming that the plasma current profile is a δ-function at the boundary $r = 1$, combined with a small flat current profile in the interior $r < 1$. The bulk of the plasma current is carried by the δ-function, while the flat current profile ensures that a non-trivial solution of the Grad-Shafranov equation exists throughout the plasma volume.

The resulting coordinates are depicted in Figure 5.1b. In the external region, $r > 1$, the coordinates are chosen to be orthogonal, becoming more circular the further away from the plasma. In the internal region, $r < 1$, the coordinates are non-orthogonal and become more circular approaching the magnetic axis. The separation into external orthogonal coordinates and internal non-orthogonal coordinates allows the perturbed field in each region to be evaluated by Laplace's equation everywhere up to the boundary, despite the triangular and up-down asymmetric geometry. The internal coordinates terminate at a finite innermost surface $r = r_0 > 0$ in order to avoid numerical issues near the magnetic axis $r = 0$. With the sharp-boundary calculations dominated by the boundary conditions at $r = 1$ and $r = r_w$, the results are found to have little dependence on the value of r_0. Throughout this thesis we set $r_0 = 0.3$. The metric coefficients and basis vectors are continuous at $r = r_0$ and $r = 1$.

The coordinates (r,θ) are designed for convenient description of the cross-sectional shape and are not straight field-line coordinates. A straight field-line angle ν is constructed for the solution to the Grad-Shafranov equation, as well as in the description of the resonant tearing layer. The coordinate basis is defined by the normalized contravariant derivatives, $\hat{\boldsymbol{e}}_r \equiv \boldsymbol{\nabla} r/|\boldsymbol{\nabla} r|$, $\hat{\boldsymbol{e}}_\theta \equiv \boldsymbol{\nabla}\theta/|\boldsymbol{\nabla}\theta|$, $\hat{\boldsymbol{e}}_\phi \equiv \boldsymbol{\nabla}\phi/|\boldsymbol{\nabla}\phi|$. The resistive wall is designed for convenience to be conformal to a flux surface $r = r_w$,

similar to the ideal-wall formulation of Goedbloed [83].

The elongation parameter κ follows the standard definition, being the height to width ratio of the plasma cross-section. The other cross-sectional shaping parameters δ_x and δ_y, which roughly represent triangularity and vertical asymmetry, are related to the top triangularity δ_t and bottom triangularity δ_b by

$$\delta_t = \frac{\kappa+2}{\kappa+4\delta_y}\delta_x, \qquad \delta_b = \frac{\kappa+2}{\kappa-4\delta_y}\delta_x. \tag{5.3}$$

These relations are obtained by expanding about $\theta = 0$, $\theta = \pi/2$ and $\theta = -\pi/2$, respectively, and neglecting factors of order $(\delta_t/\kappa)^2 \sim (\delta_b/\kappa)^2 \ll 1$. Triangularity is defined by $\delta = R_0 - R(Z_a^{\max})$ for up-down symmetric cross-sections [86], where in the present normalization $R_0 = 1/\epsilon$. Up-down asymmetry is gauged by comparing the top triangularity $\delta_t = R_0 - R(Z_a^{\max})$ with the bottom triangularity $\delta_b = R_0 - R(Z_a^{\min})$, both depicted in Figure 5.1a.

To approximate reasonable equilibrium bounds of the shaping parameters, the cross-section is required to maintain positive curvature. For the up-down symmetric case where $\delta_y = 0$, this requirement is expressed as $\frac{\partial R_a}{\partial \theta}\big|_{\theta\to\pi-} < 0$. The resulting bound for triangularity is found to be $\delta < 0.54$ (or $\delta_x < 1/4$), compatible with the typical range of ITER baseline scenarios [87] with elongation $1.7 < \kappa < 2.0$, triangularity $0.3 < \delta < 0.5$ and up-down symmetry.

Grad Shafranov Shaping Equations

A Fourier series defines the parametrization of the magnetic surface, including both up-down symmetric ($S_n(r)$) and up-down asymmetric ($C_n(r)$) shape functions. These shape functions will be determined by a large aspect-ratio expansion of the Grad-Shafranov equation. In present calculations, the Fourier series will include only S_2, S_3 and C_3, corresponding to elongation, horizontal triangularity and up-down asymmetric triangularity.

Let (R, ϕ, Z) be the standard right-handed cylindrical polar coordinates. The generalized cross-sectional coordinates (r, θ), mutually perpendicular to the axisymmetric coordinate ϕ, are defined by

$$R = 1/\epsilon + r\cos\theta - \sum_n S_n(r)\cos(n-1)\theta + \sum_n C_n(r)\sin(n-1)\theta, \tag{5.4}$$

$$Z = r\sin\theta + \sum_n S_n(r)\sin(n-1)\theta + \sum_n C_n(r)\cos(n-1)\theta. \tag{5.5}$$

Here $\theta = 0$ is defined at the outboard side of the torus and $r = 1$ at the plasma boundary. This parametrization extends the formulation of Connor and Hastie [85] to include up-down asymmetry, expressed by the C_n-series in the equation above. The signs preceding the shaping parameters are chosen to guarantee orthogonality of the external contravariant basis vectors, as in Equation (5.39). This general form must be made to satisfy the Grad-Shafranov equation for MHD pressure balance in a torus, which is written in the notation of Fitzpatrick, Gimblett and Hastie [88] (equation 2.4) as

$$\frac{f}{r}\frac{\partial}{\partial r}\left(rf|\boldsymbol{\nabla} r|^2\right) + \frac{f}{r}\frac{\partial}{\partial \nu}\left(rf\boldsymbol{\nabla} r\cdot\boldsymbol{\nabla}\nu\right) + \frac{R^2 p'}{B_0^2} + gg' = 0, \tag{5.6}$$

in terms the straight field-line angle ν, the distance from the symmetry axis R, the pressure p, and the normalized toroidal and poloidal field distribution functions $g(r)$ and $f(r)$. This notation is used only in solving for the shaping functions, for comparison with References [85] and [88], after which we will return to the notation of the main (Fitzpatrick 2010) Reference [69] which was the basis for much of this work. The field distribution functions characterize the equilibrium magnetic field

$$\boldsymbol{B} = B_0\left[f(r)\boldsymbol{\nabla}\phi\times\boldsymbol{\nabla} r + g(r)\boldsymbol{\nabla}\phi\right]. \tag{5.7}$$

According to the typical tokamak ordering

$$g = 1 + \epsilon^2 g_2 + \epsilon^4 g_4 + ..., \tag{5.8}$$

$$f = \epsilon f_1 + \epsilon^3 f_3 + \epsilon^4 f_4 + ..., \tag{5.9}$$

the $O(\epsilon)$ Grad-Shafranov equation determines the pressure balance. The radial functions $S_n(r)$ and $C_n(r)$ are found by the $O(\epsilon^2)$ correction. In order to relate the θ-coordinate in Equations (5.4) and (5.5) to the straight field-line angle ν in the Equation (5.6) form of the Grad-Shafranov equation, we relate the two by the expression

$$\nu(r,\theta) \equiv \frac{2\pi}{L}\int_0^\theta d\theta' \left.\frac{\boldsymbol{B}\cdot\boldsymbol{\nabla}\phi}{\boldsymbol{B}\cdot\boldsymbol{\nabla}\theta'}\right|_r \tag{5.10}$$

$$= \frac{2\pi}{\oint d\theta \frac{J}{R}}\int_0^\theta d\theta \frac{J}{R} = \theta + \epsilon H(r,\theta) + O(\epsilon^2), \tag{5.11}$$

making use of the toroidal geometry properties $\boldsymbol{B}\cdot\boldsymbol{\nabla}\phi \propto R^{-1}$ and $\boldsymbol{B}\cdot\boldsymbol{\nabla}\theta \propto J^{-1}$ described in

D'haeseleer [89] section 4.9.1. Deviations from cylindrical geometry are captured by the function

$$H = r\sin\theta - \sum_n \frac{1}{rn}\left(rS_n' - (n-1)S_n\right)\sin n\theta + \sum_n \frac{1}{rn}\left(rC_n' - (n-1)C_n\right)(\cos n\theta - 1), \tag{5.12}$$

which relates the curvilinear θ coordinate to the straight field line according to

$$\theta = \nu - \epsilon H(r,\theta) + O(\epsilon^2). \tag{5.13}$$

Thus terms with angular dependence can be expanded as

$$a(\theta) = a(\nu) - \epsilon H(\nu)\frac{\partial a}{\partial \theta}(\nu) + O(\epsilon^2). \tag{5.14}$$

The resulting contravariant metric terms, calculated up to $O(\epsilon)$ according to the general coordinate relations found in Appendix A.2, are given by

$$R^2 = 1/\epsilon + [-2r\cos\theta] + O(\epsilon) \tag{5.15}$$

$$\begin{aligned}|\boldsymbol{\nabla} r|^2 =& J^{-2}\left[\left(\frac{\partial R}{\partial \theta}\right)^2 + \left(\frac{\partial Z}{\partial \theta}\right)^2\right] \\ =& 1/\epsilon + \left[-2\Delta'\cos\theta + 2\sum_n S_n'\cos n\theta + 2\sum_n C_n'\sin n\theta\right] + O(\epsilon)\end{aligned} \tag{5.16}$$

$$\begin{aligned}\boldsymbol{\nabla} r\cdot\boldsymbol{\nabla}\theta =& -J^{-2}\left[\frac{\partial R}{\partial r}\frac{\partial R}{\partial \theta} + \frac{\partial Z}{\partial r}\frac{\partial Z}{\partial \theta}\right] + \frac{\partial H}{\partial r}(r,\theta) + O(\epsilon) \\ =& \frac{1}{r}\left[(r\Delta'' + \Delta' + r)\sin\theta - \sum_n \frac{1}{n}\left(rS_n'' + S_n' + (n^2-1)\frac{S_n}{r}\right)\sin n\theta\right. \\ &\left. + \sum_n \frac{1}{n}\left(rC_n'' + C_n' + (n^2-1)\frac{C_n}{r}\right)\cos n\theta - \sum_n \frac{1}{n}\left(rC_n'' - (n-1)C_n' + (n-1)\frac{C_n}{r}\right)\right] + O(\epsilon)\end{aligned} \tag{5.17}$$

Note that the last $O(1)$ term in $\boldsymbol{\nabla} r\cdot\boldsymbol{\nabla}\theta$, while appearing in the contribution to the metric coefficient, will be eliminated by the ∂_θ operator in Equation (5.6) and hence does not affect the shape equations. Plugging these metric terms into the Grad-Shafranov equation ((5.6)), the resulting up-down symmetric shape functions $S_n(r)$ and asymmetric shape functions $C_n(r)$ are found to independently

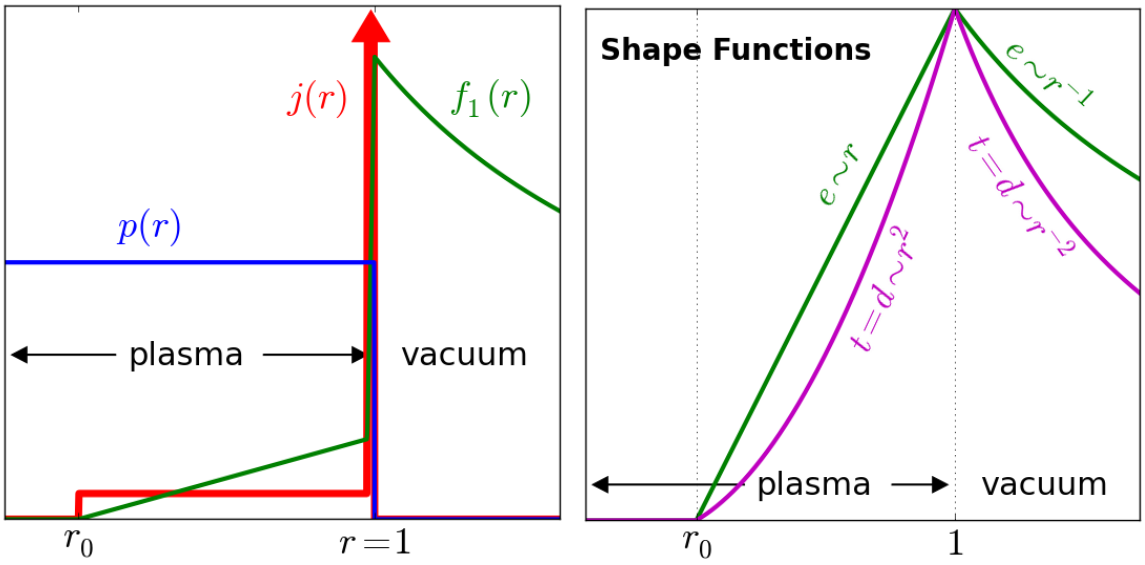

(a) (b)

Figure 5.2: (a) Equilibrium plasma profile used to construct the sharp-boundary model coordinates. The δ-function at the plasma boundary $r = 1$ carries the bulk of the current. A small flat-current region in the plasma permits a non-trivial Grad-Shafranov solution to continue the boundary shape inward. The finite innermost surface r_0 avoids numerical issues near $r = 0$. Also shown are the poloidal field function $f_1(r)$ and the step-function pressure $p(r)$. (b) Grad-Shafranov solution for the shape functions; elongation $e(r)$, triangularity $t(r)$ and up-down (divertor) asymmetry $d(r)$. The surfaces become circular at $r = r_0$ and $r \to \infty$.

satisfy the same equation

$$S_n''(r) + \left(\frac{2(r f_1(r))'}{f_1(r)} - 1 \right) \frac{S_n'(r)}{r} - (n^2 - 1) \frac{S_n(r)}{r^2} = 0, \tag{5.18}$$

$$C_n''(r) + \left(\frac{2(r f_1(r))'}{f_1(r)} - 1 \right) \frac{C_n'(r)}{r} - (n^2 - 1) \frac{C_n(r)}{r^2} = 0, \tag{5.19}$$

Here $f_1(r) = \psi'(r)$ describes the radial poloidal field distribution. As discussed by Conner and Hastie [85], the shape equations are independent of pressure and therefore requires an external origin. Thus Equations (5.18) and (5.19) describe how the shape of the plasma boundary in continued into the plasma.

Shape Profile in a δ-Function Limit

For the present model, the shape functions are resolved in the limit of a δ-function current at the plasma boundary. A pure δ-function current profile has no internal poloidal field ($f = 0$), leading

to a trivial solution to Equation (5.6). In order to permits a non-trivial Grad-Shafranov solution, a small flat-current region is maintained inside the plasma, still assuming that the bulk of current is at the the surface. The combined profile including a δ-function current and flat-current is depicted in Figure 5.2a, including the resulting poloidal field distribution $f_1(r)$ as well as the step-function pressure profile terminating at $r = 1$. The innermost surface $r = r_0$ is kept finite in order to avoid numerical issues near $r = 0$.

A general flat current profile corresponds to a poloidal field distribution $f_1(r) \propto \int const. \propto r$, according to Ampere's law. In the vacuum region beyond the plasma boundary, the poloidal field decreases as $f_1(r) \propto r^{-1}$. Thus the poloidal field function (shown in Figure 5.2a) is given by

$$f_1(r) = \begin{cases} 0, & 0 < r < r_0 \\ (r - r_0), & r_0 < r < 1 \\ (1 - r_0)r^{-1}, & 1 < r \end{cases} . \tag{5.20}$$

In the small innermost region $0 < r < r_0$ there is no poloidal field and thus no magnetic surfaces, so that the shaping equations are trivially satisfied by $S_n = C_n = 0$. In the other three regions the profile above leads to the following shape equations:

$$r_0 < r < 1 : \qquad S_n'' + \left(\frac{3r - r_0}{r - r_0}\right)\frac{S_n'}{r} - (n^2 - 1)\frac{S_n}{r^2} = 0, \tag{5.21}$$

$$1 < r : \qquad S_n'' - \frac{S_n'}{r} - (n^2 - 1)\frac{S_n}{r^2} = 0, \tag{5.22}$$

keeping in mind that the equations for $S_n(r)$ and $C_n(r)$ are identical. Note that the resulting shape equations are independent of the equilibrium current magnitude and the pressure. Taking the limit $r_0 \to 0$ yields the following solution:

$$r < 1 : \qquad S_n, C_n = r^{-1 \pm n}, \tag{5.23}$$

$$1 < r : \qquad S_n, C_n = r^{1 \pm n}. \tag{5.24}$$

The regular solutions are the increasing term in $r < 1$ and the decreasing term in $1 < r$.

Sharp-Boundary Model Parametrization

In the present sharp-boundary formulation, we include the up-down symmetric terms representing elongation $e(r) \equiv S_2$ and triangularity $t(r) \equiv -S_3$, as well as a new up-down asymmetric term $d(r) \equiv -C_3$ which introduces a separate top and bottom triangularity. This radial structure, extending the geometry in Reference [69] with up-down asymmetry, is given by

$$e(r) = e_a \begin{cases} 0, & 0 \le r \le r_0 \\ (r - r_0)/(1 - r_0), & r_0 < r < 1 \\ 1/r, & 1 \le r \end{cases}, \tag{5.25}$$

$$\begin{matrix} t(r) \\ d(r) \end{matrix} = \begin{matrix} t_a \\ d_a \end{matrix} \begin{cases} 0, & 0 \le r \le r_0 \\ r(r - r_0)/(1 - r_0), & r_0 < r < 1 \\ 1/r^2, & 1 \le r \end{cases}. \tag{5.26}$$

The constants in Equations (5.25) and (5.26) are related to the surface shaping parameters in Equations (5.1) and (5.2) by

$$e_a = \frac{\kappa - 1}{\kappa + 1}, \qquad t_a = \frac{2\delta_x}{\kappa + 1}, \qquad d_a = \frac{2\delta_y}{\kappa + 1}. \tag{5.27}$$

These radial shape functions are plotted in Figure 5.2b. As mentioned above, the finite innermost surface $r_0 > 0$ is designated to prevent numerical issues near the magnetic axis ($r = 0$), and to initialize integration through $r_0 < r < 1$ with a series of decoupled cylindrical-like solutions $V_m(r_0) \propto r_0^m$. Note that the coordinates resulting from the internal region solution are *non-orthogonal*. The set of non-orthogonal internal coordinates spanning $r_0 < r < 1$, and orthogonal external coordinates in the region $1 < r$, is depicted in Figure 5.1b. Finally, we express the model parametrization in the form

$$R(r, \theta) = 1/\epsilon + \frac{[r - e(r)] \cos\theta + t(r) \cos 2\theta - d(r) \sin 2\theta}{1 - e_a}, \tag{5.28}$$

$$Z(r, \theta) = \frac{[r + e(r)] \sin\theta - t(r) \sin 2\theta - d(r) \cos 2\theta}{1 - e_a}. \tag{5.29}$$

For concise expression of the regularly appearing geometric factor R/R_0, the non-constant part of R in Equation (5.28) is denoted

$$g(r,\theta) \equiv \frac{[r-e(r)]\cos\theta + t(r)\cos 2\theta - d(r)\sin 2\theta}{1-e_a}, \tag{5.30}$$

so that $R/R_0 = 1+\epsilon g$. This term is evaluated separately for the interior and exterior region, based on Equations (5.25) and (5.26). While the covariant derivatives of $\hat{\boldsymbol{x}} = (R,\phi,Z)$ are straightforward, the contravariant derivatives require evaluation of the Jacobian

$$J = \frac{\partial R}{\partial r}\frac{\partial Z}{\partial \theta} - \frac{\partial R}{\partial \theta}\frac{\partial Z}{\partial r}, \tag{5.31}$$

and the contravariant derivatives

$$\boldsymbol{\nabla} r = \frac{1}{J}\left(\frac{\partial Z}{\partial \theta}\hat{\boldsymbol{R}} - \frac{\partial R}{\partial \theta}\hat{\boldsymbol{Z}}\right), \tag{5.32}$$

$$\boldsymbol{\nabla} \theta = \frac{1}{J}\left(\frac{\partial R}{\partial r}\hat{\boldsymbol{Z}} - \frac{\partial Z}{\partial r}\hat{\boldsymbol{R}}\right). \tag{5.33}$$

The toroidal component satisfies $|\boldsymbol{\nabla}\phi| = R^{-1}(r,\theta)$. These terms are calculated separately for the internal and external coordinates to determine the form of the equations describing the perturbed response. Properties of toroidal flux coordinates as well as generalized coordinate relations are found in Appendices A.1 and A.2.

Internal Metric Coefficients

The internal cross-sectional coordinates described in Equations (5.28), (5.29), (5.25) and (5.26) for $r_0 < r < 1$, which are non-orthogonal, produce the scaled Jacobian

$$\begin{aligned}\widetilde{J} \equiv& \frac{J}{E^2 r} = \frac{1}{E^2 r}\left(\frac{\partial R}{\partial r}\frac{\partial Z}{\partial \theta} - \frac{\partial R}{\partial \theta}\frac{\partial Z}{\partial r}\right)\\ =& 1 - r^{-1}ee' - 2r^{-1}tt' - 2r^{-1}dd' + (r^{-1}e - e')\cos 2\theta\\ &+ r^{-1}(et' + 2te')\cos\theta + (t' - 2r^{-1}t)\cos 3\theta\\ &- r^{-1}(ed' + 2de')\sin\theta - (d' - 2r^{-1}d)\sin 3\theta.\end{aligned} \tag{5.34}$$

Here we have factored out a shape constant

$$E = \frac{1}{1-e_a}, \tag{5.35}$$

which appears in the parametrization Equations (5.28) and (5.29), and thus is carried to all of the metric coefficients derived below:

$$\begin{aligned} a_{rr} \equiv & E^2 \widetilde{J}^2 \boldsymbol{\nabla} r \cdot \boldsymbol{\nabla} r = \frac{1}{r^2 E^2} \left[\left(\frac{\partial Z}{\partial \theta} \right)^2 + \left(\frac{\partial R}{\partial \theta} \right)^2 \right] \\ = & 1 + r^{-2} e^2 + 2 r^{-1} e \cos 2\theta \\ & + 4 r^{-2} t^2 - 4 r^{-2} t e \cos\theta - 4 r^{-1} t \cos 3\theta \\ & + 4 r^{-2} d^2 + 4 r^{-2} d e \sin\theta + 4 r^{-1} d \sin 3\theta, \end{aligned} \tag{5.36}$$

$$\begin{aligned} a_{r\theta} \equiv & r E^2 \widetilde{J}^2 \boldsymbol{\nabla} r \cdot \boldsymbol{\nabla} \theta = -\frac{1}{r E^2} \left[\frac{\partial R}{\partial \theta} \frac{\partial R}{\partial r} + \frac{\partial Z}{\partial \theta} \frac{\partial Z}{\partial r} \right] \\ = & -2 r^{-1} d' t + 2 r^{-1} t' d - (r^{-1} e + e') \sin 2\theta \\ & + r^{-1} (e d' - 2 d e') \cos\theta + (d' + 2 r^{-1} d) \cos 3\theta \\ & + r^{-1} (e t' - 2 t e') \sin\theta + (t' + 2 r^{-1} t) \sin 3\theta, \end{aligned} \tag{5.37}$$

$$\begin{aligned} a_{\theta\theta} \equiv & r^2 E^2 \widetilde{J}^2 \boldsymbol{\nabla} \theta \cdot \boldsymbol{\nabla} \theta = \frac{1}{E^2} \left[\left(\frac{\partial Z}{\partial r} \right)^2 + \left(\frac{\partial R}{\partial r} \right)^2 \right] \\ = & 1 + (e')^2 - 2 e' \cos 2\theta \\ & + (t')^2 - 2 t' e' \cos\theta + 2 t' \cos 3\theta \\ & + (d')^2 + 2 d' e' \sin\theta - 2 d' \sin 3\theta. \end{aligned} \tag{5.38}$$

External Metric Coefficients

In the external region $1 < r$, the coordinate parametrization in Equations (5.28) and (5.29) is designed so that the covariant derivatives satisfy the orthogonality relations

$$\frac{\partial R}{\partial \theta} = -r\frac{\partial Z}{\partial r}, \qquad \frac{\partial Z}{\partial \theta} = r\frac{\partial R}{\partial r}, \tag{5.39}$$

which guarantee orthogonality of the basis vectors. Orthogonality simplifies the metric coefficient h, given by

$$\begin{aligned} h \equiv & \frac{|\partial_\theta \hat{\boldsymbol{x}}|}{r} = |\partial_r \hat{\boldsymbol{x}}| = \frac{1}{|\boldsymbol{\nabla} r|} = \frac{1}{r|\boldsymbol{\nabla}\theta|} \\ = & E\left\{1 + \frac{e_a^2}{r^4} + \frac{4t_a^2}{r^6} + \frac{4d_a^2}{r^6} - \frac{4e_a t_a}{r^5}\cos\theta - \frac{4d_a e_a}{r^5}\sin\theta \right. \\ & \left. + \frac{2e_a}{r^2}\cos 2\theta - \frac{4t_a}{r^3}\cos 3\theta - \frac{4d_a}{r^3}\sin 3\theta\right\}^{1/2}. \end{aligned} \tag{5.40}$$

At the plasma boundary, this metric function reduces to

$$h_a = E\left(1 + e_a^2 + 4t_a^2 - 4e_a t_a\cos\theta + 2e_a\cos 2\theta - 4t_a\cos 3\theta + 4d_a^2 - 4d_a e_a\sin\theta - 4d_a\sin 3\theta\right)^{1/2}, \tag{5.41}$$

expressed in terms of the boundary shape constants defined in Equation (5.27). Now it is convenient to express the θ-line element

$$dl_\theta = rhd\theta, \tag{5.42}$$

the surface area element

$$ds = rhRd\theta d\phi, \tag{5.43}$$

and the volume element

$$d^3x = |\partial_r \hat{\boldsymbol{x}}||\partial_\theta \hat{\boldsymbol{x}}||\partial_\phi \hat{\boldsymbol{x}}| dr d\theta d\phi = rh^2 R dr d\theta d\phi. \tag{5.44}$$

Since the geometry is continuous, these terms apply to plasma boundary calculations on either side of the boundary.

5.2 Equilibrium Pressure Balance

For purpose of developing a set of coordinates satisfying the Grad-Shafranov equation, the previous section incorporated a small flat-current region inside the plasma ($r < 1$). In the interest of simplicity, we now neglect this flat current and assume that the entire equilibrium current is located at the boundary $r = 1$. This allows the equilibrium pressure balance to be determined by a boundary condition at $r = 1$, and the perturbed field to be vacuum-like both inside ($r < 1$) and outside ($r > 1$) of the plasma boundary.

Following the sharp-boundary equilibrium formulation of Freidberg and Grossmann [2], the field inside and outside the plasma boundary is given by

$$\boldsymbol{B} = \frac{B_i}{1 + \epsilon g(r,\theta)} \hat{\boldsymbol{e}}_\phi, \tag{5.45}$$

$$\hat{\boldsymbol{B}} = \frac{1}{1 + \epsilon g(r,\theta)} \hat{\boldsymbol{e}}_\phi + \hat{B}_\theta(r,\theta)\hat{\boldsymbol{e}}_\theta + \hat{B}_r(r,\theta)\hat{\boldsymbol{e}}_r, \tag{5.46}$$

where B_i is the relative magnitude of the internal magnetic field along the magnetic axis ($\theta = \pi/2$), and all fields are scaled by the vacuum on-axis toroidal field strength B_0. The internal domain ($r < 1$) contains only a toroidal field since the equilibrium current is confined to the plasma boundary ($r = 1$). With a step-function pressure terminating at $r = 1$, the boundary poloidal field is determined by the equilibrium pressure balance

$$\hat{B}^2(r = 1_+, \theta) = 2\mu_0 p + B^2(r = 1_-, \theta), \tag{5.47}$$

with $B_r(r = 1) = 0$ and the pressure p is constant on the flux surface $r = 1$. This equilibrium condition, based on the free parameters p and B_i, as well as the inverse aspect ratio and cross-sectional shape parameters, will be used to determine the poloidal field distribution just outside of the plasma boundary. The two parameters p and B_i can be related to the commonly used plasma parameters β and q_a, respectively representing the ratio of fluid to magnetic pressure and the edge safety factor. As a first step, the surface average of Equation (5.47) is used to express the uniform pressure as

$$2\mu_0 p = \frac{\alpha_a \beta B_i^2}{1 - \beta}, \tag{5.48}$$

in terms of

$$\beta \equiv 2\mu_0 p / < \hat{B}^2 > . \tag{5.49}$$

The geometric parameter

$$\alpha_a =< (1+\epsilon g_a(\theta))^{-2} >= \frac{\int_0^{2\pi}(1+\epsilon g_a(\theta))^{-1} h_a(\theta) d\theta}{\int_0^{2\pi}(1+\epsilon g_a(\theta)) h_a(\theta) d\theta}, \tag{5.50}$$

results from the flux surface average of a toroidally symmetric quantity, defined by

$$< A > (r) \equiv \frac{\oint\oint A(r,\theta,\phi) ds}{\oint\oint ds} \tag{5.51}$$

$$= \frac{\int_0^{2\pi} A(r,\theta) R(r,\theta) h(r,\theta) d\theta}{\int_0^{2\pi} R(r,\theta) h(r,\theta) d\theta}. \tag{5.52}$$

Here $h(r,\theta)$ is the external cross-sectional metric function defined by Equation (5.40). We note again that the subscript 'a' denotes evaluation at the boundary. Both $R(r,\theta)$ and $h(r,\theta)$ modify the local arc-length and the resulting local curvature. The average toroidal curvature improves total stability while the local unfavorable curvature focuses the dominant instabilities around the outboard (low-field) side of the torus and around the sharper areas of the plasma cross-section.

Combining Equations (5.45)-(5.48), the poloidal field just outside of the plasma boundary, denoted $\hat{B}_p(\theta) \equiv \hat{B}_\theta\Big|_{r=1+}$, is expressed by

$$\hat{B}_p^2(\theta) = B_i^2 \left(\frac{\alpha_a \beta}{1-\beta} + \frac{1}{(1+\epsilon g_a(\theta))^2} \right) - \frac{1}{(1+\epsilon g_a(\theta))^2}. \tag{5.53}$$

As observed by Freidberg and Grossmann [2], the plasma to vacuum toroidal field ratio B_i is constrained according to

$$\left(1 + (1+\epsilon g_a(\theta_{\min}))^2 \frac{\alpha_a \beta}{1-\beta} \right)^{-1/2} < B_i. \tag{5.54}$$

The lower limit in B_i is set by the condition $\hat{B}_p(\theta_{\min}) \to 0$, which leads to an x-point ($q \to \infty$) approaching the inboard side of the torus, where the resulting pressure is locally balanced by a jump in the toroidal field only. This constraint results in an *equilibrium* β-limit. As discussed in the textbook by Freidberg [49], however, the equilibrium β-limit is generally above the β-limit for MHD instabilities and is therefore not considered in the present analysis. This trend is confirmed for present calculations in Section 6.1 over a variety of aspect-ratios and shaping values. Reference

[2] takes the equilibrium β-limit as an upper bound for the stability limit β_{crit}, in order to avoid explicit computation of the free parameter B_i. As a typical lower value for β_{crit}, Reference [2] adopts a low-β condition of $\beta_p = 1$, physically marked by the transition to a paramagnetic toroidal field and mathematically defined by $B_i = 1$. Presently B_i is explicitly computed by fixing a value of the edge safety factor

$$q_a = \frac{1}{2\pi}\int_0^{2\pi} d\theta \frac{\boldsymbol{B}\cdot\boldsymbol{\nabla}\phi}{\boldsymbol{B}\cdot\boldsymbol{\nabla}\theta} = \frac{1}{2\pi}\int_0^{2\pi} \frac{1}{\hat{B}_p(\theta; B_i^2)} \frac{h_a(\theta)d\theta}{(1+\epsilon g_a(\theta))^2}, \tag{5.55}$$

and numerically solving this transcendental equation, observing the lower bound constraint in Equation (5.54) which appears as a singularity in the integrand. For a choice of q_a this transcendental equation is solved for B_i^2 by Newton's method, noting that the derivative can also be expressed analytically in integral form as

$$\frac{\partial q_a}{\partial(B_i^2)} = \frac{1}{2\pi}\int_0^{2\pi} d\theta \frac{\epsilon h_a(\theta)}{(1+\epsilon g_a(\theta))^2}\left(-\frac{1}{2}\left[\frac{\alpha_a\beta}{1-\beta} + (1+\epsilon g_a(\theta))^{-2}(\theta)\right]\hat{B}_p^{-3}(\theta; B_i^2)\right). \tag{5.56}$$

Thus the equilibrium is characterized by β and q_a, as well as the shape parameters ϵ, κ, δ_x and δ_y.

5.3 Perturbed Field Solution with Tearing Layers and a Resistive Wall

The perturbed magnetic field both inside and outside of the plasma boundary is characterized by a scalar potential

$$\delta\boldsymbol{B} = i\boldsymbol{\nabla}V. \tag{5.57}$$

In the external region with orthogonal coordinates this leads to normal and tangential perturbed fields of the form $\delta B_r \sim \partial_r V$ and $\delta B_\theta \sim V$, reversed from the commonly used flux function $\delta\boldsymbol{B} = \hat{\boldsymbol{b}}\times\boldsymbol{\nabla}\psi$. This means that jumps in the tangential field across layers of skin current are expressed by a discontinuity in V, while the radial derivative $\partial_r V$ must be continuous. The sharp-boundary current profile results in a curl-free perturbed field satisfying Laplace's equation

$$\nabla^2 V = 0, \tag{5.58}$$

everywhere except for the layers of surface current, which impose boundary conditions.

Boundary Conditions

The layers of skin-current, which include the plasma boundary, the resonant tearing layers and the resistive wall, define the perturbed field boundary conditions

$$\left(\frac{\partial(B_\theta\xi)}{\partial\theta}+\frac{\epsilon h}{1+\epsilon g(r,\theta)}\frac{\partial(B_\phi\xi)}{\partial\phi}\right)_{r=1-}=i\,r\frac{\partial V}{\partial r}\bigg|_{r=1-}, \tag{5.59}$$

$$\left(\frac{\partial(B_\theta\xi)}{\partial\theta}+\frac{\epsilon h}{1+\epsilon g(r,\theta)}\frac{\partial(B_\phi\xi)}{\partial\phi}\right)_{r=1+}=i\,r\frac{\partial V}{\partial r}\bigg|_{r=1+}, \tag{5.60}$$

$$\frac{\partial}{\partial\theta}\left[\frac{\epsilon}{h^2}\frac{\partial V}{\partial\theta}\right]_{r_s-}^{r_s+}=-\gamma_D\tau_t\,(1+\epsilon g(r,\theta))r\frac{\partial V}{\partial r}\bigg|_{r_s}, \tag{5.61}$$

$$\frac{\partial}{\partial\theta}\left[\frac{\epsilon}{h^2}\frac{\partial V}{\partial\theta}\right]_{r_w-}^{r_w+}=-\gamma\tau_w\,(1+\epsilon g(r,\theta))r\frac{\partial V}{\partial r}\bigg|_{r_w}, \tag{5.62}$$

$$\left[r\frac{\partial V}{\partial r}\right]_{r_s-}^{r_s+}=\left[r\frac{\partial V}{\partial r}\right]_{r_w-}^{r_w+}=0. \tag{5.63}$$

The ideal boundary condition Equations (5.59) and (5.60), in accordance with Freidberg and Grossmann [2], come directly from the normal component of the ideal induction equation, obtained from Ampere's law along with the ideal-Ohm's law, combined with $\boldsymbol{\nabla}\cdot\boldsymbol{B}=\boldsymbol{\nabla}\cdot\boldsymbol{\xi}=0$. The tearing jump condition in Equation (5.61), following Fitzpatrick [69], is derived by applying $\hat{\boldsymbol{e}}_r\cdot\boldsymbol{\nabla}\times$ to the *non-ideal* induction equation, obtained by keeping finite resistivity in Ohm's law, and integrating across a thin resistive plasma layer with a dissipation time

$$\tau_t\equiv r_s\delta_s\sigma_s, \tag{5.64}$$

where r_s, δ_s and σ_s are the layer (average) radius, thickness and conductivity, respectively. A general derivation of boundary condition for a thin conducting layer is found in the electrodynamics textbook by Jackson [90]. The Doppler-shift in growth rate $\gamma_D\equiv\gamma-in\Omega_s$ is introduced by the plasma surface rotation Ω_s. The perturbed poloidal current on the thin surface scales as $O(\epsilon^2)$, compared to the $O(\epsilon)$ perturbed toroidal current, and is therefore neglected. While this approach allows for different tearing layer regimes, present calculations use a constant-ψ visco-resistive [50, 51] tearing response $\Delta(\gamma_D\tau_t)\propto\gamma_D\tau_t$. The new resistive wall condition is expressed by Equation (5.62)

in terms of the resistive wall dissipation time

$$\tau_w \equiv r_w \delta_w \sigma_w, \tag{5.65}$$

analogous to Fitzpatrick's tearing condition. There is no rotation-induced Doppler shift in Equation (5.62) since the wall is stationary. The resistive wall is induced with perturbed currents in response to all poloidal harmonics, in contrast with the tearing layers which each respond to only a single *resonant* harmonic. The final condition in Equation (5.63) enforces continuity of δB_r. Shape dependence of the geometric coefficients, $g(r,\theta)$ and $h(r,\theta)$, introduces mode-coupling at each surface.

Integration of the perturbed forces across the plasma boundary produces the perturbed force

$$\delta F = \oint \oint ds \left[\frac{\boldsymbol{B}\cdot\delta\boldsymbol{B}}{2} + \boldsymbol{\xi}\cdot\boldsymbol{\nabla}\left(\frac{B^2}{2}\right)\right]_{1_-}^{1_+}. \tag{5.66}$$

In terms of a force matrix defined by $\boldsymbol{\delta F} = \mathcal{F}\boldsymbol{\xi}$, the perturbed energy is written as

$$\delta K + \delta W \propto \sum_{m,k} \xi_m^* \left[(\tau_A \gamma_D)^2 \delta_{mk} + \mathcal{F}_{mk} \right] \xi_k = 0, \tag{5.67}$$

where the Alfvén time τ_A characterizes the timescale of ideal instabilities. This equation defines the growth rate and eigen-structure of the perturbed system. The perturbed force matrix $\mathcal{F}$ is found by solving Laplace's equation subject to the boundary conditions above, as detailed in the following subsections. The solution on either side of the perturbed plasma boundary will be expressed by a multi-harmonic relation between the perturbed tangential and normal fields

$$V_m(1_-) = \sum_k C_{mk}^{(\mathrm{plas})} \left. r\frac{dV_k}{dr}\right|_{1_-}, \tag{5.68}$$

$$V_m(1_+) = \sum_k C_{mk}^{(\mathrm{vac})} \left. r\frac{dV_k}{dr}\right|_{1_+}, \tag{5.69}$$

with the $C^{(\mathrm{vac})}$ matrix incorporating the non-ideal response of the resistive wall and the tearing layer. The perturbed field is then replaced by the perturbed displacement $\boldsymbol{\xi}$ via the induction equation boundary conditions in Equations (5.59) and (5.60). In the absence of resonant surfaces and a resistive wall, the plasma response matrix $C^{(\mathrm{plas})}$ and the no-wall vacuum response matrix $C^{(\mathrm{vac})}$ are computed by radially integrating Laplace's equation on either side of the plasma boundary.

The geometric terms define the Fourier-expanded Laplace equation which is expressed by geometric coupling matrices, calculated by FFT. In the cylindrical limit, internal $r^{|m|}$ and external $r^{-|m|}$ solutions lead to the diagonal response matrices $C_{mk}^{(\mathrm{plas})} = |m|^{-1}\delta_{mk}$ and $C_{mk}^{(\mathrm{vac})} = -|m|^{-1}\delta_{mk}$, respectively. These simple solutions define the initial conditions for the multi-harmonic system, radially launched for each harmonic in order to span the solution space. Broken into a set of coupled first-order ODEs, the system is integrated for each initial condition by a fourth order Runge-Kutta algorithm.

Non-Resonant Plasma Response

The non-resonant plasma response, sometime confusingly referred to as the ideal plasma response, is the response to a magnetic perturbation in the absence of resonant surfaces. The response matrix is calculated by radially integrating Laplace's equation outward, from some finite surface $r_0 > 0$ (to avoid numerical issues near the axis) up to the plasma boundary $r = 1_-$. The geometric information describing the system is contained in the metric coefficients which determine the form of the Laplace equation. Using the previously derived internal metric coefficients from Equations (5.34)-(5.38), the Laplace equation takes the form

$$0 = \frac{\partial}{\partial r}\left[\frac{Ra_{rr}}{\widetilde{J}} r \frac{\partial V}{\partial r} + \frac{Ra_{r\theta}}{\widetilde{J}}\frac{\partial V}{\partial \theta}\right] + \frac{\partial}{\partial \theta}\left[\frac{Ra_{r\theta}}{\widetilde{J}}\frac{\partial V}{\partial r} + \frac{Ra_{\theta\theta}}{r\widetilde{J}}\frac{\partial V}{\partial \theta}\right]. \tag{5.70}$$

The $O(\epsilon^2)$ toroidal term is neglected for consistency. It is convenient to take the Fourier transform before expanding V in the Fourier basis, whereby integration by parts yields a periodic boundary term that vanishes. Fourier expansion then produces

$$0 = \sum_k \left\{\frac{d}{dr}\left(\mathcal{L}_{mk} r \frac{dV_k}{dr} - \frac{m}{k}\mathcal{M}_{mk} V_k\right) - \mathcal{M}_{mk}\frac{dV_k}{dr} + \mathcal{P}_{mk}\frac{1}{r}V_k\right\}, \tag{5.71}$$

in terms of the geometric coupling matrices

$$\mathcal{L}_{mk}(r) = L_{mk}\left\{\frac{1+\epsilon g}{\widetilde{J}} a_{rr}\right\}, \tag{5.72}$$

$$\mathcal{M}_{mk}(r) = L_{mk}\left\{-ik\frac{1+\epsilon g}{\widetilde{J}} a_{r\theta}\right\}, \tag{5.73}$$

$$\mathcal{P}_{mk}(r) = L_{mk}\left\{-mk\frac{1+\epsilon g}{\widetilde{J}} a_{\theta\theta}\right\}. \tag{5.74}$$

This notation makes use of a Fourier coupling operator defined by

$$L_{mk}\{y\} \equiv \frac{1}{2\pi}\int_0^{2\pi} y(\theta)\exp[i(k-m)\theta]d\theta. \tag{5.75}$$

The components of the coupling matrices are computed by complex FFT. Symmetry relations

$$\mathcal{L}_{mk} = \mathcal{L}_{km}, \qquad \mathcal{M}_{mk} = -\frac{m}{k}\mathcal{M}_{km}, \qquad \mathcal{P}_{mk} = \mathcal{P}_{km}, \tag{5.76}$$

are used to further simplify the calculation. For computational purposes, it is desirable to convert the system of 2nd order ODEs in r to a larger system of 1st order ODEs. Swapping $m \leftrightarrow m'$ and making use of the symmetry relations yields the desired form

$$r\frac{dV_m}{dr} = \sum_k \left(\mathcal{Q}_{mk}\psi_k - \mathcal{R}_{mk}V_k\right), \tag{5.77}$$

$$r\frac{d\psi_m}{dr} = \sum_k \left(\mathcal{R}_{km}\psi_k - \mathcal{S}_{mk}V_k\right). \tag{5.78}$$

This form makes use of a new variable

$$\psi_k \equiv \sum_{m'}\left(\mathcal{L}_{km'}r\frac{dV_{m'}}{dr} + \mathcal{M}_{km'}V_{m'}\right), \tag{5.79}$$

as well as modified coupling matrices

$$\mathcal{Q}_{mm'}(r) = (\mathcal{L}^{-1})_{m'm}, \tag{5.80}$$

$$\mathcal{R}_{mm'}(r) = \sum_k (\mathcal{L}^{-1})_{mk}\mathcal{M}_{km'}, \tag{5.81}$$

$$\mathcal{S}_{mm'}(r) = \sum_k \mathcal{M}_{km}\mathcal{R}_{km'} + \mathcal{P}_{mm'}. \tag{5.82}$$

Using a fourth order Runge-Kutta algorithm, the set of equations (5.77) and (5.78) is integrated radially over the interior region $r_0 < r < 1$ to obtain the non-resonant component of the plasma response. Integration is initialized using the simplified geometry near the axis, $0 < r < r_0$, where the coupling matrices reduce to

$$Q_{mm'} = \delta_{mm'}, \qquad R_{mm'} = 0, \qquad S_{mm'} = -m^2\delta_{mm'}, \tag{5.83}$$

thereby converting the coupled system to a set of uncoupled cylindrical Laplace equations, having the familiar solution

$$V_j = b_j r^{|j|}, \qquad \psi_j = r\frac{dV_j}{dr} = b_j |j| r^{|j|}, \tag{5.84}$$

for each j. The $r^{-|j|}$ term is eliminated for regularity at $r = 0$. Since the goal is to write a linear plasma response relation between V_j and ψ_j at the plasma boundary (where $\psi \sim rdV/dr$ due to orthogonality), the constant b_j scales out. Each j'th analytic solution on $0 \le r \le r_0$ can be used to define an initial condition (at r_0) for a numerical solution over the coupled region $r_0 < r < 1$. Each component initialized by $r^{|j|}$ is integrated outward from the plasma center toward the plasma boundary, where the plasma response is evaluated. Let $V_m^j(r)$ be defined as the magnetic potential component V_m given an initial perturbation $r^{|j|}$. Since the solutions start out uncoupled at $r = r_0$, the initial condition can be written

$$V_m^j(r_0) = r_0^{|j|}\delta_{jm}, \tag{5.85}$$

$$\psi_m^j(r_0) = |j| r_0^{|j|}\delta_{jm}. \tag{5.86}$$

Integration of (5.77) and (5.78) evolves the perturbations up to the $r = 1_-$ surface, where the solution is denoted

$$V_m^j(1_-) = A_{jm}, \tag{5.87}$$

$$\psi_m^j(1_-) = B_{jm}. \tag{5.88}$$

Thus the internal plasma response is captured by a set of conditions at the plasma boundary. The response matrix is found by a linear relation between matrices A_{jm} and B_{jm}:

$$A_{jm} = \sum_k B_{jk} C_{km}^{(\mathrm{plas})} + \delta_{0j}\delta_{0m}, \tag{5.89}$$

with the second term on the right hand side added to compensate for $B_{0k} = B_{j0} = 0$. Finally, the non-resonant plasma response matrix $C^{(\mathrm{plas})}$ is obtained by taking the pseudo-inverse of the singular matrix B:

$$C^{(\mathrm{plas})} = B^{\dagger}(A - I_{00}). \tag{5.90}$$

Here $B^\dagger$ is the pseudo-inverse and $I_{00} = \delta_{0j}\delta_{0m}$ is a matrix of zeros except for unity in the center. In accordance with Fitzpatrick [69] as well as the more detailed discussion of Freidberg and Grossmann [2], symmetry must be enforced to account for small errors introduced by the finite size of the matrices. In this process the arbitrary values for the column C_{0m}, introduced by the $m = 0$ singularity in B, are replaced by the row values C_{m0}. Note also that the addition of up-down asymmetry makes the coupling matrices complex, so that the real symmetry condition is replaced by Hermitian symmetry. As mentioned before, in the cylindrical limit $r^{|m|}$ solutions lead to a diagonal response matrix $C_{mk}^{(\text{plas})} \to |m|^{-1}\delta_{mk}$.

Vacuum Response

In the absence of a conducting wall, the vacuum response is computed similarly to the non-resonant plasma response, by radially integrating Laplace's equation inward up to the boundary. The geometric terms define the Fourier-expanded Laplace equation which is expressed by a geometric coupling matrix, calculated analytically at $O(\epsilon)$ for the external region. Including the toroidal curvature term, Laplace's equation now takes the form

$$r\frac{d}{dr}\left(r\frac{dV_m}{dr}\right) - m^2 V_m = -\sum_k X^r_{mk} r\frac{dV_k}{dr}, \tag{5.91}$$

in terms of the analytic coupling matrix

$$\begin{aligned} X^r_{mk} =& L_{mk}\left\{\epsilon r\frac{\partial g}{\partial r}\right\} \\ =& \epsilon E\left[\left(r+\frac{e_a}{r}\right)\frac{1}{2}\left(\delta_{m+1,k}+\delta_{m-1,k}\right) - \frac{t_a}{r^2}\left(\delta_{m+2,k}+\delta_{m-2,k}\right) - i\frac{d_a}{r^2}\left(\delta_{m+2,k}-\delta_{m-2,k}\right)\right]. \end{aligned} \tag{5.92}$$

The Kronecker-δ matrices $\delta_{m,k\pm1}$ and $\delta_{m,k\pm2}$ show how elongation introduces additional $m \pm 1$ coupling, and triangularity and up-down asymmetry introduce $m \pm 2$ coupling. As before, $E = 1/(1-e_a)$ (Equation (5.35)). Note that the toroidal curvature variation $g(r,\theta)$, which is neglected in the error-field calculations of Fitzpatrick [69], plays an important role in the present stability calculations and ensuing mode structure. While neglecting this toroidal correction in the vacuum region is found to be inconsequential for a circular cross-section, confirming previous assertions that shaping effects predominantly impact domains of perturbed current [37, 91], an observable mode-coupling effect is observed in the presence of cross-sectional shaping.

Starting at the wall surface $r = r_w$, solutions for the multi-harmonic system are radially launched for each harmonic in order to span the solution space, as described in the subsection above for the non-resonant plasma response. The result is the vacuum response matrix $C^{\,(\mathrm{vac})}$ required for Equation (5.69). In the cylindrical limit, analytic $r^{-|m|}$ solutions lead to a diagonal form $C^{(\mathrm{vac})}_{mk} \rightarrow -|m|^{-1}\delta_{mk}$. The next two subsections describe how this vacuum response matrix is extended in the presence of a resistive wall and resonant tearing surfaces.

Resistive Wall Contribution to the Vacuum Response

With the addition of a resistive wall, defined for convenience to be conformal to a flux surface $r = r_w$, the new model introduces a modification to the vacuum response expressed by Equation (5.69). Expanded in the standard Fourier basis, the wall boundary condition in Equation (5.62) becomes

$$\sum_k \left(\hat{\tau}^{(\mathrm{wall})}_{mk}\right)^{-1} [V_k]^{r_{w+}}_{r_{w-}} = \gamma\tau_w \sum_k U^{(\mathrm{wall})}_{mk} r \left.\frac{dV_k}{dr}\right|_{r_w} . \tag{5.93}$$

The shaped wall coupling matrices are given by

$$U^{(\mathrm{wall})}_{mk} \equiv L_{mk}\left\{1 + \epsilon g_w(\theta)\right\}, \tag{5.94}$$

$$\left(\hat{\tau}^{(\mathrm{wall})}_{mk}\right)^{-1} \equiv L_{mk}\left\{\frac{mk\epsilon}{h^2_w(\theta)}\right\}, \tag{5.95}$$

expressed in terms of a Fourier coupling operator defined in Equation (5.75). In the up-down symmetric case where $\delta_t = \delta_b = \delta$, it suffices to calculate Fourier integrals over $0 < \theta < \pi$ and take only the real (cosine) component, while general asymmetric geometry requires evaluation over the entire circumference and inclusion of the imaginary (sine) component. An important feature of the coupling matrix $U^{(\mathrm{wall})}$ is the presence of the geometric terms $g_w(\theta) \equiv g(r_w, \theta)$ and $h_w(\theta) = h(r_w, \theta)$, according to Equations (5.30) and (5.40), which couple wall currents of different harmonic structure. In addition, the wall boundary condition contains a geometric time factor $\hat{\tau}^{(\mathrm{wall})}$ associated with the wall time τ_w. Both the toroidicity matrix $U^{(\mathrm{wall})}$ and the geometric time factor matrix $\hat{\tau}^{(\mathrm{wall})}$ become diagonal in the cylindrical limit. Geometric coupling in the wall plays a key role in this sharp-boundary model, where the total mode structure is strongly affected by the interdependence of the tearing layer and the wall. The harmonic structure of the wall currents is now captured by the jump of the tangential field. Borrowing from the notation of tearing mode theory, the harmonic

structure of the wall currents is captured by the jump of the tangential field

$$[V_m]_{r_{w-}}^{r_{w+}} = \sum_k C_{mk}^{(\mathrm{wall})}(\gamma\tau_w)\, r\frac{dV_k}{dr}\bigg|_{r_w}, \tag{5.96}$$

written in terms of the resistive wall response matrix

$$C_{mk}^{(\mathrm{wall})} = \gamma\tau_w \sum_{m'} \hat{\tau}_{mm'}^{(\mathrm{wall})} U_{m'k}^{(\mathrm{wall})}. \tag{5.97}$$

The wall jump condition in Equation (5.96) along with the δB_r continuity condition in Equation (5.63) enter the $\gamma\tau_w$-dependent resistive-wall vacuum response matrix

$$C_{mk}^{(\mathrm{vac\text{-}rw})}(\gamma\tau_w) = C_{mk}^{(\mathrm{vac})} - r_w^{-2|k|} W_{mk}^{-1}(\gamma\tau_w), \tag{5.98}$$

with the wall contribution given by

$$W_{mk} = \frac{|m|}{2}(1 - r_w^{-2|m|})\delta_{mk} + {C_{mk}^{(\mathrm{wall})}}^{-1}(\gamma\tau_w). \tag{5.99}$$

The first term in Equation (5.98) represents the no-wall vacuum response, recovered in the limit $r_w \to \infty$. The ideal wall limit $\tau_w \to \infty$ forces the condition $\delta B_r(r_w) = 0$ at the wall. In this case the second term in Equation (5.99) vanishes. The uncoupled ideal-wall response of Freidberg and Haas [80] is recovered in the present formulation by taking the cylindrical limit, whereby

$$C_{mk}^{(\mathrm{vac\text{-}rw})} \to -|m|^{-1}\frac{1 + r_w^{-2|m|}}{1 - r_w^{-2|m|}}\delta_{mk}. \tag{5.100}$$

as in Freidberg and Haas [80]. Since the wall factor above is larger than unity, the vacuum has a positive contribution to the energy balance and the effect of the ideal wall is always stabilizing.

Tearing Layer Contribution to Vacuum Response

The tearing layers, based on those formulated in an error-field response model by Fitzpatrick [69], also contribute in this model to the field response of the vacuum region, which can be thought of as a resistive plasma with no equilibrium current as portrayed by Finn [5]. This approximation allows the sharp-boundary model to have rational surfaces despite having $B_\theta = 0$ and $q = \infty$ in the interior

region $r < 1$. The tearing layer imposes a boundary condition only on its corresponding resonant harmonic. The formulation of Reference [69] is extended to include the local toroidal curvature term $g_m(\theta) \equiv g(r_m, \theta)$ for each rational m/n surface located at $r_m > 1$. A straight field-line angle

$$\nu_m(\theta) = \int_0^\theta \frac{\epsilon h_m(\theta)}{q_m \hat{B}_m(\theta)(1+\epsilon g_m(\theta))^2} d\theta, \tag{5.101}$$

is used to evaluate the resonant component at the shaped surface. Here the subscript m denotes evaluation at the resonant m/n-surface, with a fixed toroidal harmonic $n = 1$. Assuming that the equilibrium poloidal field $\hat{B}_m = \hat{B}_\theta(r = r_m)$ can be approximated by the same functional form at r_m as at $r = 1_+$, the resonant-surface poloidal field distribution is solved analogously to Equations (5.53) and (5.55), now with $q_m = m/n$ leading to a different free parameter to replace B_i. In terms of the straight field-line, the total jump across the rational surface r_m is expanded in terms of its sub-harmonics:

$$[V]_{r_{m-}}^{r_{m+}} = (1+\epsilon g_m(\theta)) \sum_{m'} [V_{m'}]_{r_{m-}}^{r_{m+}} e^{i[m'\nu_m(\theta) - n\phi]}. \tag{5.102}$$

Neglecting all non-resonant components of the surface response, the Fourier inverse of the equation above reduces to

$$[V_{m'}]_{r_{m-}}^{r_{m+}} = [V_m]_{r_{m-}}^{r_{m+}} U_{m'm}^{(\text{tear})} \quad \text{(no sum)}, \tag{5.103}$$

written in terms of a tearing surface coupling matrix

$$U_{m'm}^{(\text{tear})} \equiv \frac{1}{2\pi} \int_0^{2\pi} (1+\epsilon g_m(\theta)) \cos[m\nu_m(\theta) - m'\theta] d\theta. \tag{5.104}$$

Applying the straight field-line expansion in Equation (5.102) to the tearing boundary condition in Equation (5.61) yields the resonant layer response

$$[V_{m'}]_{r_{m-}}^{r_{m+}} = \gamma_D \tau_m \hat{\tau}_m^{(\text{tear})} \sum_k U_{m'm}^{(\text{tear})} U_{km}^{(\text{tear})^*} r \left. \frac{dV_k}{dr} \right|_{r_m}, \tag{5.105}$$

for each rational surface r_m. Each has a corresponding layer time τ_m and associated geometric time factor

$$\hat{\tau}_m^{(\text{tear})} \equiv \left\{ \frac{1}{2\pi} \int_0^{2\pi} d\theta \left(\frac{\epsilon^3 n^2}{\hat{B}_m^2(\theta)(1+\epsilon g_m(\theta))^4} \right) \right\}^{-1}, \tag{5.106}$$

analogous to the wall matrix in Equation (5.95) corresponding to multi-harmonic geometric time factor. The formulation of Reference [69] neglects this tearing layer integral, effectively applying a cylindrical low-β approximation. Noting the typical tokamak ordering of the poloidal field $\hat{B}_m = \hat{B}_\theta(r = r_m) \sim \epsilon$, the integrand above appears as $O(\epsilon^3)$ but is actually $O(\epsilon)$.

Following Reference [69], the layer response is simplified in the limit where the rational surfaces all lie just outside of the plasma edge, similar to a diverted plasma where $q_a \to \infty$. In this way the resonant surfaces are combined by taking $r_m \to 1_+$, $\tau_m \to \tau_t$, $\Omega_m \to \Omega$, $h_m(\theta) \to h_a(\theta)$, and $g_m(\theta) \to g_a(\theta)$. This also reduces the number of domains for radial integration. Note that artificial singularities at the plasma boundary are avoided by calculating the equilibrium field distribution $\hat{B}_m(\theta)$ at the resonant layer with $q_m \neq q_a$. With a unique poloidal field distribution, each layer maintains its own geometric coupling matrix $U^{(\text{tear})}$ and geometric time factor $\hat{\tau}^{(\text{tear})}$. After taking the limit and summing over all rational surfaces $q_0 < q_m < q_a$, the total resonant response at $r_m \to r_s \to 1_+$ is written as

$$[V_{m'}]_{r_{s-}}^{r_{s+}} = \sum_k C_{m'k}^{(\text{tear})} (\gamma_D \tau_t) r \left. \frac{dV_k}{dr} \right|_{r_s}, \tag{5.107}$$

in terms of the tearing layer response matrix

$$C_{m'k}^{(\text{tear})} = \gamma_D \tau_t \sum_{m_0 \leq m \leq m_1} \hat{\tau}_m^{(\text{tear})} U_{m'm}^{(\text{tear})} U_{km}^{(\text{tear})^*}, \tag{5.108}$$

which combines all of the relevant rational surfaces in the range $nq_0 < m_0 \leq ... \leq m_1 < nq_a$. This tearing formulation agrees with that of Reference [69] for the case of high aspect-ratio and up-down symmetry.

In the language of tearing theory, the inner solution is given by a constant-ψ visco-resistive [50, 51] diagonal matrix $\Delta_{mk}(\gamma_D \tau_t) = \gamma_D \tau_t \delta_{mk}$ (whereas the other terms in Equation (5.107) all belong to the outer solution Δ'). Other tearing regimes may be conveniently substituted into this formulation by replacing the linear $\gamma_D \tau_t$ with different functional forms (for example $(\gamma_D \tau_t)^{5/4}$ in the resistive-inertial regime), while keeping the geometric coupling terms unchanged. The matching condition $r_{s-} = 1_+$ is used to combine the resonant response above with the wall dependent vacuum

response in Equation (5.98), resulting in the combined vacuum-wall-tearing response

$$V_m(1_+) = \sum_k \left(C_{mk}^{(\text{vac-rw})}(\gamma\tau_w) - C_{mk}^{(\text{tear})}(\gamma_D\tau_t) \right) r \left. \frac{dV_k}{dr} \right|_{r=1_+} . \tag{5.109}$$

5.4 Multi-Mode Dispersion Relation

Using the ideal boundary conditions in Equations (5.59) and (5.60), the total perturbed force matrix defined in Equation (5.66) takes the form

$$\mathcal{F} \equiv -H + G^\dagger C^{\,(\text{plas})}\, G - \hat{G}^\dagger \left(C^{(\text{vac-rw})}(\gamma\tau_w) - C^{(\text{tear})}(\gamma_D\tau_t) \right) \hat{G}, \tag{5.110}$$

which contains contributions of the non-resonant plasma, vacuum (including the resistive wall) and resonant tearing response. The resistive wall and tearing terms are γ-dependent and therefore make the force matrix non-self-adjoint. The three additional matrices, H, G and $\hat{G}$, respectively associated with the surface, internal and external solutions, are given by

$$H_{mk} = L_{mk} \left\{ \frac{B_p^2 (1+\epsilon g_a)^2 h_a'}{h_a^2} + (1 - B_i^2)(1+\epsilon g_a) g_a' \right\}, \tag{5.111}$$

$$G_{mk} = L_{mk} \left\{ \left(-nB_i \epsilon \frac{h_a}{1+\epsilon g_a} \right) \right\}, \tag{5.112}$$

$$\hat{G}_{mk} = L_{mk} \left\{ \left(m(1+\epsilon g_a)\hat{B}_p - n\epsilon \frac{h_a}{1+\epsilon g_a} \right) \right\}, \tag{5.113}$$

This form makes use again of the Fourier coupling operator defined in Equation (5.75), as well as the geometric functions

$$h_a'(\theta) \equiv \left. \frac{1}{2} \frac{\partial([rh]^2)}{\partial r} \right|_{r=1}, \tag{5.114}$$

$$g_a'(\theta) \equiv \left. \epsilon r \frac{\partial g}{\partial r} \right|_{r=1} . \tag{5.115}$$

This categorization of energy contributions in the sharp-boundary model is discussed in Freidberg's *Ideal MHD* textbook, where it is referred to as the *extended energy principle*. The derivation of the three contributions is found below.

Surface Contribution

The perturbed surface contribution, denoted H in the force matrix above, comes from the second term of the MHD perturbed force expression in Equation (5.66). Evaluating this term just inside of the plasma boundary ($r = 1_-$), where there is no poloidal field, leads to

$$(\xi\hat{\boldsymbol{e}}_r)\cdot\boldsymbol{\nabla}\left(\frac{B_\phi^2}{2}\right)_{r=1_-} = -\xi\frac{\epsilon B_i^2}{h(1+\epsilon g)^3}\frac{\partial g}{\partial r}\bigg|_{r=1_-}. \tag{5.116}$$

Similar to the expression above, the toroidal field contribution outside of the plasma boundary ($r = 1_+$) is

$$(\xi\hat{\boldsymbol{e}}_r)\cdot\boldsymbol{\nabla}\left(\frac{\hat{B_\phi}^2}{2}\right)_{r=1_+} = -\xi\frac{\epsilon}{h(1+\epsilon g)^3}\frac{\partial g}{\partial r}\bigg|_{r=1_+}, \tag{5.117}$$

which is the same as inside except for the absent B_i^2 factor. Outside there is an additional poloidal field contribution given by

$$(\xi\hat{\boldsymbol{e}}_r)\cdot\boldsymbol{\nabla}\left(\frac{\hat{B_\theta}^2}{2}\right)_{r=1_+} = -\xi\frac{\hat{B_p}^2}{2h^3}\left.\frac{\partial[rh(r,\theta)]^2}{\partial r}\right|_{r=1_+}. \tag{5.118}$$

Here we use the radial dependence of the poloidal field, which according to Ampere's law is given by

$$\hat{B}_\theta(r,\theta) = \frac{\hat{B}_p(\theta)h_a(\theta)}{rh(r,\theta)}. \tag{5.119}$$

The total surface term becomes

$$\left[\!\left[\boldsymbol{\xi}\cdot\boldsymbol{\nabla}\left(\frac{B^2}{2}\right)\right]\!\right]_{1-}^{1+} = -\left(\frac{B_p^2 h_a'}{h_a^3} + \frac{1-B_i^2}{h_a(1+\epsilon g_a)^3}\epsilon g_a'\right)\xi, \tag{5.120}$$

using the geometric functions h_a' and g_a' defined in Equations (5.114) and (5.115). The expansion of the perturbed surface displacement (normal to the surface) is chosen to be

$$\xi(\theta,\phi) = (1+\epsilon g_a(\theta))\sum_m \xi_m e^{i(m\theta-n\phi)}, \tag{5.121}$$

as in Freidberg and Grossmann [2], in order to preserve the symmetric form of the energy matrices. The surface integrated contribution is now expressed in a Fourier basis as

$$\delta F_m^{\text{surf}} = -\sum_{m'} H_{mm'}\xi_{m'}, \tag{5.122}$$

in terms of the surface energy matrix defined in Equation (5.111).

Plasma Contribution

The plasma volume contribution to the perturbed force matrix is calculated in three steps outlined below.

1. The first perturbed force term in Equation (5.66) is written in terms of the field-line operator $\boldsymbol{B}\cdot\boldsymbol{\nabla}$ and the magnetic potential:

$$\boldsymbol{B}\cdot\delta\boldsymbol{B} = (\boldsymbol{B}\cdot\boldsymbol{\nabla})iV. \tag{5.123}$$

On the inside of the plasma boundary, where $B_r = B_\theta = 0$, the field-line operator is given by

$$\boldsymbol{B}\cdot\boldsymbol{\nabla}|_{r=1_-} = B_\phi|\boldsymbol{\nabla}\phi|\partial_\phi = -\frac{in\epsilon B_i}{(1+\epsilon g_a(\theta))^2}. \tag{5.124}$$

Equations (5.124) and (5.43) are now used to write the surface integrated plasma contribution

$$-\frac{\epsilon}{(2\pi)^2}\left(\oint\oint ds\boldsymbol{B}\cdot\delta\boldsymbol{B}\right)_{r=1_-}^{(m)} = \sum_{m'} G^*_{m'm}V_{m'}\Big|_{r=1_-}, \tag{5.125}$$

in terms of the plasma energy matrix defined in Equation (5.112). As a consequence of the G matrix being non-diagonal, there is a difference in the harmonic structure of the perturbed fields versus the perturbed surface displacement. This effect, pointed out in section 7.4 of Bateman's textbook *MHD Instabilities* [79], represents an important departure from single-mode theory. When discussing the harmonic structure in real geometry, it is necessary to specify if referring to the fields or the displacement.

2. Next, using the non-resonant plasma response matrix from Equation (5.90), the plasma re-

sponse Equation (5.68), repeated here for convenience;

$$V_m(1_-) = \sum_k C_{mk}^{(\mathrm{plas})}\, r\frac{dV_k}{dr}\bigg|_{r=1_-},$$

is used to relate the magnetic potential to the perturbed normal field.

3. Finally the normal field is related to the perturbed surface by the normal component of the induction equation

$$\hat{\boldsymbol{e}}_r\cdot\delta\boldsymbol{B} = i\frac{r}{h_a}\frac{\partial V}{\partial r} = (\boldsymbol{B}\cdot\boldsymbol{\nabla})\xi - \xi\hat{\boldsymbol{e}}_r\cdot(\hat{\boldsymbol{e}}_r\cdot\boldsymbol{\nabla})\boldsymbol{B}. \tag{5.126}$$

Making use of $\boldsymbol{\nabla}\cdot\boldsymbol{B} = 0$, the equation above reduces to

$$i\frac{r}{h_a}\frac{\partial V}{\partial r} = h_a^{-1}\partial_\theta\left(B_\theta\xi\right) + B_\phi|\boldsymbol{\nabla}\phi|\partial_\phi\xi. \tag{5.127}$$

Setting $B_\theta = 0$ inside the plasma boundary, along with the modified perturbed surface expansion (5.121), leads to

$$r\,\frac{dV_k}{dr}\bigg|_{r=1_-} = \sum_{m''} G_{km''}\xi_{m''}. \tag{5.128}$$

Combining the three steps yields the desired form

$$\delta F_m^{\mathrm{plasma}} = \sum_{m',k,m''} G_{m'm}^{*} C_{m'k}^{(\mathrm{plas})} G_{km''}\xi_{m''}. \tag{5.129}$$

Vacuum Contribution

The vacuum contribution to the perturbed force matrix, calculated at $r = 1_+$, follows the same three step procedure as the plasma contribution calculated above.

1. Again using Equation (5.123), the field-line operator

$$\boldsymbol{B}\cdot\boldsymbol{\nabla}|_{r=1_+} = \frac{im'\hat{B}_p(\theta)}{h_a(\theta)} - \frac{in\epsilon}{(1+\epsilon g_a)^2(\theta)}, \tag{5.130}$$

is used to write the surface integrated force as

$$\frac{\epsilon}{(2\pi)^2}\left(\oint\oint ds\boldsymbol{B}\cdot\delta\boldsymbol{B}\right)^{(m)}_{r=1_+} = -\sum_{m'}\hat{G}^{*}_{m'm}V_{m'}\bigg|_{r=1_+}, \tag{5.131}$$

in terms of the vacuum matrix defined by (5.113) and the magnetic potential.

2. Next the combined vacuum-wall-tearing response Equation (5.109), repeated here for convenience;

$$V_m(1_+) = \sum_k \left(C_{mk}^{(\mathrm{vac})} - C^{(\mathrm{tear})}{}_{mk} \right) r \frac{dV_k}{dr}\bigg|_{r=1_+},$$

relates the perturbed potential and the perturbed normal field.

3. Finally the normal component of the induction equation, as expressed in Equation (5.127) and now including the poloidal field beyond the boundary, relates the normal field to the normal component of the perturbed surface displacement

$$r \frac{dV_k}{dr}\bigg|_{1_+} = \sum_{m''} \hat{G}_{km''} \xi_{m''}. \tag{5.132}$$

Combining the three steps yields the desired form

$$\delta F_m^{\mathrm{vac}} = \sum_{m',k,m''} \hat{G}^*_{m'm} \left(C^{(\mathrm{tear})}{}_{m'k} - C_{m'k}^{(\mathrm{vac})} \right) \hat{G}_{km''} \xi_{m''}. \tag{5.133}$$

Multi-Mode MHD Dispersion Relation

In terms of the non-ideal perturbed force matrix, the energy balance problem portrayed in Equation (5.67) can be expressed as a non-linear eigenvalue problem

$$\left[(\tau_A \gamma_D)^2 I + \mathcal{F}(\gamma\tau_w, \gamma_D \tau_t) \right] \boldsymbol{\xi} = 0. \tag{5.134}$$

In contrast with the ideal model of Freidberg and Grossmann [2], this new non-ideal dispersion relation produces mode behavior on three different timescales, τ_A, τ_w and τ_t, and can be used to study transitions between phenomena on different timescales. A similar multi-mode dispersion relation was formulated in a circular cross-section toroidal model by Betti [37].

In the cylindrical limit, the response matrices have an infinite contribution from the $m = 0$ component. Due to the large aspect ratio approximation, it is necessary to enforce the incompressibility constraint $\xi_0 = 0$, expressed by the $m = 0$ component of Equations (5.59) and (5.60):

$$r \frac{dV_0}{dr}\bigg|_{1_-} = r \frac{dV_0}{dr}\bigg|_{1_+} = 0. \tag{5.135}$$

From Equations (5.59) and (5.60) it is observed that deviations from cylindrical geometry make the harmonic content of the surface displacement distinct from that of the perturbed field, so that $m \neq 0$ components of the normal displacement ξ may contribute to the $m = 0$ component of δB_r. By the definitions of G and $\hat{G}$ in Equations (5.112) and (5.113), it is observed that $G_{0m} = B_i \hat{G}_{0m}$ and hence the incompressibility constraint both inside and outside is satisfied by

$$\boldsymbol{g}^\dagger \boldsymbol{\xi} = 0, \qquad \boldsymbol{g}_m = \frac{G_{0m}}{(\sum_k G_{0k} G_{0k})^{1/2}}. \tag{5.136}$$

Following Freidberg and Haas [54], a projection operator $P = I - \boldsymbol{g}\boldsymbol{g}^\dagger$ is used to eliminate the subspace of compressible solutions, with $P\boldsymbol{g} = 0$. The constraint above is automatically satisfied by the reformulation

$$\left[(\tau_A \gamma_D)^2 I + P\mathcal{F}(\gamma\tau_w, \gamma_D \tau_t)P\right] \boldsymbol{\xi} = 0 \tag{5.137}$$

which forces the trivial solution $\gamma_D = 0$ to accompany the incompressible component $\boldsymbol{\xi} = \boldsymbol{g}$. This method is extended here from the formulation of Freidberg and Haas to the non-linear eigenvalue problem with a γ-dependent force matrix.

The non-linear eigenvalue problem in Equation (5.137) is solved for the dominant mode. In principle it is possible to manipulate this system into a polynomial form which may be converted into a larger linear system. This approach, however, requires inverting the $\hat{G}$ matrix which can become singular, analogous to the single mode resonance $\boldsymbol{B}\cdot\boldsymbol{\nabla} \to 0$. Instead we adopt the direct approach of minimizing the absolute value of the system determinant with respect to γ.

In the absence of plasma rotation, the dominant mode γ is purely real [36]. Solutions with complex frequencies that appear due to additional tearing layer physics [92] are beyond the scope of the present study. The mode with largest γ is found by initiating a 1-D Newton solver at large γ and converging to the solution from above. In order to find the dominant mode, the initial calculation is carried out at large β where the dominant growth rate lies well above zero (near the top of the ip-iw dome shown in Figure 6.3 in the next chapter). This first calculated growth rate is then used as an initial guess for further calculations as β is ramped down toward the point of marginal stability $\gamma = 0$. The same method is applied with other parameters as well (e.g. q_a in the inset of Figure 6.3 in the next chapter). Calculating the entire growth rate curve, rather than just the marginal stability points, has the benefit of showing how the mode transitions between the ideal, wall and tearing timescales. The addition of plasma rotation Ω introduces rotation of the dominant mode

and thus requires a 2-D search over complex γ. Rotation is varied starting with the same initial calculation at high β and zero rotation. Any point on this branch of rotation values (at fixed high β) can be then used to initiate a β scan in the presence of fixed rotation. A reliable 2-D minimizer for this application was determined to be the Nelder-Mead algorithm [93] found in the Scientific Python (*SciPy* [94])) library.

The corresponding eigenvector, describing the mode structure, is obtained by a singular value decomposition (SVD) of the system after plugging in the dominant eigenvalue. The desired vector is associated with the smallest of the (non-negative real) singular values of the decomposition, which in the absence of computational errors equals exactly zero (i.e. the system null space).

The entire model is implemented in Python on a personal computer. Calculation of certain geometric quantities can take approximately 10 seconds, after which each stability calculation is performed in approximately 1 second. Appendix B provides more details regarding the code implementation, as well as some example calculations for the first time user. The next chapter presents the results discovered using this new sharp-boundary model.

Chapter 6

Shaping Studies with the Sharp-Boundary Model

The purpose of this study is to determine the effects of geometry on MHD mode stability and rotational stabilizability in the presence of resistive resonant plasma surfaces and a resistive wall. The bounds for rotational stabilization serve as indicators for the roughly equivalent bounds of feedback control with imaginary normal-field gain (exactly equivalent in a cylinder [48]).

As shown analytically the a cylindrical reduced-MHD model in Chapter 3, the least stable mode in a system with both plasma resistivity and wall resistivity goes unstable at a resistive-plasma resistive-wall (rp-rw) β-limit. We demonstrate in this work how this least stable limit, denoted β_{rp-rw}, can be increased by bulk plasma rotation (comparable with the tearing-time or the wall-time) up to the first ideal limit; either the resistive-plasma ideal-wall (rp-iw) limit β_{rp-iw} or the ideal-plasma resistive-wall (ip-rw) limit β_{ip-rw}. An ideal-plasma ideal-wall (ip-iw) limit β_{ip-iw} sets the upper bound for the other limits. The space of rotational stabilizability is thus evaluated based upon the order of the four β-limits (β_{rp-rw}, β_{rp-iw}, β_{ip-rw}, β_{ip-iw}) over a broad range of plasma parameters. The 4-β formalism provides information regarding the nature of the rotationally stabilized MHD mode, which can be dominated by either tearing mode (TM) or resistive wall mode (RWM) physics.

Only one resonant surface ($m = 2$) is included in present calculations, with a corresponding tearing time τ_t that leads to a resistive plasma β-limit with finite τ_t and an ideal plasma β-limit

when $\tau_t \rightarrow \infty$. Thus we do not address the additional β-limits possible in the two-mode model presented in Section 4.4, where the timescales of two resonant surfaces could be defined separately. We begin in Section 6.1 by exploring the typical solution space of the model geometry in comparison with two special cases defined by Freidberg and Grossmann [2]: (i) An upper bound equilibrium β-limit describes the case where an x-point approaches the plasma surface on the inboard side and (ii) a typical lower value of β_{crit} describes the transition from a diamagnetic to a paramagnetic plasma equilibrium, with the toroidal field becoming larger in the plasma than in the vacuum in order to balance the strong poloidal field. Next, Section 6.2 discusses a subtle difference in the β-limit calculations of resonant versus non-resonant models. As an initial proof of principle, Section 6.3 illustrates the concept of β ordering transitions with a circular cross-section. Familiar parameters such as the wall location and edge safety factor are used to demonstrate the utility of the 4-β framework in exploring intrinsic stability and rotational stabilizability. An intuitive picture of curvature effects is developed in Section 6.4, which demonstrates how the mode structure changes as the cross-section switches from circular to shaped. In particular, varying elongation and triangularity is found to modify the β-limit ordering and lead to local optima in the space of rotational stabilizability, which is severely reduced at high shaping. Up-down asymmetry is found to reduce the two middle limits uniformly, with no dramatic impact on the rotationally stabilizable domain. Finally Section 6.5 explores transitions in the β ordering across a broad space of plasma shapes. We conclude with implications for the interpretation of observed MHD phenomena, and discussion of a new approach for optimizing the design of tokamak devices based on the space of rotational stabilizability.

6.1 Evaluating the Scope of the Sharp-Boundary Model

Although this is only a qualitative study of stability limits in tokamak geometry, it is important to first evaluate the extent to which neglecting $O(\epsilon^2)$ terms affects the resulting stability limits. Figure 6.1a portrays the effect of the $O(\epsilon)$ approximation on the stability limit β_{crit}, shown in the *dashed* line for $q_a = 2.1$. For a circular cross-section, present results are compared with the non-resonant no-wall circular cross-section calculation of Freidberg and Grossmann [2] (See Figure 3 in Reference [2]. Note that the original figure was scanned and fit to the solid black curves depicted in Figure 6.1a.). These two special cases, discussed in Chapter 5, were used in Reference [2] to characterize the

typical solution space without explicitly solving the marginal stability problem. While stability in Reference [2] is calculated without any scaling approximations, the present expansion in ϵ facilitates the convenient incorporation of non-ideal physics such as resistivity in resonant plasma layers and in the surrounding wall.

As defined in Section 5.2, an upper bound in β for any given ϵ, labeled $q \to \infty$, is given by an equilibrium β-limit with a poloidal field null approaching the inboard plasma boundary so that local pressure balance is governed by the jump in toroidal field. This upper bound is described mathematically by a constraint on the interior to exterior toroidal field ratio, expressed in Equation (5.54). A typical lower value of β_{crit}, labeled $\beta_p = 1$, is defined by a pressure balance governed entirely by the poloidal field. The stability limit with finite $q_a = 2.1$ (dashed green) is observed to cross the $\beta_p = 1$ curve (dash-dotted green) at $\epsilon = 0.36$, so that the plasma equilibrium becomes paramagnetic, since $B_i > 1$ implies $\beta_p < 1$. As discussed in Reference [49], the equilibrium β-limit generally remains above the stability limit ($q_a = 2.1$ curve) and can thus be ignored in β-limit studies. The Freidberg and Grossmann results (solid black lines) in Figure 6.1a, which are calculated numerically with no high aspect-ratio approximation, are found to agree at low ϵ with the present $O(\epsilon)$ approximation and share the same qualitative trend at high ϵ. Both models exhibit the linear high-β scaling $\beta \sim \epsilon$ at low ϵ and demonstrate an expected saturation of this toroidal stabilization at high ϵ. This contrasts with the low-β scaling $\beta \sim \epsilon^2$ of earlier models [95]. It can be concluded that the present model tends to slightly underestimate the β-limits as the aspect ratio decreases, while maintaining the same qualitative trends as an exact numerical solution.

In preparation for shaping studies, it is interesting to examine how the elongation, triangularity and up-down asymmetry β-limits behave in comparison with the two special cases discussed above, keeping in mind that $B_i = 1$ represents a transition to paramagnetic behavior rather than a β-limit. Figure 6.1b shows a varying elongation with a fixed inverse aspect ratio of $\epsilon = 0.3$. Fixing $\kappa = 1.86$ (shown later to be a locally optimal elongation for rotational stabilizability), Figure 6.1c presents a varying triangularity. Lastly, starting with a (up-down symmetric) triangularity of $\delta_0 = 0.29$ ($\delta_x = 0.14$), Figure 6.1d shows the change in β_{crit} introduced by up-down asymmetry. In all four figures (6.1a, 6.1b, 6.1c and 6.1d), the stability limit with finite $q_a = 2.1$ (dashed green line) is found to always lie below the equilibrium β-limit and therefore is the relevant upper bound for β.

Having examined the typical operational space of the non-resonant no-wall β-limits for the model geometric parameters, we now proceed to MHD stability studies in the presence of resonant resistive-

plasma layers and a resistive-wall.

6.2 Non-Resonant versus Resonant Ideal Limits

An important subtlety of the following analysis is the distinction between the present resonant-ideal model and past non-resonant-ideal models, also commonly referred to as *ideal* [2, 80, 81, 83, 84, 96–99]. Resonant-ideal boundary conditions - as used in the present model - enforce $\delta B_r = 0$ on a corresponding resonant surface, whereas non-resonant models neglect the effect of resonant surfaces and allow δB_r to pass smoothly through them. In the present model where the rational surfaces lie at the plasma boundary (just outside the equilibrium current layer), the resonant ideal limit $\tau_t \to \infty$ shields resonant perturbations from reaching the wall. The non-resonant case is recovered in this model by taking the limit $\tau_t \to 0$. Figure 6.2 plots the four resonant branches along with the non-resonant resistive-wall and non-resonant ideal-wall branches. Here the cross-section is taken to be circular, with $q_a = 2.1$, $\epsilon = 0.25$, $r_w = 1.33a$ and $\Omega = 0$. The finite dissipation timescales are set in units of Alfvén time to $\tau_w = 10^3$ and $\tau_t = 5 \times 10^4$. Throughout the thesis, plots follow the following convention: The dashed versus solid lines distinguish between a resistive and ideal plasma, while blue versus red distinguish between a resistive and ideal wall. In contrast with the reduced-MHD models (in Chapters 3 and 4) which neglect the inertial term $(\gamma\tau_A)^2$ in the dispersion relation and therefore exhibit a singularity at the ideal-plasma ideal-wall limit, the sharp-boundary model growth rate in Figure 6.2 is observed at high β to approach finite values comparable with the Alfvén time.

In the limit $\tau_t \to 0$, the model recovers the classic non-resonant ideal kink β-limit of Freidberg and Haas [80]. In the opposite limit $\tau_t \to \infty$, the resonant boundary condition becomes similar to the ideal boundary conditions of DCON [100], forcing the resonant component of δB_r to vanish at its respective resonant surface. The resistive-plasma (finite τ_t) branches, while connecting to the resonant-ideal branches at high $\gamma\tau_A$, are observed to coincide with the non-resonant ($\tau_t = 0$) limits, independent of the value of τ_t. Just as the no-wall and resistive-wall stability limits coincide [5, 33–36], so do the non-resonant ($\tau_t = 0$) and resonant resistive (finite τ_t) limits. This implies that, at zero plasma rotation, the resistive-plasma values of β_{crit} in this thesis can be compared with previous results of non-resonant ideal models.

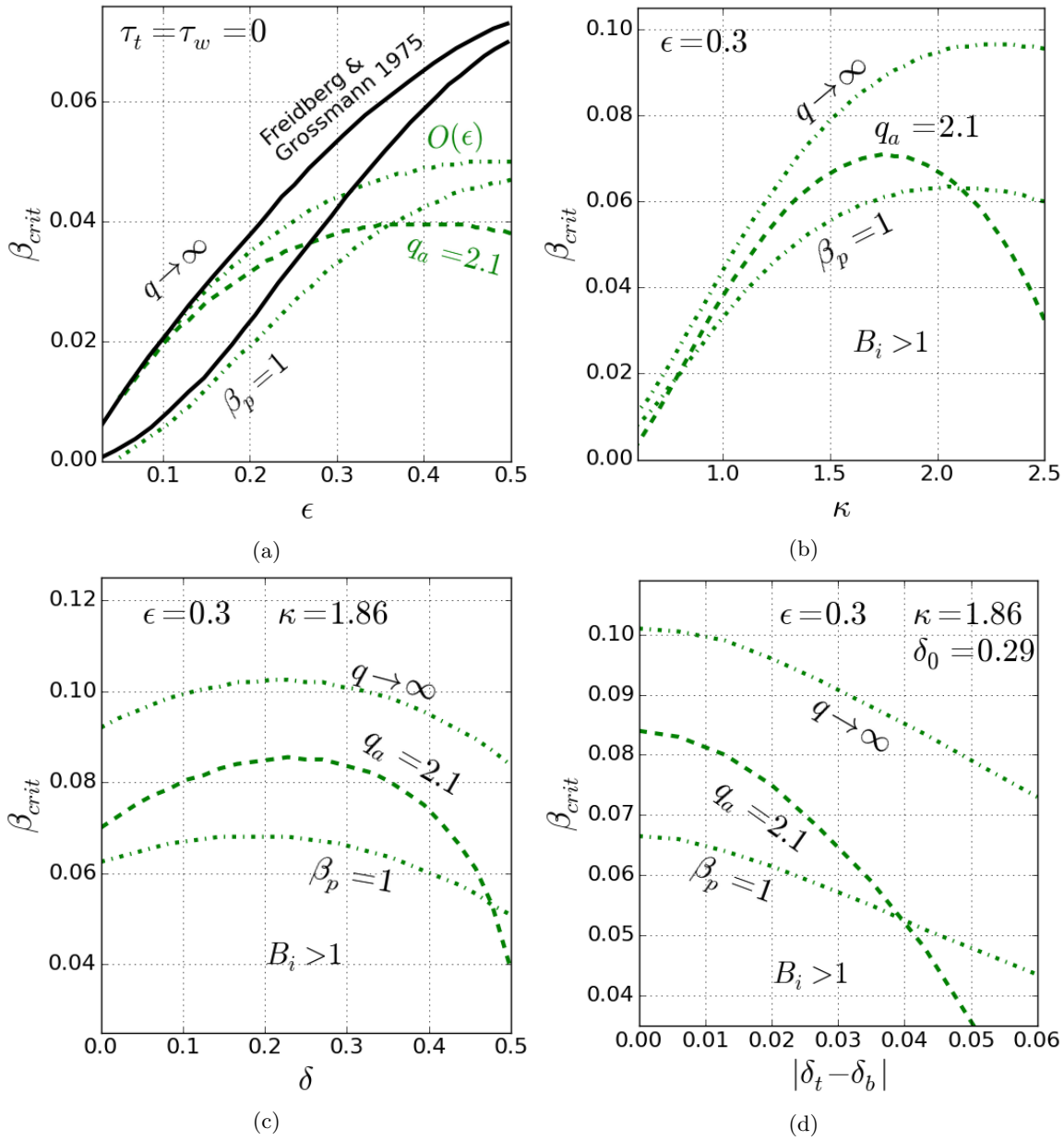

Figure 6.1: Critical β in two special cases of the sharp-boundary equilibrium, for a non-resonant no-wall calculation, plotted versus different shape parameters; (a) inverse aspect ratio ϵ, (b) elongation j, (c) triangularity δ (up-down symmetric), and (d) up-down asymmetry defined by the difference of the top triangularity and bottom triangularity $|\delta_t - \delta_b|$. For a given shape, the limit $q \to \infty$ defines an upper bound in β, representing the equilibrium β-limit. This limit is characterized by a poloidal field null which approaches the inboard plasma boundary, resulting in a local pressure balance dominated by the toroidal field. $\beta_p = 1$ is typical lower value of β_{crit} where the pressure is balanced entirely by the poloidal field. Figure (a) shows how in the present model, the $O(\epsilon)$ approximation (green dot-dashed lines) is observed to underestimate β_{crit} in these special cases in comparison with the numerical solution of Freidberg and Grossmann [2] (black solid lines), while maintaining the same qualitative trends. In all four plots, the stability limit with finite $q_a = 2.1$ (dashed green line) is found to always lie below the equilibrium β-limit and therefore is the relevant upper bound for β.

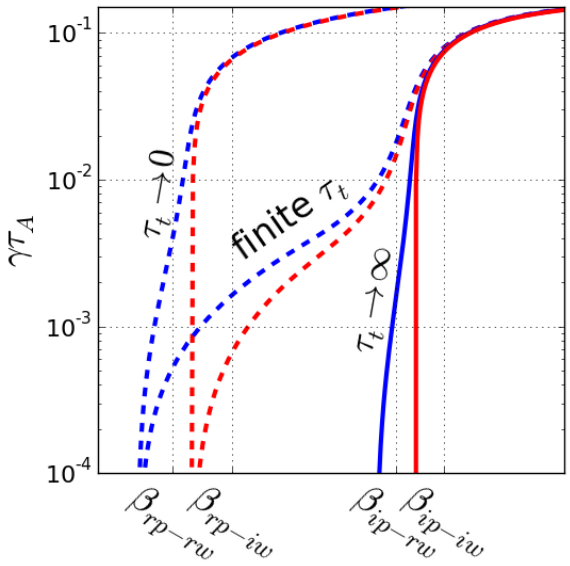

Figure 6.2: Comparison of growth-rate curves (on a logarithmic scale) for different plasma limits: Non-resonant; $\tau_t \to 0$ (dashed), resonant-resistive; finite τ_t (dashed), and resonant-ideal; $\tau_t \to \infty$ (solid). The β-limits are defined by the marginal stability points where $\gamma \to 0$. Considering first the resistive-wall (blue) curves, the resonant-ideal plasma limit β_{ip-rw} is shown to differ from the *non*-resonant ideal β-limit which coincides with the resistive-plasma limit β_{rp-rw}. This is because the β-limit is independent of the tearing timescale (which affects the growth rate but not the point of marginal stability) for any finite τ_t including $\tau_t = 0$. A mode transition occurs as $\tau_t \to \infty$. The same is true for the ideal-wall (red) curves, where the resonant ideal limit is given by β_{ip-iw}, while the *non*-resonant ideal β-limit coincides with the resistive-plasma limit β_{rp-iw}.

6.3 Effect of Wall Distance and Safety Factor on the β-Limit Ordering

As an initial qualitative comparison with the growth rate trends obtained by Betti [37], Figure 6.3 displays growth rate curves of the four branches (rp-rw, rp-iw, ip-rw, ip-iw) versus β, along with a close-up inset of the four β-limits (marginal stability points) plotted logarithmically. Here the geometry is characterized by $\epsilon = 0.25$, $r_w = 1.33$ and $q_a = 2.1$, and the dissipation times are $\tau_t = 5 \times 10^4$ and $\tau_w = 10^3$ in units of the Alfvén time. The ideal-plasma and ideal-wall limits are obtained by scaling up the dissipation times by a factor of 10^7. All present calculations include a single $m = 2$ surface by taking an edge safety factor in the range $2 < q_a < 3$, with $q_0 > 1$. The ideal "dome", reminiscent of Shafranov's reduced-MHD cylindrical analysis of non-resonant ideal kink stability [70], agrees qualitatively with the results plotted in Figures 5-6 of Reference [37]. Reference [37] obtains a relatively small separation between the resistive and ideal plasma limits, as observed in

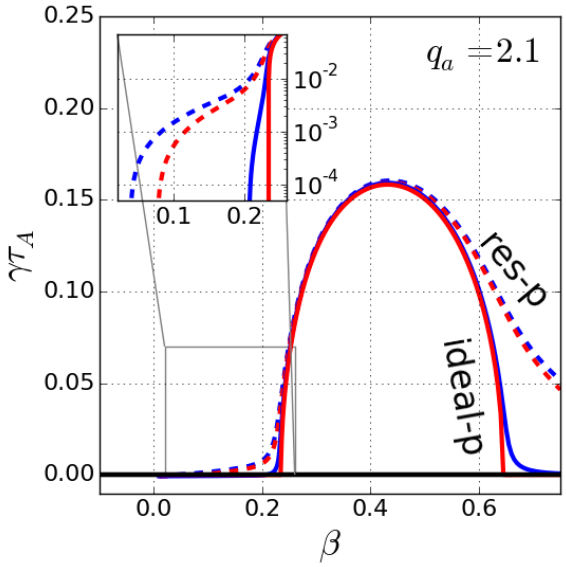

Figure 6.3: The four-β branches are plotted for circular cross-section, $\epsilon = 0.25$, $r_w = 1.33$. With $q_a = 2.1$, the observed ideal dome is dominated by $m = 2$. For the resistive branches $\tau_t = 5 \times 10^4$ and $\tau_w = 10^3$. The inset shows a close-up of the four β-limits on a logarithmic scale. (Dashed: resistive-plasma. Solid: ideal-plasma. Blue: resistive-wall. Red: ideal-wall).

the present model for calculations at high aspect-ratio. Including $O(\epsilon)$ geometric terms consistently throughout, the present model produces four distinct tails of the ideal dome, observed in the inset of Figure 6.3 comparable with the limits observed by Brennan and Finn [4]. This separation between the ideal-plasma and resistive-plasma limits is attributed to the destabilization of the resistive modes caused by toroidal mode-coupling. The additional stable domain observed in Figure 6.3 for the ip-iw curve at high β is the well-known second stability regime [101, 102]. In models with a diffuse profile and full toroidal geometry, second stability results from the high magnetic shear on the outboard side produced by the Shafranov shift [103, 104], whereas in the sharp-boundary model a similar effect is created by the wall-induced increase in magnetic pressure [37].

Recall that this study is concerned with comparing intrinsic stability of MHD modes with their rotational stabilizability; the maximum extent to which bulk plasma rotation can raise the lowest stability limit β_{rp-rw} in a system with plasma and wall resistivity. The four β-limits calculated *without* rotation will be used as indicators for the bounds of stabilizability by rotation. As a starting point, we demonstrate how as a general rule the lowest limit β_{rp-rw} can be raised by rotation up to the first ideal limit, either β_{rp-iw} or β_{ip-rw}, depending upon the wall distance from the plasma. Figure 6.4a shows the rotational stabilization of the least stable (rp-rw) mode for different values of

the wall distance r_w (normalized by the minor radius for the case of a circular cross-section). For zero rotation, the rp-rw limit is independent of wall location, being the same as the resistive-plasma no-wall limit. Rotation is observed to raise the rp-rw critical β curve and is thus stabilizing. A sharp transition is observed between the close-wall RWM-limited domain of r_w and the far-wall TM-limited domain. Consistent with existing studies [5, 33–36, 105], scanning r_w with fixed β reveals a finite window for rotational stabilization (marked by red arrows). The r_w-window is observed near the transition between the RWM-dominated and TM-dominated domain. The top curve, $\Omega\tau_w = 40$, defines the saturated bound (same as $\Omega \to \infty$) for rotational stabilization.

In order to understand the non-monotonic behavior observed in Figure 6.4a, it is illuminating to examine the higher β-limits shown in Figure 6.4b. The domain of stability for a non-rotating mode is shaded in dark-gray, while the light-gray region shows where the mode is *stabilizable* by bulk plasma rotation or feedback control with imaginary δB_r-gain. A sufficiently close wall is observed to raise β_{rp-iw} up to arbitrarily high β, which clearly does not provide a complete picture of the rotational stabilization cutoff observed in Figure 6.4a. Since β_{rp-iw} moves up as the wall moves inwards while keeping the β_{ip-rw} limit (equivalent for $\Omega = 0$ to the ideal-plasma *no*-wall limit) fixed, a switching of the two limits β_{rp-iw} and β_{ip-rw} is observed around $r_w = 1.18$. Similar plots are found in studies by Finn [52] and Betti [37]. Below the transition point, which appears as a sharp knee in the light-gray shaded region, the limit for rotational stabilization corresponds to β_{ip-rw} limit, associated with the onset of a RWM-dominated instability. Here the non-rotating mode β-limit is equivalent to the ideal-plasma no-wall limit and is thus independent of r_w. For $r_w > 1.18$, the rotationally stabilizable region gradually shrinks with the decrease of the β_{rp-iw} limit associated with the onset of a TM-dominated instability. As the wall moves outward (r_w increases), the β_{ip-rw} limit approaches the β_{rp-rw} limit (equivalent for $\Omega = 0$ to the non-resonant no-wall β-limit). These results demonstrate how a unified treatment of MHD modes over a wide range of β exhibits both RWM-dominated and TM-dominated behavior. In the interest of extending the 4-β study of Brennan and Finn [4] to shaped toroidal geometry, we begin the shaping studies in the domain that is TM-limited for a circular cross-section, proceeding with $r_w = 1.33$ for the remaining calculations.

Careful comparison of Figures 6.4a and 6.4b reveals a small exception to the general rule that rotational stabilization of the β_{rp-rw} limit is bounded by the first ideal limit. Here the maximum rotationally stabilized rp-rw limit ($\Omega\tau_w = 40$ curve) peaks slightly above the ip-rw limit, near the interchange of the ip-rw and rp-iw curves. This small stability window above the first ideal limit,

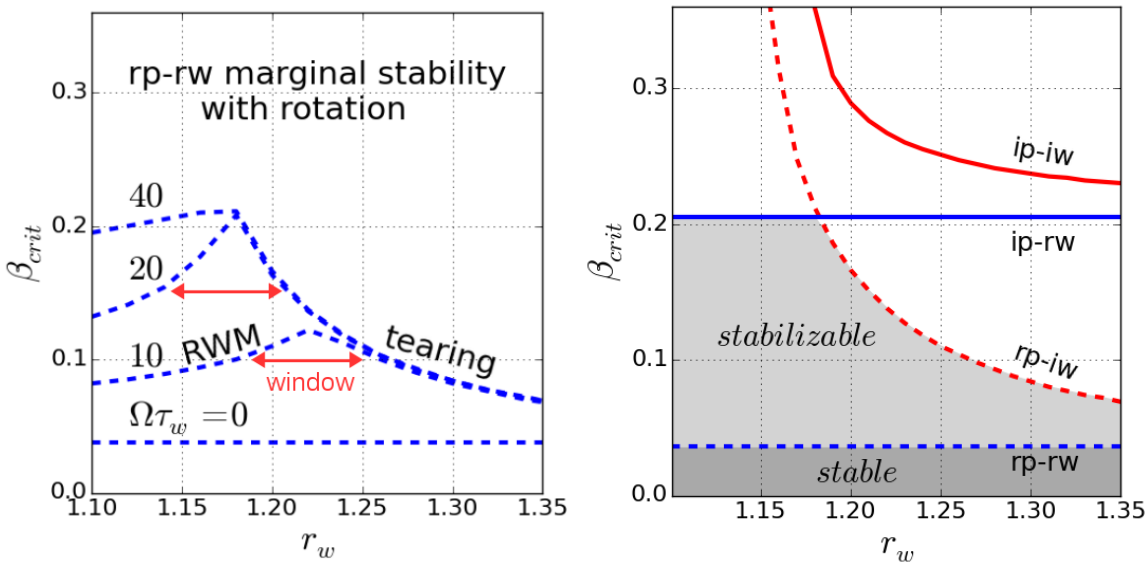

Figure 6.4: Critical β versus wall position r_w (normalized by the minor radius) for circular cross-section, $\epsilon = 0.25$ and $q_a = 2.1$. (a) The least stable (rp-rw) mode limit for four different values of plasma rotation: $\Omega\tau_w = 0$, $\Omega\tau_w = 10$, $\Omega\tau_w = 20$, $\Omega\tau_w = 40$. The mode is stable below the β_{crit} curve. For a fixed β, drawing a horizontal line crossing the non-monotonic β_{crit} curve reveals a window in r_w for rotational stabilizability (red arrows). The r_w-window opens around the transition between the RWM-limited and the tearing-limited domains. The stabilizing effect of rotation is found to saturate at $\Omega\tau_w = 40$. (b) The 4-β branches. The resistive-wall limits are equal to the no-wall limits (for $\Omega = 0$) and therefore independent of r_w. The ideal-wall branches are completely stabilized as the wall approaches the plasma ($r_w \to 1$). The rotationally stabilizable domain is marked by an interchange of the rp-iw and ip-rw branches at $r_w = 1.18$.

first observed by Finn [52], can be explained as a result of complex mode resonances as in the work of Finn and Gerwin [106]. Bondeson, Gimblett and Hastie [107] examined this exception in toroidal geometry and found an even smaller window of stability. Although not addressed in the present study, the authors suggest that a broader investigation of the parameter space should be considered before discounting this higher window of stability.

Next we consider the effect of varying the edge safety factor q_a, still keeping a circular cross-section. A strength of this model is the ability to vary q_a independently of β, unlike a diffuse equilibrium calculation. Although the q_a-domain near external kink resonance is generally avoided, it is illuminating to examine this undesirable region in the context of the 4-β framework. Recall that the ideal dome presented in Figure 6.3, for $q_a = 2.1$, is dominated by $m = 2$. Keeping $r_w = 1.33$, Figure 6.5a shows how as $q_a \to 3$, a lower ideal dome appears corresponding to the $m = 3$-dominated ideal external kink. This is clearly distinct from the remaining larger dome at higher β which, as

in Figure 6.3, represents an ideal internal kink dominated by $m = 2$. The transition is captured in the figure inset by plotting the growth rate versus q_a at fixed $\beta = 0.15$, as in Shafranov's cylindrical external kink theory [70]. Note that the relatively low-q_a point of marginal stability of the ip-iw curve (solid red in the inset of Figure 6.5a) is a toroidal effect. In agreement with the cylindrical theory, Figure 6.5b demonstrates how the ip-iw limit approaches $q_a = 3$ as ϵ decreases and the geometry becomes more like a cylinder. Observe also the analogy between the q_a-dome and the β-dome, corresponding to the current and pressure drive components of the instability.

The appearance of the lower $m = 3$-dominated dome in Figure 6.5a is associated with a sharp transition in the β limits, portrayed in Figure 6.6. In this figure, the edge safety factor is varies keeping the central axis safety factor fixed with $1 < q_0 < 2$. For $q_0 < q_a < 2$, there are no rational surfaces and so the resistive-plasma and ideal-plasma limits coincide. As q_a is increased above $q_a = 2$, the $m/n = 2/1$ rational surface is introduced, whereby the ideal plasma limits jump to a high value of β_{crit}, representing a mode dominated by an internal $m/n = 2/1$ kink. The resistive-plasma modes are continuous at $q_a = 2$, being equivalent (at $\Omega = 0$) to the non-resonant limits. As $q_a \to 3$, and the smaller $m = 3$-dominated ideal mode arises as shown in Figure 6.5a, both ideal-plasma limits are observed to drop off sharply toward their corresponding resistive-plasma limits. This effect produces a finite rotationally stabilizable window lying approximately in $2.0 < q_a < 2.27$, limited by the rp-iw (tearing) mode. This window contains much higher ideal-plasma limits, corresponding to an ideal internal kink. For the shaping calculations that follow in the next section, the safety factor is fixed inside the window at $q_a = 2.1$.

Although not addressed by Brennan and Finn [4], the interchange of the two middle β-limits due to variation of r_w or q_a can be observed even in their cylindrical reduced-MHD model. Next we consider how cross-sectional shaping in toroidal geometry can similarly influence the β-limit ordering and corresponding domain of rotational stabilizability.

6.4 Effect of Shaping on Mode Structure

Before studying how the stability limits are affected by plasma shaping, an intuitive understanding can be developed by comparing the mode structure of an unshaped versus a shaped plasma. The eigenvector associated with the dominant mode provides the harmonic distribution in terms of complex Fourier amplitudes. When possible HBT-EP and ITER numbers are used in the calculations

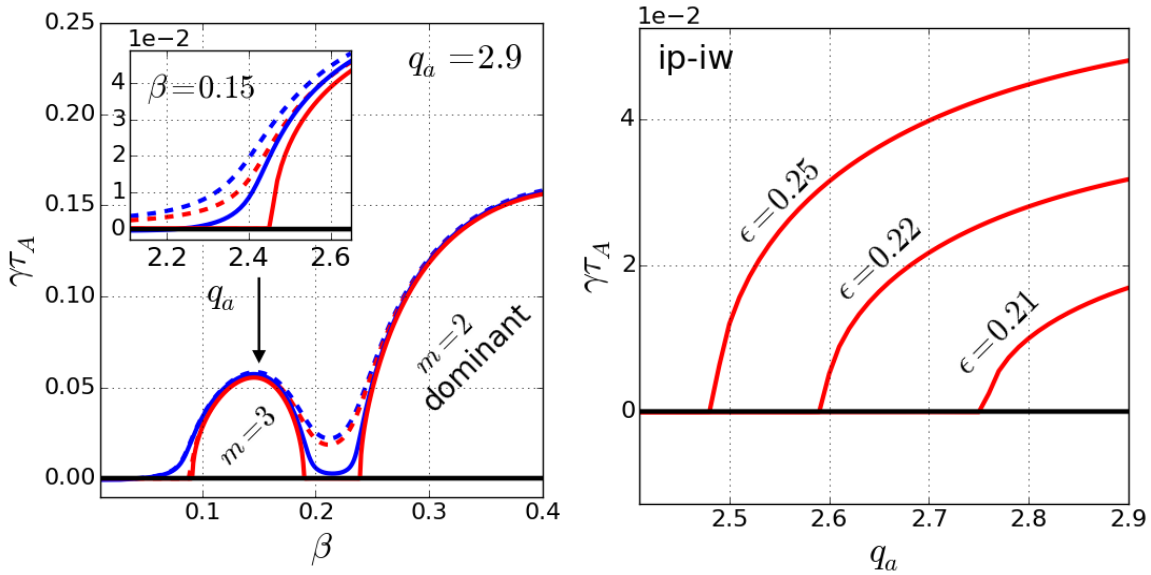

(a) (b)

Figure 6.5: (a) Rise of an $m = 3$-dominated mode near external kink resonance: The main plot shows the distinct $m = 3$-dominated and $m = 2$-dominated humps at $q_a = 2.9$, with $r_w = 1.33$. The inset shows the rise of the $m = 3$-dominated mode as $q_a \to 3$ at fixed $\beta = 0.15$. (b) Decreasing ϵ, we observe that the ip-iw limit (of the solid red curve in the inset of Fig. (a)) approaches $q_a = 3$, in agreement with cylindrical theory.

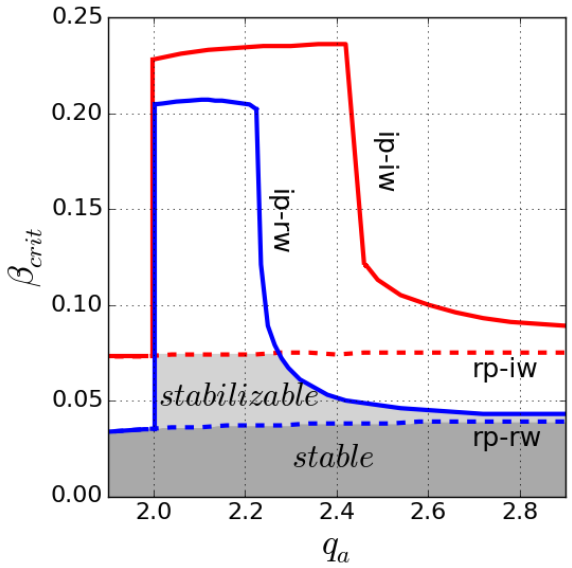

Figure 6.6: For a circular cross-section, $\epsilon = 0.25$ and $r_w = 1.33$, the critical β for the four branches is shown for varying edge safety factor q_a. The ideal-plasma limits cut of the rotationally stabilizable domain near both the $m = 2$ and $m = 3$ external kink resonances.

below. However, the point of this exercise is to compare the typical mode structure of a high aspect-ratio circular cross-section plasma with a low aspect-ratio shaped plasma, making the numerical values less important than the conceptual discussion that follows.

As discussed in a textbook by Bateman [79], the surface structure of the perturbed fields in shaped toroidal geometry can differ from the structure of the perturbed surface displacement $\boldsymbol{\xi}$. This can be seen by Fourier expanding the ideal equation $\delta \boldsymbol{B} = \boldsymbol{B} \cdot \boldsymbol{\nabla} \boldsymbol{\xi}$ relating the perturbed field and the surface displacement. In the context of the sharp-boundary model this results in a set of perturbed radial and poloidal field components described by

$$\delta B_r^{(m)} \propto r \frac{dV_m}{dr} = \sum_k \hat{G}_{mk} \xi_k \tag{6.1}$$

$$\delta B_\theta^{(m)} \propto m V_m = m \sum_k C_{mk}^{(\mathrm{vac})} r \frac{dV_k}{dr} = m \sum_k \sum_{m'} C_{mk}^{(\mathrm{vac})} \hat{G}_{km'} \xi_{m'} \tag{6.2}$$

We are primarily interested in the perturbed poloidal, typically the dominant perturbed field measured by magnetic sensors. Using typical values from HBT-EP, with a circular cross-section and a relatively high aspect ratio of $1/\epsilon = 6$, comparison of Figures 6.7a and 6.7b confirms that the sharp-boundary model is able to produce a mode structure with reasonably close agreement with experiments. Figure 6.7a shows a typical HBT-EP poloidal field structure, broken into sine and cosine components from an array of poloidal sensors [3]. The amplitude is adjusted in arbitrary units to create a clear visualization. Figure 6.7b, the sharp-boundary model output demonstrates a similar perturbed field structure, projected onto the wall surface $r = r_w$ with a cylindrical $r_w^{-|m|}$ approximation for each mode. An edge safety factor of $q_a = 2.9$ and $\beta = 0.03$ ($\beta_N = 3.0$) result in a wall-time normalized growth rate of $\gamma \tau_w = 0.29$, slightly above marginal stability. Typical HBT-EP values are used: Wall radius (normalized by the minor radius) of $r_w = 1.09$, wall dissipation time of $\tau_w = 286 \tau_A$ ($\approx 286 \mu sec$) and rotation frequency of $\Omega \tau_A = 0.048$ ($f \approx 8 kHz$). Note that the $8 kHz$ modes observed in experiments are thought to be carried by the electron fluid, while this single fluid MHD model must capture the effect by rotating the entire plasma with respect to the wall. In the absence of any known value, the tearing time is taken to be a typical $\tau_t = 1000 \tau_A$ ($\approx 1000 \mu sec$), on the same order of magnitude as the wall time. The harmonic breakdown is included to demonstrate the good agreement with the expected $m = 2$ and $m = 4$ sideband coupling expected for a toroidal plasma with circular cross-section. Due to the high aspect ratio, the perturbed field

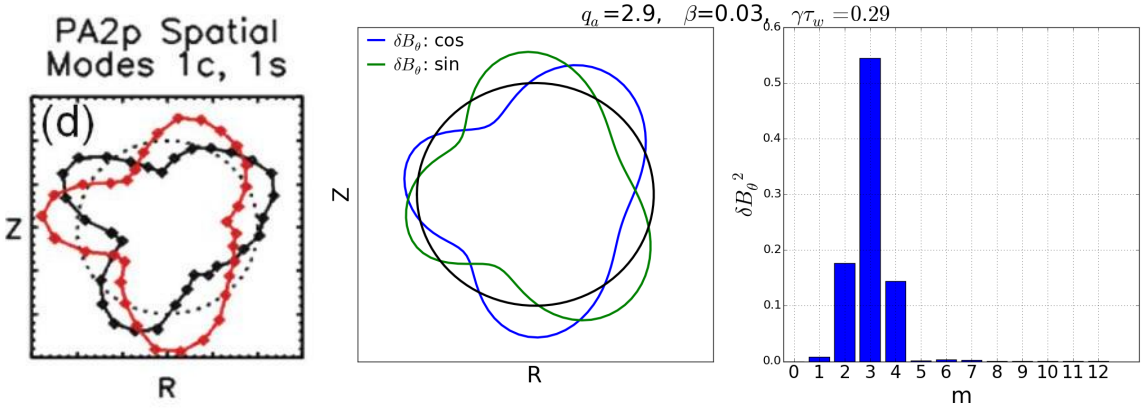

(a) (b)

Figure 6.7: (a) HBT-EP experimental output [3] showing a typical poloidal field structure from a poloidal sensor array, broken into sine and cosine components. (b) Sharp-boundary model calculation showing good agreement with the HBT-EP perturbed field structure, just above marginal stability.

is evenly distributed around the cross-section, whereas low aspect ratio devices tend to concentrate the instabilities on the low-field outboard side of the torus.

To help visualize the perturbed field over the entire plasma surface, Figure 6.8 shows the toroidal distribution unfolded onto a flat contour plot. Here θ and ϕ are the poloidal angle-like coordinate and toroidal angle, respectively. For a circular cross-section the poloidal coordinate equals the poloidal angle. The distribution is nearly uniform over the surface, as expected of a circular cross-section at high aspect-ratio. For any fixed θ, drawing a horizontal line crosses each stripe only once, describing an $n = 1$ toroidal Fourier number. For any fixed ϕ, drawing a vertical line crosses each stripe three times, describing an $m = 3$ poloidal Fourier number.

In contrast with HBT-EP, the ITER design includes a strongly shaped cross-section with typical elongation $\kappa = 1.7$, triangularity $\delta = 0.5$ and up-down symmetry, along with an inverse aspect ratio of $\epsilon = 0.3$ and normalized wall position of $r_w = 1.08$ [99]. While potentially stabilizing, as will be discussed in the following section, the strong shaping can create localized regions of bad curvature (where the pressure gradient is aligned with the field curvature) near the top and bottom of the plasma cross-section. Figure 6.9 shows the perturbed poloidal field around the cross-section and the associated harmonic breakdown. This calculation uses typical a dissipation time of $\tau_t = \tau_w = 10^4 \tau_A$, zero rotation, $q_a = 2.9$ and $\beta = 0.13$, resulting in a growth rate of $\gamma\tau_w = 0.22$ slightly above marginal stability. Note that in the shaped case the poloidal coordinate differs somewhat from the actual poloidal angle, with visible compression and expansion as the cross-sectional curvature changes.

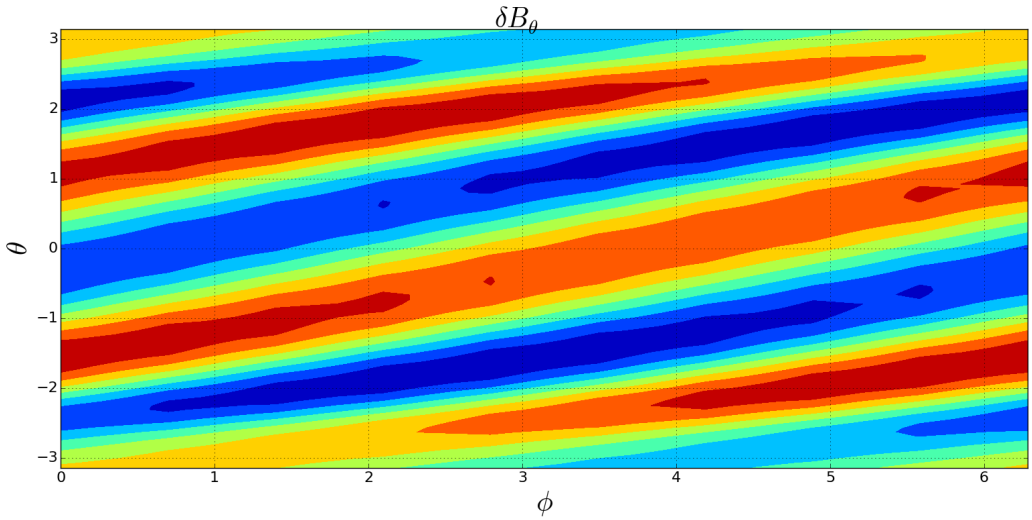

Figure 6.8: Sharp-boundary model contour plot of the mode in Figure 6.7b, demonstrating a typical HBT-EP perturbed poloidal field structure displayed over the entire surface at $r = r_w$, defined by the poloidal coordinate θ (equal to the poloidal angle in this circular case) and the toroidal angle ϕ.

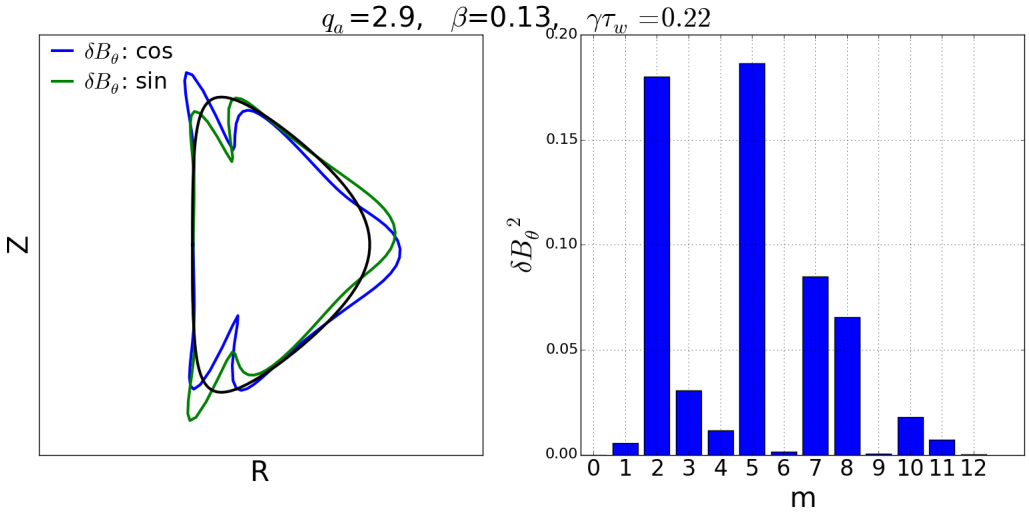

Figure 6.9: Sharp-boundary model prediction of a perturbed poloidal field structure for a strongly shaped up-down symmetric (ITER-like) shape. The instability is strongly localized around the regions of bad curvature (where the pressure gradient is aligned with the field curvature), including the top, bottom and outboard (low-field) side.

As anticipated, the instability is concentrated in the local regions of bad curvature on the top and bottom. In addition, the lower aspect-ratio ($1/\epsilon = 3.3$) creates a larger curvature on the outboard (right hand) side of the torus, making the mode balloon outwards. The resulting harmonic distribution is much broader than in the circular-cross section case, and more difficult to predict by intuition. In order to visualize the instability of the entire plasma surface, Figure 6.10 shows the

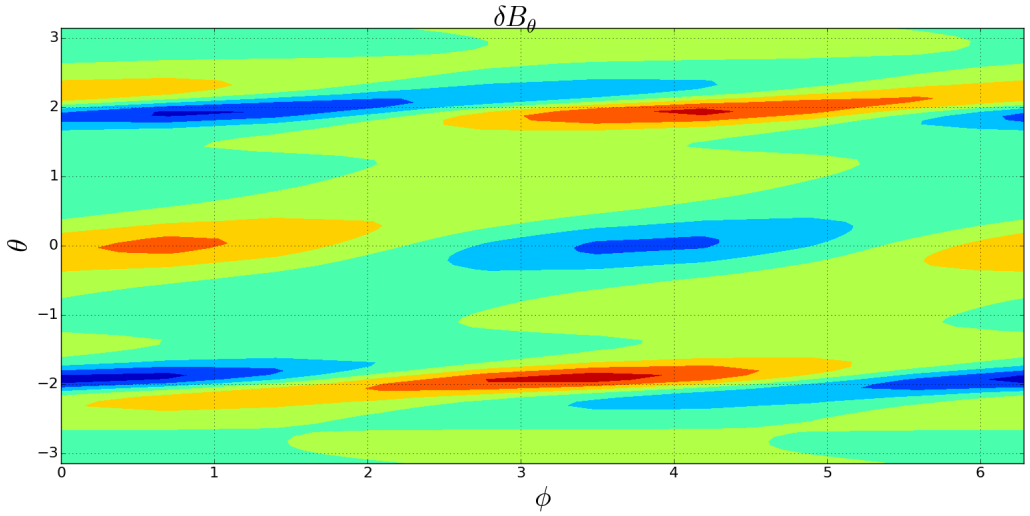

Figure 6.10: Sharp-boundary model contour plot of a perturbed poloidal field predicted for a strongly shaped up-down symmetric (ITER-like) shape, to help visualize the mode in Figure 6.9 over the entire shaped toroidal surface at $r = r_w$. The instability is strongly localized around the regions of bad curvature including the top, bottom and outboard (low-field) side. The surface is defined by a poloidal coordinate θ (which differs slightly from the poloidal angle in this shaped parametrization) and the toroidal angle ϕ.

resulting contour plot, highlighting the localized unstable bands around specific poloidal angles.

These mode structure plots illuminate a tradeoff in plasma shaping. While shaping can improve the total surface-averaged curvature, it can also introduce local regions to bad curvature. It is therefore heuristically expected that shaping will improve stability, but only up to a point. With this intuition in mind, we now explore how shaping affects stability.

6.5 Effect of Shaping on the Rotationally Stabilizable Domain

Cross-sectional shaping is shown in this section to also influence the β-limit ordering. Starting with a realistic inverse aspect ratio of $\epsilon = 0.3$, a wall located at $r_w = 1.33$ and a safety factor of $q_a = 2.1$, Figure 6.11a shows how the critical β curves of the four branches vary with elongation κ. As before, the central axis safety factor is set to $1 < q_0 < 2$, so that with $2 < q_a < 3$ there is only an $m/n = 2/1$ surface included in the calculations. For a circular cross-section and $q_a = 2.1$, this yields an ideal mode dominated by $m = 2$ as discussed in the previous subsection. Figure 6.11a shows how, for these equilibrium parameters, the ideal plasma modes are predominantly *destabilized* by elongation beyond

$\kappa = 1.1$ for β_{ip-rw} and beyond $\kappa = 1.3$ for β_{ip-iw}. This behavior is consistent with shaping models of the ideal internal kink [62, 63]. The resistive plasma modes, on the other hand, are stabilized up to an elongation in the neighborhood of $\kappa = 1.9$, in qualitative agreement with the non-resonant result of Freidberg and Haas [54]. The domain of rotational stabilizability is observed to peak at $\kappa = 1.86$, the interchange point of the rp-iw and ip-rw curves, beyond which increasing elongation severely reduces the ip-rw limit and the resulting extent of rotational stabilizability. This peak value is a local optimum which depends upon the other plasma shaping parameters. We emphasize that, rather than an exhaustive study of the parameters space, the present study aims to demonstrate the utility of the 4-β approach and to develop a qualitative understanding of how plasma shaping affects the domains of MHD stability and rotational stabilizability. It is interesting to note that this peak of rotational stabilizability appears to closely coincide here with the peak in intrinsic (non-rotating) stability, which exhibits good agreement with the range of optimal elongation calculated for DIII-D by Kessel et. al. [97] as well as typical values in the ITER design [87]. In general, however, the two peaks need not coincide.

In order to highlight how vertical elongation can open a window of rotational stabilizability, analogous to the r_w-window observed in Figure 6.4a, Figure 6.11b plots the growth rates (normalized by the wall-time) of the least stable (rp-rw) mode versus κ, with different rotation values $\Omega\tau_w = 0$, $\Omega\tau_w = 2$, and $\Omega\tau_w = 6$. The fixed $\beta = 0.11$ corresponds to a horizontal cut across the plot in Figure 6.11a, above the peak value of intrinsic stability $\beta_{crit} = 0.08$, but below the peak value of rotational stabilizability $\beta_{crit} = 0.13$. Starting from $\Omega\tau_w = 0$, where the mode is unstable for any elongation, an increase of rotation to $\Omega\tau_w = 2$ is observed to saturate the extent of rotational stabilization for any elongation above $\kappa > 2.0$. For these highly elongated shapes, the ip-rw limit (associated with the linear onset of a RWM) is observed to block the mode from being completely stabilized. A slight exception is found near the transition point from the TM-dominated (left) branch to the RWM-dominated (right) branch of the $\Omega\tau_w = 2$ curve. Similar to the case discussed in the previous section for β_{crit} versus r_w, this is another example of slight stabilization above the ip-rw (RWM) limit as discovered by Finn [52]. Note that this shaped case in Figure 6.11b hits the transition point at $\Omega\tau_w = 2$ rather than $\Omega\tau_w = 40$ as observed in Figure 6.4a for a circular cross-section. At lower elongation values, increasing rotation continues to stabilize the mode up to the rp-iw (TM) limit, saturating slightly above $\Omega\tau_w = 6$. The $\Omega\tau_w = 6$ also exhibits a slight crossing of the ip-rw limit near the transition point between the ip-rw and rp-iw curves, in this case for stable values of γ.

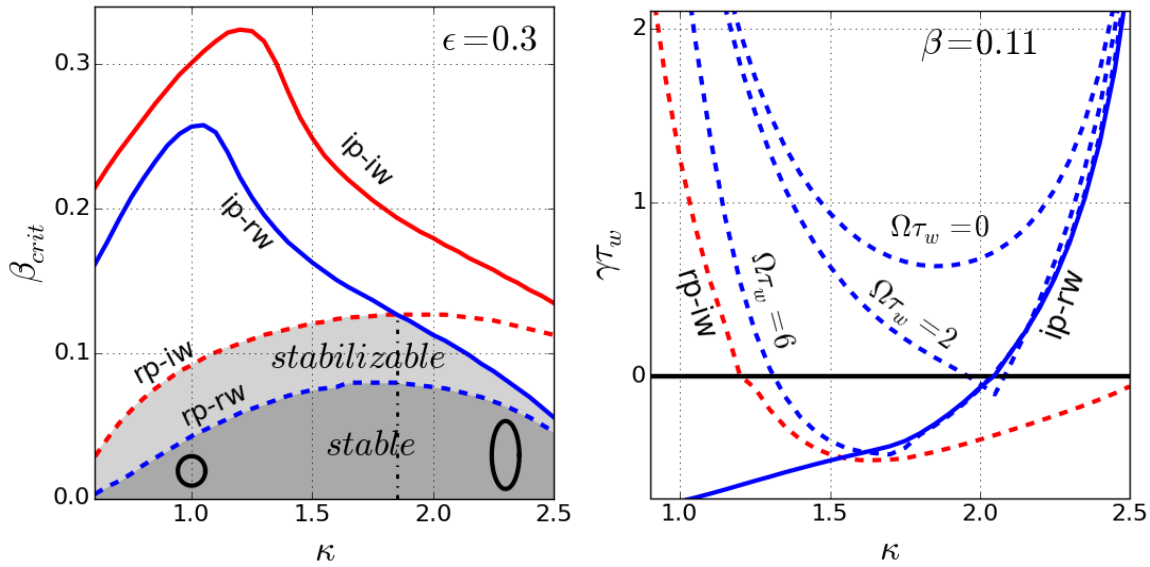

(a) (b)

Figure 6.11: (a) Critical β values of the four branches versus elongation κ, with $\epsilon = 0.3$, $r_w = 1.33$ and $q_a = 2.1$. The two middle branches are observed to cross at $\kappa = 1.86$, where $\beta_{crit} = 0.13$, representing a transition in the rotationally stabilizable domain from tearing limited (rp-iw) to resistive-wall limited (ip-rw) behavior. (b) Growth rates of the least stable (rp-rw) mode versus elongation, for fixed $\beta = 0.11$ and three different values of rotation $\Omega\tau_w = 0$, $\Omega\tau_w = 2$, $\Omega\tau_w = 6$ (all dashed-blue). The rp-iw curve (dashed-red) is observed to be marginally stable ($\gamma = 0$) at $\kappa = 1.2$, below which the rp-rw mode cannot be stabilized by rotation. Similarly the ip-rw curve (solid-blue) crosses $\gamma = 0$ near $\kappa = 2.0$, above which the rp-rw mode cannot be stabilized by rotation (with a slight exception at the mode transition near $\kappa = 2.0$)

Increasing the fixed β would shift all of the curves upwards, until the marginal stability ($\gamma\tau_w = 0$) line coincides with the bottom of the high rotation curve $\Omega\tau_w = 6$, which occurs at $\beta = 0.13$. The point of maximal rotational stabilization is observed to coincide with the crossing of the rp-iw and ip-rw curves. This result suggests that, similar to the window of r_w for rotational stabilizability (Fig. 6.4a), the optimal window of elongation κ is found around the transition from the TM-dominated to the RWM-dominated domain.

To clarify the different mode behavior before and after the mode crossing, Figures 6.12a and 6.12b show the rotation-induced shift of the rp-rw growth rate curves below and above $\kappa = 1.86$. In the first case, $\kappa = 1.5$, rotational stabilization of the least stable mode (associated with the rp-rw limit) is bounded by the rp-iw limit, saturating at a rotation of $\Omega\tau_w = 5.0$. In the second case, $\kappa = 2.1$, the rotational stabilization effect saturates at a lower value of $\Omega\tau_w = 1.6$, cut off by the ip-rw limit. Looking back at Figure 6.11a, it is clear that the rotational stabilization continues to

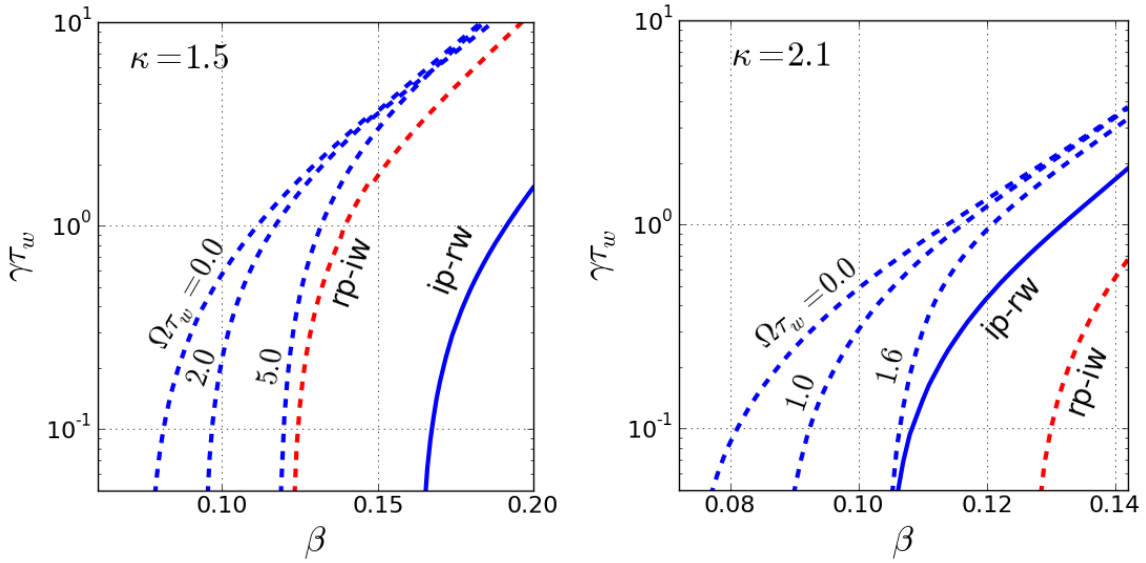

Figure 6.12: Rotational stabilization of the rp-rw mode up to the first ideal limit, for $q_a = 2.1$ and $\epsilon = 0.3$, according to Figure 6.11a. (a) At $\kappa = 1.5$ the first ideal limit is the rp-iw limit. (b) At $\kappa = 2.1$, the first ideal limit is the ip-rw limit.

become less effective as the elongation further increases. Around $\kappa = 2.5$, the stabilizable region nearly disappears, so that rotation (or feedback control with imaginary δB_r gain) becomes ineffective at stabilizing the mode. This suggests that with too much elongation, mode coupling can cause the ideal internal kink to behave similarly the external-kink dominated region observed in Figure 6.5a as $q_a \to 3_-$.

Next, Figure 6.13a introduces triangularity δ, fixing elongation at the peak rotationally stabilizable value of $\kappa = 1.86$. Starting at the mode interchange where the two middle β limits coincide, increasing triangularity is observed to create a slight separation and then another interchange at $\delta = 0.29$ ($\delta_x = 0.14$). Beyond this critical triangularity, the ip-rw limit decreases rapidly and diminishes the rotationally stabilizable region, similar to the high elongation effect observed in Figure 6.11a. While this value provides only a local optimum around a fixed aspect ratio and elongation, as well as wall position and safety factor, it provides a proof of concept for parameter optimization based on rotational stabilizability.

As with elongation, the peak rotational stabilizability is found nearby the peak of intrinsic (non-rotating) stability. Further investigation is required to determine if this is a trend or mere coincidence. In contrast with the relatively high range of optimal triangularity $0.5 < \delta < 0.8$

calculated for ideal external kink modes in DIII-D by Kessel et. al. [97], present results suggest that such high triangularity may be detrimental in a real system with plasma dissipation. The triangularity range in the ITER design [87], $0.3 < \delta < 0.5$, is in the slightly more conservative range but still possibly beyond optimal stabilizability by rotation or the equivalent feedback control with imaginary δB_r-gain.

Now starting with the (locally) optimal shaping parameters $\kappa = 1.86$ and $\delta = 0.29$, Figure 6.13b plots the four β_{crit} curves with increasing up-down asymmetry, measured by the difference between the top and bottom triangularity (see diagram in Figure 5.1a). While up-down asymmetry is found to destabilize the least stable (rp-rw) mode, it is not seen to substantially modify the relative height of the first ideal β-limit. No β-limit reordering is observed. Thus, although destabilizing, up-down asymmetry is not predicted to severely reduce the effectiveness of rotational stabilization or the equivalent feedback control with imaginary δB_r-gain. One more observation is the increase in the ip-iw limit. This opposite behavior of the rp-rw and ip-iw limits should serve as a caveat for ideal-plasma ideal-wall models, which may falsely conclude that up-down asymmetry is generally stabilizing.

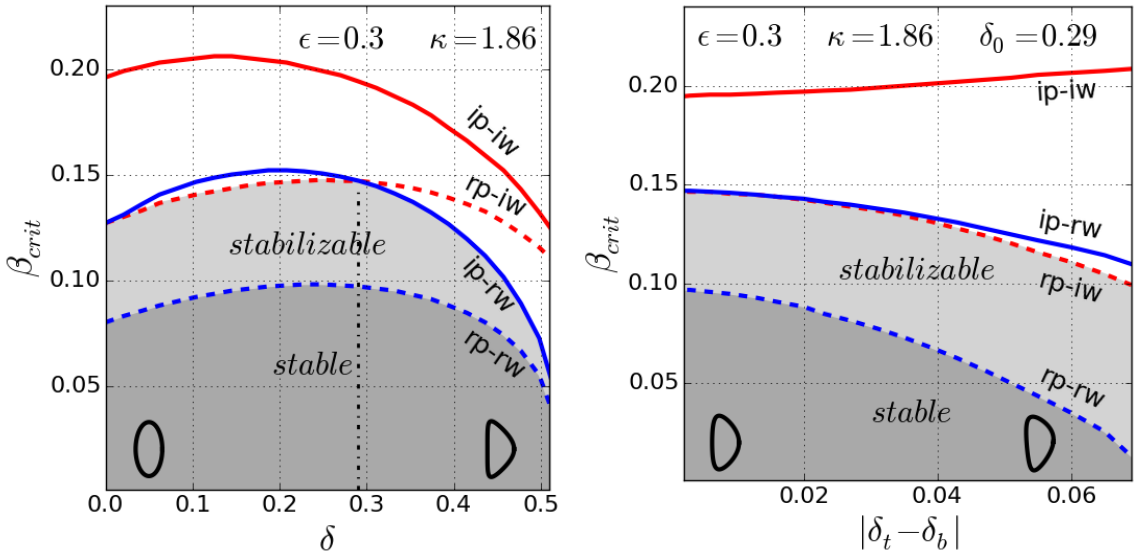

(a) (b)

Figure 6.13: The four marginal stability branches varying (a) triangularity, with fixed $\epsilon = 0.3$ and $\kappa = 1.86$ (the optimal elongation at $\delta = 0$ in Fig. 6.11a, where $\beta_{ip-rw} = \beta_{rp-iw}$). This calculation is up-down symmetric so that $\delta_t = \delta_b = \delta$. Another mode interchange is observed at $\delta = 0.29$ ($\delta_x = 0.14$). (b) Up-down asymmetry is varied, starting from the locally optimal up-down symmetric triangularity $\delta_0 = 0.29$. The stabilizable domain decreases monotonically with no observed mode transition.

Chapter 7

Conclusion

7.1 Thesis Summary

Mode-Coupling and the 4-β Formalism

This study has explored shaping effects on the magnetohydrodynamic (MHD) stability of a resistive tokamak plasma surrounded by a resistive wall. Considering a plasma equilibrium that is stable at low β - the volume-averaged ratio of the fluid to magnetic pressure - we examined the linear onset of unstable MHD behavior at a finite β-*limit*. The particular focus of this study was the β-domain in which the plasma is *stabilizable* by bulk plasma rotation. We found that, as a general rule, plasma rotation comparable with the tearing or wall time can stabilize the mode up to the lower β-limit among two ideal limits; either the resistive-plasma ideal-wall limit β_{rp-iw}, associated with the onset of a tearing dominated instability, or the ideal-plasma resistive-wall limit β_{ip-rw}, associated with the onset of a resistive-wall dominated instability.

This investigation was motivated by the '4-β' framework of Brennan and Finn [4], who used the four limits

$$\beta_{rp-rw}, \qquad \beta_{rp-iw}, \qquad \beta_{ip-rw}, \qquad \beta_{ip-iw}, \tag{7.1}$$

to explore general MHD stabilizability by rotation and/or feedback control. While the β_{rp-rw} limit is always associated with the least stable mode and the β_{ip-iw} limit sets an upper bound for stability, there is no constraint on the order of the two middle limits β_{rp-iw} and β_{ip-rw}. The study in Reference [4] explored a limited set of parameters in which the 4-β limits followed the

order $\beta_{rp-rw} < \beta_{rp-iw} < \beta_{ip-rw} < \beta_{ip-iw}$. Revisiting the Brennan-Finn reduced-MHD model, we demonstrated that even in cylindrical geometry the order of these two middle limits, β_{rp-iw} and β_{ip-rw}, can vary with plasma parameters such as the wall radius and edge safety factor, thereby causing a mode transition in the bounds for rotational stabilizability. This finding motivated the further investigation of the 4-β limit ordering in shaped toroidal geometry.

We note that the utility of the presented results applies even in systems with very little plasma rotation, where the rotationally stabilizable β-domain can be accessed by an equivalent feedback control with imaginary normal-field gain. This type of feedback can be designed to emulate wall rotation with respect to the plasma, which in the cylindrical single-mode limit is exactly equivalent to bulk plasma rotation with respect to the wall [48].

To better understand the effects of the geometric mode-coupling in a shaped toroidal model, we developed a reduced-MHD model with two poloidal harmonics coupled by first-order toroidal curvature, presented in Chapter 4. This model was used to analytically demonstrate how geometric mode-coupling can introduce a lower resistive-plasma resistive-wall β-limit in a system that would be more stable in a cylinder. This effect carries over to the sharp-boundary model, which includes a broad spectrum of coupled poloidal harmonics.

Shaped Sharp-Boundary Model with Tearing Surfaces and a Resistive Wall

A new sharp-boundary model was developed to study the impact of plasma shaping on the stability and rotational stabilizability of MHD modes in the presence of plasma and wall resistivity. With this new tool, the non-ideal MHD physics established using the reduced-MHD models was extended to shaped toroidal tokamak geometry, parametrized by the inverse aspect-ratio and cross-sectional shaping parameters; elongation, triangularity and up-down asymmetry.

The model combines aspects of previous sharp-boundary models by Fitzpatrick [69] and Freidberg and Grossmann [2]. Fitzpatrick's error-field response model contributed the tearing layer formulation as well as the base equilibrium geometry. Following Freidberg and Grossmann, the geometry was extended to a torus, including toroidal curvature contributions up to first order in the inverse aspect-ratio ϵ. In addition, the geometry was generalized to encompass up-down asymmetric plasmas which appear in systems with a single-null divertor. Lastly, a resistive wall was added around the plasma to explore tearing-wall coupling and to apply the 4-β approach in shaped toroidal geometry.

The model was designed to focus on key aspects of non-ideal MHD physics, in order to study

qualitative trends and develop physical insight into the effect of plasma shaping on MHD stability in the presence of tearing layers and a resistive wall. It was implemented in Python on a personal computer. Making use of the versatility and speed of the sharp-boundary model, stability limits were explored over a wide range of plasma and wall parameters, with particular emphasis on shaping.

Geometric Effects on MHD Stability and Rotational Stabilizability

The development of the sharp-boundary model has lead to new insights into the nature of MHD stability limits in a tokamak. An observation that underlies MHD stability analysis in general is the distinction between resonant and *non*-resonant limits. The present work pointed to an inconsistency in the understanding of ideal-MHD stability limits, shown to be qualitatively different depending upon whether or not resonant surfaces are present in the plasma. The ideal plasma β-limit in the absence of resonant surfaces (the non-resonant case) was shown to coincide with the β-limit of a resistive plasma with resonant surfaces. In contrast, the ideal-plasma β-limit in the presence of resonant surfaces was shown to be higher due to the shielding of resonant perturbations. Shaping effects on *resonant resistive* plasma limits in the present model qualitatively were shown to agree with previous *non-resonant ideal* plasma shaping studies [54, 54].

The analysis in this study is based on the 4-β formalism of Brennan and Finn [4], dividing the plasma response to rotation or feedback according to the four β-limits; resistive-plasma resistive-wall (β_{rp-rw}), resistive-plasma ideal-wall (β_{rp-iw}), ideal-plasma resistive-wall (β_{ip-rw}), ideal-plasma ideal-wall (β_{ip-iw}), calculated *without* rotation or feedback. In the absence of rotation, increasing β causes the least stable mode to go unstable at the β_{rp-rw} limit. To achieve higher β, the mode is shown to be stabilized by rotation (comparable with the wall-time or the tearing-time) up to the first ideal limit; either β_{rp-iw} associated with the linear onset of a TM-dominated instability, or β_{ip-rw} associated with the linear onset of a RWM-dominated instability. A slight deviation above the ip-rw limit was observed when the TM-RWM transition occurs near marginal stability. Although in agreement with previous studies [52, 107] the exception to the general rule was found to be very small, further investigation of the parameter space is needed to understand the scope of this phenomenon.

Initial studies with a circular cross-section torus have illuminated important points. The growth rate plots for β and for the safety factor q_a were shown to produce analogous ideal 'domes' (similar to those in cylindrical ideal kink theory) with extended tails for resistive-plasma or resistive-wall

branches, in agreement with a similar study by Betti [37]. Furthermore, varying q_a was shown to introduce multiple ideal-plasma domes dominated by different poloidal harmonics (here $m = 2$ and $m = 3$). Plotting β_{crit} versus q_a revealed how approaching the external kink resonance $q_a \to 3$ destabilizes the ip-rw branch (dominated by $m = 3$), resulting in a sharp contraction in the domain of rotational stabilizability. Plotting β_{crit} versus wall radius r_w with different rotation values also revealed an important feature of rotational stabilization: The r_w-window for rotational stabilization, observed in several early RWM studies [5, 33–36, 105], was shown to reside around the transition between the RWM-dominated and TM-dominated regions.

A central result of this dissertation was obtained by examining the 4-β limits while varying the plasma shape parameters. Extending existing predictions that the plasma-wall distance can interchange the order of the rp-iw and ip-rw β-limits [37, 52], present results showed that the safety factor, elongation and triangularity can all introduce similar mode transitions which affect the rotationally stabilizable domain. In the case of the elongation and triangularity, the window of highest rotational stabilizability was found to reside around the transition point $\beta_{ip-rw} = \beta_{rp-iw}$, defining a local optimum in the parameter space. Beyond this point, excessive elongation or triangularity was found to severely reduce the possible rotational stabilizability by driving the ip-rw limit below the rp-iw limit. This result suggests a new approach to shape optimization, based on the rp-rw β-domain accessible with stabilization by plasma rotation, or by an equivalent feedback control with imaginary normal-field gain. This approach could be used to optimize the shape with respect to other toroidal n-harmonics as well, in particular $n = 0$ which is a concern for vertical stability.

The goal of this dissertation is twofold. First, new insights stemming from the 4-β analysis of rotational stabilizability in shaped toroidal geometry are intended to improve the interpretation of experimentally observed MHD modes involving aspects of both TM and RWM behavior. Secondly these qualitative trends, the discovery of which was facilitated by the speed and versatility of the sharp-boundary model, are intended to lay the groundwork for a broader investigation of the multi-dimensional space of plasma and wall parameters. By locating sub-domains of interest, the model may be used to guide the investigation of larger codes in determining optimal design parameters for future tokamak devices.

7.2 Future Work

The following projects, while beyond the scope of this dissertation, are natural extensions of the sharp-boundary model and associated analysis techniques developed in this work. The first two topics, alternate tearing layer regimes and differential rotation of multiple tearing surfaces, require minimal modification to the model with plenty of new physics to be explored. Next, we provide background and describe the incorporation of ferritic wall effects, of particular interest to recent HBT-EP experiments. The ferritic layer can be incorporated into the single-mode reduced-MHD model as well as into the multi-mode sharp-boundary model, a project which is already in progress. Feedback-control and error-field response have also undergone a preliminary formulation but still require careful benchmarking. The last topic, converting this eigenvalue calculation to a time evolution code, may also be a direct extension of this model but is not yet underway.

Alternate Tearing Layer Regimes

The present calculations assume a constant-ψ visco-resistive tearing regime [50, 51]. As meticulously detailed by Cole and Fitzpatrick [77], different tearing regimes produce a different layer response to both intrinsic perturbations and external error-fields. A different tearing layer is expected to exhibit a different interaction with the resistive wall. By modifying the tearing layer boundary condition, defined in the sharp-boundary Equation (5.61), it would be straightforward to investigate how these different tearing regimes influence the stability and rotational stabilizability of the resistive-plasma resistive-wall mode. Since the growth rate is solved numerically, this modification requires no additional alterations to the model and is ready for implementation. The various versions of the reduced-MHD model, described in Chapters 3 and 4, may also be used to develop an intuition for the effect of alternate layers, with the benefit of being completely analytic.

Differential Rotation

In addition to bulk plasma rotation, tokamak plasmas are affected by rotation *shear*. This can introduce differential rotation between rational surfaces which modifies their mutual interaction and the resulting tearing modes [51]. While presented calculations focused on a single $m/n = 2/1$ rational surface due to an edge safety factor in the range $2 < nq_a < 3$ (with a central axis saftefy factor $1 < nq_0 < 2$ and fixed toroidal mode number $n = 1$), the tearing layer response in Equation (5.108)

includes the possibility of multiple rational surfaces. To account for differential rotation, a separate rotation and corresponding Doppler shift can be assigned to each rational surface. This will affect the complex mode interaction by changing both the mutual inductance between the layers as well as their coupling with the resistive wall.

Ferritic Effects

The best existing candidates for blanket materials in tokamaks are types of low-activation ferritic steel [108]. This is due to their ability to withstand heavy neutron bombardment as well as to reduce the toroidal field ripple or error-fields in general. There are, however, potential drawbacks that arise from the materials' ferromagnetic properties, most notably (i) reduced MHD stability, (ii) increased error-field response and (iii) reduced effectiveness of correction and feedback coils. The impact of the ferritic wall depends primarily upon the saturated permeability (typically $\mu/\mu_0 \sim 2-4$), the wall thickness and the wall radius. Since the study of ferritic materials is a relatively new and unexplored topic, we provide some background of existing studies before discussing the open questions to be explored.

Tokamak experiments with various ferritic wall configurations were reported in 2003 for JFT-2M in Japan [109]. No adverse effects on plasma stability were observed, and in addition the toroidal field ripple and associated particle losses were greatly reduced. While this experiment bodes well for the use of ferritic steels, the experimental range of wall parameters is fairly limited, particularly a relatively distant wall radius ($r_w = 1.6a$). A line-tied pinch experiment in 2008 at Wisconsin [110] reports quite extreme ferritic effects. The observed growth rates are larger than theoretically predicted, an order of magnitude larger than without the ferritic wall. This disagreement with the previous experiment, probably due to a much closer ferritic wall, begs further investigation. Most recently the HBT-EP tokamak at Columbia installed internal ferritic tiles [111], with movable walls which allow variation of the plasma-wall interaction. The experiments resulted in moderate but significant ferritic effects with the closer wall configuration, including larger growth rates and error-field response (up to a factor of two), and higher plasma disruptivity [3]. Furthermore the HBT-EP experiments found that feedback control is possible despite the ferritic material but requires higher gains [29].

In conjunction with the JFT-2M experiments, Bakhtiari [112] developed an analytic zero-β cylindrical tearing-mode model, including a ferritic-resistive wall with finite thickness. This model showed

only a slight reduction in the stabilizing effect of the resistive wall in the desired experimental range of JFT-2M, but with a strong dependence on wall position. Extensive numerical calculations were carried out by Kurita for the ideal kink and RWM, including a varying current profile and poloidal mode spectrum (m=1,...,10), first in cylindrical [113] and later in toroidal [114] geometry. The JFT-2M parameters reduced the theoretical β limit by 10%. Toroidal coupling was found to have little effect on the β limit, but a significant increase in the critical rotation and a narrowing of the rotation stability window. There is no discussion of the effects on the eigenmode spectrum, which is an important topic for error-fields and feedback control. A set of analytic [115] and numerical [116, 117] calculations by Pustovitov predict little ferritic effect on a wall with a short resistive timescale ('slow RWM'), but larger effect near the ideal wall β limit where the resistive skin depth is much smaller than the wall thickness ('fast RWM'). This makes sense in the context of the Brennan-Finn β limits, where the resistive-wall mode tail gradually crosses marginal stability while the ideal-wall growth rate sharply rises near the β limit. In disagreement with Kurita, Pustovitov predicts *improved* rotational stabilization with a ferritic wall, an issue that requires further investigation. Lastly, Fitzpatrick recently used a cylindrical low-β model to calculate the marginal-stability error-field response of the ideal kink [118] and tearing mode [119]. In disagreement with Pustovitov, Fitzpatrick finds the ideal-wall stability limit unaffected by its ferritic properties as well as a detrimental effect on rotational stabilization. These issues require investigation. Fitzpatrick also predicts a lower critical amplitude for the tearing mode and a shrinkage of the forbidden rotation band that separates fast and slow tearing modes.

While some of the disagreements among the papers above stem from uncertainty over the appropriate parameter range for the next stage of tokamaks, several crucial physics issues remain unresolved:

1. The role of rotational stabilization is under dispute, due to the complicated opposing effects of the stabilizing eddy currents and destabilizing ferromagnetic effect in the thick resistive-ferritic wall. In order to better understand this issue, the ferritic and resistive layers are separated in the present formulation as well as in the sharp-boundary version presented in the next chapter. Decoupling the resistive wall time from the effective permeability may clarify the contribution of each to rotational effects. Separating the two layers also allows for an interesting comparison between a ferritic-resistive wall and a resistive-ferritic wall (by radial order), where the jump

across the resistive layer implies that the two cases do not commute (this is in agreement with Pustovitov's proof that a combined ferritic-resistive thin-layer approximation is not possible).

2. The 4-β limits of Brennan and Finn [4] have yet to be studied with ferritic effects. Existing analytic studies describe a single kink or tearing mode, and do not study the entire MHD mode as a whole. An interesting point raised by both Kurita and Fitzpatrick is the change in the β limit even in the absence of a resistive wall. This is somewhat surprising given that the dominant effect of the ferritic material is to reduce the stabilizing effect of an ideal wall (which appears effectively farther away). Since the no-wall and resistive-wall β limits are identical, it follows that the μ affects the resistive-wall β-limit as well as the ideal-wall limit.

3. Multi-mode studies in realistic geometry are expected to reveal changes in mode-spectrum of both the intrinsic modes and the error-field response. Due to the m-dependence of the ferritic boundary condition, each Fourier component of the eigenmode is affected differently. Another multi-mode effect is the shifting of the marginally-stable mode spectrum with the shifting of the β-limit.

4. The sharp-boundary model calculates the equilibrium and stability limits self-consistently, unlike some existing models which utilize pre-calculated equilibrium parameters and then super-impose a ferritic boundary condition. The extent of the this distinction remains to be examined.

5. Error-field response should be distinguished from the error-field itself. While the error-field at the plasma surface is mitigated by the ferritic layer, the error-field *response* may be amplified, as suggested by the RMP response studies at HBT-EP.

Feedback Control

Robust feedback control of MHD instabilities in a tokamak has yet to be attained and is still an active field of study. The present study was motivated in great part by previous work of the HBT-EP group, which has consistently pioneered the development of active feedback control over the past two decades, including a variety of theory [21, 44, 47, 120–122], experimental [3, 20, 22, 29, 40, 123] and engineering [19, 23–25] techniques. In particular, the new model was motivated by the VALEN code [47, 122], which calculates the response of a perturbed plasma equilibrium to a set of

intricately characterized external conductors and active coils, but does not self-consistently include these external features in the equilibrium calculation. The present model, while less accurate, includes the external conducting wall in the perturbed equilibrium calculation, and is thus well suited for examining the response to feedback control as well. This dissertation only touched upon one aspect of MHD feedback control, namely the stabilizable space with respect to rotation or an equivalent feedback control with imaginary normal-field gain. The next step is to reexamine the stability problem in the presence of both normal-field and poloidal-field feedback gains.

Generalizing the cylindrical study by Brennan and Finn [4], the shaped sharp-boundary model can be extended to include feedback control by replacing the uniform conducting wall boundary condition with a field distribution located at the same radius, emulating the effect of feedback control coils. The feedback gains for the normal and poloidal field sensors, described in the single-mode model by complex scalars, must now be described by complex gain matrices. A major challenge in the modernization of active feedback control for MHD instabilities is optimization of these gain matrices, which define the approach of the feedback system. For example, a simple approach known as the *smart shell* method [19] creates a control field which exactly mirrors the perturbed flux at the sensors. Due to a variety of geometric and phasing effects, this approach tends to destabilize sub-dominant modes as it stabilizes the dominant mode [29]. More advanced methods involve a *state space* formulation with a cost functional that defines the desired characteristics [21, 23, 24, 121]. This method is more powerful but opens up many new questions of how to characterize the system and optimize it. The VALEN code can be used to characterize the system but assumes a predefined mode structure, typically obtained from DCON [100].

In order to extend the Brennan-Finn method of studying the system stability over a broad range of complex feedback gains, it will be necessary first to design the appropriate structure for the gain matrices. Note that in contrast with feedback methods that seek to slow the growth of instabilities, the new approach strives to completely suppress the instabilities by raising the β-limit in the stabilizable domain beyond the limit of intrinsic stability.

Error-Field Response

Slight coil misalignments can induce undesirable asymmetries in the equilibrium magnetic field, known as *error-fields*. As they penetrate the plasma, error-fields tend to induce tearing modes and apply torques that can slow or even lock the plasma rotation, thus eliminating the rotational stabi-

lization and permitting the growth of coupled resistive-plasma resistive-wall modes. The HBT-EP experiment utilizes a high resolution array of control coils to generate resonant magnetic perturbations in order to examine the effect on mode structure and stability [26]. Modeling the plasma response to error-fields remains an active field of study [69, 77, 92, 124–129].

Since the new sharp-boundary model originated in an error-field response model by Fitzpatrick [69], all of the ingredients for a follow-up study are already in place. The error-field response calculation was implemented in early versions of the code but still needs updating to incorporate new additions such as full $O(\epsilon)$ toroidal curvature, up-down asymmetry and a conducting wall. Fitzpatrick used singular value decomposition to determine the most harmful error-field, that is the error-field structure that applies the most torque, but was not interested in the ensuing effect on stability. The new model, with the addition of a conducting wall, can examine resistive-plasma resistive-wall mode stability in the presence of error-fields. The error-field boundary condition can be conveniently applied in the same manner as the feedback control condition.

Time Evolution

A well-known paper by Fitzpatrick [130] combines the single-mode linear RWM dispersion relation with a non-linear equation for a torque driven by a static error-field. Replacing the growth rate γ in the dispersion relation by d/dt allows the system to be evolved in time. In conjunction with the temporal evolution, β can be ramped up to simulate a start-up scenario. With the multi-harmonic stability and torque equations already in place, the model contains all of the necessary tools for time-evolution. This non-linear simulation in realistic geometry could specify either a destructive error-field or a constructive feedback control boundary condition, while maintaining the simplicity and minimal computational cost of the sharp-boundary model.

Bibliography

[1] Robert S. Shankland. *Atomic and Nuclear Physics*. The MacMillan Company, second edition.

[2] J.P. Freidberg and W. Grossmann. Magnetohydrodynamic stability of a sharp boundary model of tokamak. *Phys. Fluids*, 18(11):1494–1506, 1975.

[3] J. P. Levesque, P. E. Hughes, J. Bialek, P. J. Byrne, M. E. Mauel, G. A. Navratil, Q. Peng, D. J. Rhodes, and C. C. Stoafer. Active and passive kink mode studies in a tokamak with a movable ferromagnetic wall. *Phys. Plasmas*, 22:056102, 2015.

[4] D. P. Brennan and J. M. Finn. Control of linear modes in cylindrical resistive magnetohydrodynamics with a resistive wall, plasma rotation, and complex gain. *Phys. Plasmas*, 21(10):102507, 2014.

[5] J. M. Finn. Resistive wall stabilization of kink and tearing modes. *Phys. Plasmas*, 2(1):198–204, January 1995.

[6] Charles Seife. *Sun In A Bottle*. Viking, 2008.

[7] Daniel Cleary. *A Piece of the Sun*. Overlook Duckworth, Peter Mayer Publishers, 2013.

[8] Samuel Glasstone and Ralph H. Lovberg. *Controlled Thermonuclear Reactions*. Van Nostrand Reinhold Company, 1960.

[9] J. Wesson. *Tokamaks*. Oxford University Press, 2004.

[10] Michael D. Lemonick. The First Starlight. *Scientific American*, April 2014.

[11] M. Stix. On the time scale of energy transport in the sun. *Solar Phys.*, 2003.

[12] S Pfalzner. *An Introduction to Inertial Confinement Fusion*. CRC Press, 2006.

[13] Stefano Atzeni and Jürgen Meyer ter Vehn. *The physics of inertial fusion.* Oxford University Press, 2004.

[14] R. J. Goldston and P. H. Rutherford. *Plasma Physics.* Taylor and Francis Group, 1995.

[15] Paul Bellan. *Fundamentals of Plasma Physics.* Cambridge U. Press, 2006.

[16] R. Fitzpatrick. *Plasma Physics.* CRC Press, 2015.

[17] `http://www.iter.org`.

[18] Edward Teller. *Energy from Heaven and Earth.* W. H. Freeman and company, 1979.

[19] C. Cates, M. Shilov, M. E. Mauel, G. A. Navratil, D. Maurer, S. Mukherjee, D. Nadle, J. Bialek, and A. Boozer. Suppression of resistive wall instabilities with distributed, independently controlled, active feedback coils. *Phys. Plasmas*, 7(8):3133, 2000.

[20] M. E. Mauel, J. Bialek, A. H. Boozer, C. Cates, R. James, O. Katsuro-Hopkins, A. Klein, Y. Liu, D. A. Maurer, D. Maslovsky, G. A. Navratil, T. S. Pederson, M. Shilov, and N. Stillits. Dynamics and control of resistive wall modes with magnetic feedback control coils: experiment and theory. *Nucl. Fusion*, 45:285–293, 2005.

[21] O. Katsuro-Hopkins, J. Bialek, D. A. Maurer, and G. A. Navratil. Enhanced iter resistive wall mode feedback performance using optimal control techniques. *Nucl. Fusion*, 47:1157–1165, 2007.

[22] J. M. Hanson, B. DeBono, R. W. James, J. P. Levesque, M. E. Mauel, D. A. Maurer, G. A. Navratil, T. S. Pedersen, and D. Shiraki. Feedback suppression of rotating external kink instabilities in the presence of noise. *Phys. Plasmas*, 15:080704, 2008.

[23] J. M. Hanson, B. DeBono, J. P. Levesque, M. E. Mauel, D. A. Maurer, G. A. Navratil, T. S. Pedersen, D. Shiraki, and R. W. James. A Kalman filter for feedback control of rotating external kink instabilities in the presence of noise. *Phys. Plasmas*, 16:080704, 2009.

[24] J. M. Hanson, A. J. Klein, M. E. Mauel, D. A. Maurer, and G. A. Navratil. A digital control system for external magnetohydrodynamic modes in tokamak plasmas. *Rev. Sci. Instrum*, 80:043503, 2009.

[25] N. Rath, J. Bialek, P. J. Byrne, B. DeBono, J. P. Levesque, B. Li, M. E. Mauel, D. A. Maurer, G. A. Navratil, and D. Shiraki. High-speed, multi-input, multi-output control using GPU processing in the HBT-EP tokamak. *Fusion Engineering and Design*, 87(1895), 2012.

[26] D. Shiraki, S. M. Angelini, P. J. Byrne, B. A. DeBono, and P. E. Hughes et. al. Measurement of 3D plasma response to external magnetic perturbations in the presence of a rotating external kink. *Phys. Plasmas*, 20:102503, 2013.

[27] T. H. Ivers, E. Eisner, A. Garofalo, R. Kombargi, M. E. Mauel, D. Maurer, D. Nadle, G. A. Navratil, M. K. V. Sankar, M. Su, E. Taylor, Q. Xiao, R. R. Bartsch, W. A. Reass, , and G. A. Wurden. Observation of wall stabilization and active control of low-n magnetohydrodynamic instabilities in a tokamak. *Phys. Plasmas*, 3(5):19261934, 1996.

[28] D. A. Maurer, J. Bialek, P. J. Byrne, B. D. Bono, J. P. Levesque, B. Q. Li, M. E. Mauel, Navratil G. A., T. S. Pedersen, N. Rath, and D. Shiraki. The high beta tokamak-extended pulse magnetohydrodynamic mode control research program. *Plasma Physics and Controlled Fusion*, 53(7):074016, 2011.

[29] Q. Peng, J. P. Levesque, C. C. Stoafer, J. Bialek, P. Byrne, P. E. Hughes, M. E. Mauel, G. A. Navratil, and D. J. Rhodes. Improved feedback control of wall stabilized kink modes with different plasma-wall couplings and mode rotation. *Plasma Phys. Control. Fusion*, 58:045001, 2016.

[30] E. J. Strait, T. S. Taylor, A. D. Turnbull, J. R. Ferron, L. L. Lao, B. Rice, O. Sauter, and S. J. Thompson. Wall stabilization of high beta tokamak discharges in DIII-D. *Phys. Rev. Lett.*, 74(13):2483, 1995.

[31] M. Okabayashi, N. Pomphrey, J. Manickam, D. J. Ward, R. E. Bell, R. E. Hatcher, R. Kaita, S. M. Kaye, H. W. Kugel, B. LeBlanc, F. M. Levinton, D. W. Roberts, S. Sesnic, Y. Sun, and H. Takahashi. Role of the stabilizing shell in high-beta, low-q disruptions in PBX-M. *Nucl. Fusion*, 36(9):1167, 1996.

[32] A. M. Garofalo, E. Eisner, T. H. Ivers, R. Kombargi, M. E. Mauel, D. Maurer, D. Nadle, G. A. Navratil, M. K. Vijaya Sankar, E. Taylor, and Q. Xiao. Stabilization of kink instabilities by eddy currents in a segmented wall and comparison with ideal mhd theory. *Nucl. Fusion*, 38(7):1029, 1998.

[33] A. Bondeson and D.J. Ward. Stabilization of external modes in tokamaks by resistive walls and plasma rotation. *Phys. Rev. Lett.*, 72(17):2709, 1994.

[34] A.H. Boozer. Stabilization of resistive wall modes by slow plasma rotation. *Phys. Plasmas*, 2:4521, 1995.

[35] M. S. Chu, J. M. Greene, T. H. Jensen, R. L. Miller, A. Bondeson, R. W. Johnson, and M. E. Mauel. Effect of toroidal plasma flow and flow shear on global magnetohydrodynamic MHD modes. *Phys. Plasmas*, 2(6):2236–2241, June 1995.

[36] R. Fitzpatrick and A. Y. Aydemir. Stabilization of the resistive shell mode in tokamaks. *Nucl. Fusion*, 36(1):11–38, 1996.

[37] R. Betti. Beta limits for the n=1 mode in rotating-toroidal-resistive plasmas surrounded by a resistive wall. *Phys. Plasmas*, 5(10):3615, 1998.

[38] B. Hu and R. Betti. Resistive wall mode in collisionless quasistationary plasmas. *Phys. Rev. Lett.*, 93(10):105002, 2004.

[39] J. W. Berkery, Y. Q. Liu, Z. R. Wang, S. A. Sabbagh, N. C. Logan, J. K. Park, J. Manickam, and R. Betti. Benchmarking kinetic calculations of resistive wall mode stability. *Phys. Plasmas*, 21:052505, 2014.

[40] G. A. Navratil, C. Cates, M. E. Mauel, D. Maurer, D. Nadle, E. Taylor, Q. Xiao, W. A. Reass, and G. A. Wurden. Active control of 2/1 magnetic islands in a tokamak. *Phys. Plasmas*, 5:1855, 1998.

[41] M. Okabayashi, J. Bialek, M. S. Chance, M. S. Chu, E. D. Fredrickson, A. M. Garofalo, M. Gryaznevich, R. E. Hatcher, T. H. Jensen, L. C. Johnson, R. J. La Haye, E. A. Lazarus, M. A. Makowski, J. Manickam, G. A. Navratil, J. T. Scoville, E. J. Strait, A. D. Turnbull, M. L. Walker, and the DIII-D Team. Active feedback stabilization of the resistive wall mode on the DIII-D device. *Phys Plasmas*, 8(5).

[42] C. G. Gimblett. Stabilization of thin shell modes by a rotating secondary wall. *Plasma Phys. Control. Fusion*, 31:2183, 1989.

[43] R. Fitzpatrick and T. H. Jensen. Stabilization of the resistive wall mode using a fake rotating shell. *Phys. Plasmas*, 3:2641, 1996.

[44] A.H. Boozer. Equations for studies of feedback stabilization. *Phys. Plasmas*, 5(9), 1998.

[45] Y. Q. Liu and A. Bondeson. Active feedback stabilization of toroidal external modes in tokamaks. *Phys. Rev. Lett*, 84(5):907, 2000.

[46] C. G. Gimblett and R. J. Hastie. A rotating shell and stabilization of the tokamak resistive wall mode. *Phys. Plasmas*, 7:5007, 2000.

[47] J. Bialek, A. H. Boozer, M. E. Mauel, and G. A. Navratil. Modeling of active control of external magnetohydrodynamic instabilities. *Phys. Plasmas*, 8:2170, 2001.

[48] J. M. Finn and L. Chacón. Control of linear and nonlinear resistive wall modes. *Phys. Plasmas*, 11(5):1866, 2004.

[49] J.P. Freidberg. *Ideal MHD*. Cambridge Univ. Press, 2nd edition.

[50] H.P. Furth, J. Killeen, and M.N. Rosenbluth. Finite-resistivity instabilities of a sheet pinch. *Phys. Fluids*, 6(4):459, 1963.

[51] R. Fitzpatrick. Interaction of tearing modes with external structures in cylindrical geometry. *Nucl. Fusion*, 33:1049, 1993.

[52] J. M. Finn. Stabilization of ideal plasma resistive wall modes in cylindrical geometry: The effect of resistive layers. *Phys. Plasmas*, 2(10):3782, 1995.

[53] A. S. Richardson, J. M. Finn, and G. L. Delzanno. Control of ideal and resistive magnetohydrodynamic modes in reversed field pinches with a resistive wall. *Phys. Plasmas*, 17:112511, 2010.

[54] J.P. Freidberg and F.A. Haas. Kink instabilities in a high-beta tokamak with elliptic cross section. *Phys. Fluids*, 17:440, 1974.

[55] E. A. Lazarus, L. L. Lao, T. H. Osborne, T. S. Taylor, A. D. Turnbull, M. S. Chu, A. G. Kellman, E. J. Strait, J. R. Ferron, R. J. Groebner, W. W. Heidbrink, T. Carlstrom, F. J. Helton, C. L. Hsieh, S. Lippmann, D. Schissel, R. Snider, and D. Wroblewski. An optimization of beta in the DIIID tokamak. *Phys. Fluids B*, 4:3644, 1992.

[56] A. D. Turnbull, T. S. Taylor, M. S. Chu, R. L. Miller, and Y. R. Lin-Liu. Synergism between cross-section and profile shaping in beta optimization of tokamak equilibria with negative central shear. *Nucl. Fusion*, 38(10):1467, 1998.

[57] C. E. Kessel, J. R. Ferron, C. M. Greenfield, J. E. Menard, , and T. S. Taylor. Shape optimization for DIII-D advanced tokamak plasmas. *30th EPS Conference on Contr. Fusion and Plasma Phys., St. Petersburg*, 27A:4.44, 2003.

[58] J. R. Ferron, T. A. Casper, E. J. Doyle, A. M. Garofalo, P. Gohil, C. M. Greenfield, A. W. Hyatt, R. J. Jayakumar, C. Kessel, J. Y. Kim, T. C. Luce, M. A. Makowski, J. Menard, M. Murakami, C. C. Petty, P. A. Politzer, T. S. Taylor, , and M. R. Wade. Optimization of

DIII-D advanced tokamak discharges with respect to the beta limit. *Phys. Plasmas*, 12:056126, 2005.

[59] S. M. Kaye C. E. Kessel J. Manickam J. E. Menard, S. C. Jardin. Ideal MHD stability limits of low aspect ratio tokamak plasmas. *Nucl. Fusion*, 37:595, 1997.

[60] R. L. Miller, Y. R. Lin-Liu, A. D. Turnbull, V. S. Chan, L. D. Pearlstein, O. Sauter, and L. Villard. Stable equilibria for bootstrap-current-driven low aspect ratio tokamaks. *Phys. Plasmas*, 4:1062, 1997.

[61] A. D. Turnbull, Y. R. Lin-Liu, R. L. Miller, T. S. Taylor, , and T. N. Todd. Improved magnetohydrodynamic stability through optimization of higher order moments in cross-section shape of tokamaks. *Phys. Plasmas*, 6:1113, 1999.

[62] A. Bondeson and M.-N. Bussac. Stability of the n=1 ideal internal kink for large aspect ratio Shafranov equilibria. *Nucl. Fusion*, 32:513, 1992.

[63] H. Lutjens, A. Bondeson, and G. Vlad. Ideal MHD stability of internal kinks in circular and shaped tokamaks. *Nucl. Fusion*, 32:1625–1636, 1992.

[64] H.G. Eriksson and C. Wahlberg. Effect of combined triangularity and ellipticity on the stability limit of the ideal internal kink mode in a tokamak. *Phys. Plasmas*, 9(5):1606–1621, 2001.

[65] A. Martynov, J. P. Graves, and O. Sauter. The stability of the ideal internal kink mode in realistic tokamak geometry. *Plasma Phys. Control. Fusion*, 47:1743–1762, 2005.

[66] R. Fitzpatrick, R. J. Hastie, T. J. Martin, and C. M. Roach. Stability of coupled tearing modes in tokamaks. *Nucl. Fusion*, 33:1533, 1993.

[67] C. J. Ham, Y. Q. Liu, J. W. Connor, S. C. Cowley, R. J. Hastie, T. C. Hender, and T. J. Martin. Tearing stability in toroidal plasmas with shaped cross section. *Plasma Phys. Control. Fusion*, 54:105014, 2012.

[68] S. E. Kruger, C. C. Hegna, and J. D. Callen. Geometric influences on neoclassical magnetohydrodynamic tearing modes. *Phys. Plasmas*, 5(2):455, 1998.

[69] R. Fitzpatrick. A nonideal error-field response model for strongly shaped tokamak plasmas. *Phys. Plasmas*, 17:112502, 2010.

[70] V. D. Shafranov. Hydromagnetic stability of a current-carrying pinch in a strong longitudinal magnetic field. *Sov. Phys. - Tech. Phys.*, 15:175, 1970.

[71] B.B. Kadomtsev and O.P. Pogutse. Nonlinear helical perturbations of a plasma in the tokamak. *Sov. Phys.-JETP*, 38:283, 1973.

[72] M. N. Rosenbluth, D. A. Monticello, H. R. Strauss, and R. B. White. Numerical studies of nonlinear evolution of kink modes in tokamaks. *Phys. Fluids*, 19(1987), 1976.

[73] H. R. Strauss. Nonlinear, three-dimensional magnetohydrodynamics of noncircular tokamaks. *Phys. Fluids*, 19(134), 1976.

[74] H. R. Strauss. Dynamics of high beta tokamaks. *Phys. Fluids*, 20(1354), 1977.

[75] B. B. Kadomtsev. *Tokamak plasma: a complex physical system.* Plasma Physics Series. IOP Publishing, 1992.

[76] R. D. Hazeltine and J. D. Meiss. *Plasma Confinement.* Dover, 2003.

[77] A.J. Cole and R. Fitzpatrick. Drift-magnetohydrodynamical model of error-field penetration in tokamak plasmas. *Phys. Plasmas*, 13:032503, 2006.

[78] J.W. Connor, S. C. Cowley, R. J. Hastie, T. C. Hender, A. Hood, and T. J. Martin. Tearing modes in toroidal geometry. *Phys. Fluids*, 31:577, 1988.

[79] Glenn Bateman. *Magnetohydrodynamic Instabilities.* MIT Press, 1978.

[80] J.P. Freidberg and F.A. Haas. Kink instabilities in a high-beta tokamak. *Phys. Fluids*, 16:1909, 1973.

[81] B. M. Marder. Kink instabilities in the belt pinch. *Phys. Fluids*, 17:447, 1974.

[82] B. M. Marder. Kink instabilities in arbitrary cross-section plasmas. *Phys. Fluids*, 17:634, 1974.

[83] J.P. Goedbloed. Free-boundary high-beta tokamaks. III. Free-boundary stability. *Phys. Fluids*, 25:2073–2088, 1982.

[84] R. Fitzpatrick. A sharp boundary model for the vertical and kink stability of large aspect-ratio vertically elongated tokamak plasmas. *Phys. Plasmas*, 15:092502, 2008.

[85] J. W. Connor and R. J. Hastie. The effect of shaped plasma cross sections on the ideal internal kink mode in a tokamak. Technical Report CLM-M106, Culham Laboratory, 1985. Journal Ref: Phys. Fluids Document No. PFLDA-30-1730-36.

[86] R. L. Miller, M. S. Chu, J. M. Greene, Y. R. Lin-Liu, and R. E. Waltz. Noncircular, finite aspect-ratio, local equilibrium model. *Phys. Plasmas*, 5:973, 1998.

[87] V. Mukhovatov and M. Shimada. Overview of physics basis for ITER. *Plasma Phys. Control. Fusion*, 45:A235–A252, 2003.

[88] R. Fitzpatrick, C. G. Gimblett, and R. J. Hastie. On the "1 1/2-D" evolution of tokamak plasmas in the case of large aspect ratio. *Plas. Phys. Control. Fusion*, 34:161–174, 1992.

[89] W. D. D'haeseleer, W. N. G. Hitchon, J. D. Callen, and J. L. Shohet. *Flux coordinates and magnetic field structure*. Springer series in computational physics. Springer-Verlag, 1991.

[90] J.D. Jackson. *Classical Electrodynamics*. John Wiley and Sons, 3rd edition.

[91] G. T. A. Huysmans, J. P. Goedbloed, and W. Kerner. Free boundary resistive modes in tokamaks. *Phys. Fluids*, 5:1545, 1993.

[92] J. M. Finn, A. J. Cole, and D. P. Brennan. Error field penetration and locking to the backward propagating wave. *Phys. Plasmas*, 22:120701, 2015.

[93] J. A. Nelder and R. Meade. A simplex method for function minimization. *The Computer Journal*, 7(4):308–313, 1965.

[94] Eric Jones, Travis Oliphant, Pearu Peterson, et al. SciPy: Open source scientific tools for Python, 2001–. `http://www.scipy.org`.

[95] A.A. Ware and F.A. Haas. Stability of a circular toroidal plasma under average magnetic well conditions. *Phys. Fluids*, 9(5):956, 1966.

[96] F.J. Helton and T.S. Wang. MHD Equilibrium in Non-Circular Tokamaks With Field Shaping Coil Systems. *Nucl. Fusion*, 18(11):1523, 1978.

[97] C.E. Kessel, T. K. Mau, S. C. Jardin, and F. Najmabadi. Plasma profile and shape optimization for the advanced tokamak power plant, ARIES-AT. *Fusion Engng. Des.*, 80:63–77, 2006.

[98] J.P. Freidberg, A. Cerfon, and J. P. Lee. Tokamak elongation - how much is too much? Part 1. Theory. *J. Plasma Phys.*, 81(6):515810607, 2015.

[99] J.P. Lee, A. Cerfon, J. P. Freidberg, and M. Greenwald. Tokamak elongation - how much is too much? Part 2. Numerical Results. *J. Plasma Phys.*, 81(6):515810608, 2015.

[100] A. H. Glasser. The direct criterion of Newcomb for the ideal mhd stability of an axisymmetric toroidal plasma. *Phys. Plasmas*, 23:072505, 2016.

[101] B. Coppi, A. Ferreira, J. W.-K. Mark, and J. J. Ramos. Ideal-MHD stability of finite-beta plasmas. *Nucl. Fusion*, 19:715, 1979.

[102] B. Coppi, A. Ferreira, and J. J. Ramos. Self-healing of confined plasmas with finite pressure. *Phys. Rev. Lett.*, 44(15):990, 1980.

[103] W. H. Choe and J. P. Freidberg. Finite shift stabilization of ballooning modes in a high-beta tokamak. *Phys. Fluids*, 29:1766, 1986.

[104] M. E. Mauel. Ballooning mode stability of high-beta tokamaks. *Phys. Fluids*, 30:3843, 1987.

[105] R. Betti and J.P. Freidberg. Stability Analysis of Resistive Wall Kink Modes in Rotating Plasmas. *Phys. Rev. Lett.*, 74(15):2949, 1995.

[106] J. M. Finn and R. A. Gerwin. Mode coupling effects on resistive wall instabilities. *Phys. Plasmas*, 3:2344, 1996.

[107] A. Bondeson, C. G. Gimblett, and R. J. Hastie. Resistive wall mode stabilization in toroidal geometry. *Phys. Plasmas*, 6(3):637, 1994.

[108] Seki et. al. Proc. 13th Int. Conf. on Plasma Physics and Controlled Nuclear Fusion Research (Washington, DC, 1990). *Vienna IAEA*, 3:473, 1991.

[109] K. Tsuzuki et. al. High performance tokamak experiments with a ferritic steel wall on JFT-2M. *Nucl. Fusion*, 43:1288–1293, 2003.

[110] W. F. Bergerson, D. A. Hannum, C. C. Hegna, R. D. Kendrick, J. S. Sarff, and C. B. Forest. Observation of Resistive and Ferritic Wall Modes in a Line-Tied Pinch. *Phys. Rev. Lett.*, 101:235005, 2008.

[111] P. E. Hughes, J. P. Levesque, N. Rivera, M. E. Mauel, and G. A. Navratil. Design and installation of a ferromagnetic wall in tokamak geometry. *Rev Sci Instrum*, 86:103504, 2015.

[112] M. Bakhtiari, M. Azumi, K. Tsuzuki, K. Kamiya, H. Kawashima, Y. Kusama, M. Sato, K. Hoshino, and JFT-2M Group. Effect of a ferromagnetic wall on low-beta tearing modes in the Japan Atomic Energy Research Institute Fusion Torus-2 Modified. *Phys. Plasmas*, 10(8):3212, 2003.

[113] G. Kurita, T. Tuda, M. Azumi, S. Ishida, S. Takeji, A. Sakasai, M. Matsukawa, T. Ozeki, and M. Kikuchi. Ferromagnetic and resistive wall effects on the beta limit in a tokamak. *Nucl. Fusion*, 43:949, 2003.

[114] G. Kurita, J. Bialek, T. Tuda, M. Azumi, S. Ishida, G. A. Navratil, S. Sakurai, H. Tamai, M. Matsukawa, T. Ozeki, M. S. Chu, M. S. Chance, and Y. Miura. Critical beta analyses with ferromagnetic and plasma rotation effects and wall geometry for a high beta steady state tokamak. *Nucl. Fusion*, 46:383, 2006.

[115] V. D. Pustovitov. Resistive ferromagnetic wall modes in theory and experiment. *Phys. Plasmas*, 16:052503, 2009.

[116] V. D. Pustovitov and V. V. Yanovskiy. Ferromagnetic effects in the theory of slow and fast resistive wall modes in tokamaks. *Phys. Plasmas*, 21:022516, 2014.

[117] V. D. Pustovitov and V. V. Yanovskiy. Rotational stabilization of the resistive wall modes in tokamaks with a ferritic wall. *Phys. Plasmas*, 22:032509, 2015.

[118] R. Fitzpatrick. Influence of ferromagnetic walls on resistive wall mode stability in tokamaks. *Plasma Phys. Control. Fusion*, 56:105002, 2014.

[119] R. Fitzpatrick. Braking of tearing mode rotation by ferromagnetic conducting walls in tokamaks. *Phys. Plasmas*, 22:092506, 2015.

[120] A.H. Boozer. Feedback equations for the wall modes of a rotating plasma. *Phys. Plasmas*, 6(8):3180–3187, August 1999.

[121] O. Katsuro-Hopkins, S.A. Sabbagh, and J.M. Bialek. Analysis of resistive wall mode LQG control in NSTX with mode rotation. *Joint 48th IEEE Conference on Decision and Control*, (WeA09.5), 2009.

[122] A.H. Boozer. Simplified multimode calculations of resistive wall modes. *Phys. Plasmas*, 17:072503, 2010.

[123] A. M. Garofalo, A. D. Turnbull, E. J. Strait, M. E. Austin, J. Bialek, M. S. Chu, E. Fredrickson, R. J. La Haye, G. A. Navratil, L. L. Lao, E. A. Lazarus, M. Okabayashi, B. W. Rice, S. A. Sabbagh, J. T. Scoville, T. S. Taylor, M. L. Walker, and The DIII-D Team. Stabilization of the external kink and control of the resistive wall mode in tokamaks. *Phys. Plasmas*, 6(5):1893, 1999.

[124] A.H. Boozer. Error field amplification and rotation damping in tokamak plasmas. *Physical Review Letters*, 86(22):5059–5061, May 2001.

[125] A.H. Boozer. Resistive wall modes and error field amplification. *Phys. Plasmas*, 10(5):1458, May 2003.

[126] Allen H. Boozer and Dmitry Maslovsky. Resistive wall modes and error field amplification. *31st EPS Conference on Plasma Phys. London*, 28G:2.159, 2004.

[127] J. K. Park, A. H. Boozer, J. E. Menard, and M. J. Schaffer. Error field correction in ITER. *Nucl. Fusion*, 48:045006, 2008.

[128] R. Fitzpatrick. Error-field induced electromagnetic torques in a large aspect-ratio, low-beta, weakly shaped tokamak plasma. *Phys. Plasmas*, 16:032502, 2009.

[129] R. Fitzpatrick. Nonlinear error-field penetration in low density ohmically heated tokamak plasmas. *Plasma Phys. Control. Fusion*, 54:094002, 2012.

[130] R. Fitzpatrick. A simple model of the resistive wall mode in tokamaks. *Phys. Plasmas*, 9(8):3459, 2002.

[131] J. D. Hunter. Matplotlib: A 2D graphics environment. *Computing In Science & Engineering*, 9(3):90–95, 2007.

[132] F. Troyon, A. Roy, W. A. Cooper, F. Yasseen, and A. Turnbull. Beta limit in tokamaks: Experimental and computational status. *Plasma Physics and Controlled Fusion*, 30(11):1597–1609, 1988.

Appendix A

Toroidal Flux Coordinate Representations

This appendix describes flux coordinates in a torus, and also includes mathematical relations used in generalized coordinate calculations.

A.1 Flux Coordinates

The magnetic field in a tokamak can be visualized as a set of nested toroidal surfaces containing constant magnetic flux. Following the textbook by D'haeseleer et. al. [89], the magnetic field on a flux surface can expressed in terms of its toroidal and poloidal components

$$\boldsymbol{B} = \boldsymbol{B}_T + \boldsymbol{B}_P, \tag{A.1}$$

$$= I(\psi)\boldsymbol{\nabla}\phi + \boldsymbol{\nabla}\phi \times \boldsymbol{\nabla}\psi. \tag{A.2}$$

The field is characterized by a flux-surface label ψ and a toroidal angle ϕ. There is also a poloidal angle θ which does not appear explicitly but is defined in terms of the other variables and will be discussed shortly. By definition there is no perpendicular field component on a flux surface, since the coordinates follow the magnetic field-lines, so that $\boldsymbol{B}\cdot\boldsymbol{\nabla}\psi = 0$. Taking the magnitude of the toroidal component

$$B_T = I(\psi)|\boldsymbol{\nabla}\phi|, \tag{A.3}$$

provides an expression for the toroidal flux function

$$I(\psi) = \frac{B_T}{|\boldsymbol{\nabla}\phi|}. \tag{A.4}$$

Similarly taking the magnitude of the poloidal component

$$B_P = |\boldsymbol{\nabla}\phi||\boldsymbol{\nabla}\psi| = |\boldsymbol{\nabla}\phi|\psi'(r)|\boldsymbol{\nabla}r|, \tag{A.5}$$

with the flux label expressed as a function of a radial variable r, gives an expression for the poloidal flux function

$$\psi'(r) = \frac{B_P}{|\boldsymbol{\nabla}\phi||\boldsymbol{\nabla}r|}. \tag{A.6}$$

Using the expressions in Equations (A.4) and (A.6), the magnetic field in Equation (A.2) can be rewritten as

$$\boldsymbol{B} = B_T \frac{\boldsymbol{\nabla}\phi}{|\boldsymbol{\nabla}\phi|} + B_P \frac{\boldsymbol{\nabla}\phi}{|\boldsymbol{\nabla}\phi|} \times \frac{\boldsymbol{\nabla}r}{|\boldsymbol{\nabla}r|} \tag{A.7}$$

$$\equiv B_T \hat{\boldsymbol{e}}_\phi + B_P \hat{\boldsymbol{e}}_\phi \times \hat{\boldsymbol{e}}_r, \tag{A.8}$$

in terms of normalized contravariant basis vectors. The final expression makes it clear that $\hat{\boldsymbol{e}}_\theta = \hat{\boldsymbol{e}}_\phi \times \hat{\boldsymbol{e}}_r$ is the component associated with the implicit poloidal angle θ. This normalized contravariant basis

$$\hat{\boldsymbol{e}}_r \equiv \boldsymbol{\nabla}r/|\boldsymbol{\nabla}r|, \qquad \hat{\boldsymbol{e}}_\theta \equiv \boldsymbol{\nabla}\theta/|\boldsymbol{\nabla}\theta|, \qquad \hat{\boldsymbol{e}}_\phi \equiv \boldsymbol{\nabla}\phi/|\boldsymbol{\nabla}\phi|, \tag{A.9}$$

is applied in the error-field response model by Fitzpatrick [69] which is the basis for the present sharp-boundary model. Using the form above, the poloidal field can now be written as

$$B_P = \hat{\boldsymbol{e}}_\phi \times \hat{\boldsymbol{e}}_r \cdot \boldsymbol{B} = \hat{\boldsymbol{e}}_\theta \cdot \boldsymbol{B}, \tag{A.10}$$

and will be evaluated later by the equilibrium pressure balance. The toroidal field magnitude scales according to Ampere's law as

$$B_T = \frac{R_0}{R} B_0, \tag{A.11}$$

where B_0 and R_0 are the toroidal field magnitude and major radius at the magnetic axis.

Up to this point the derivation is general. In a *toroidally symmetric* system where $\partial_\phi = 0$ for all equilibrium quantities, the toroidal basis vector is defined by the orthogonality relations

$$\boldsymbol{\nabla}\phi\cdot\boldsymbol{\nabla}\psi = \boldsymbol{\nabla}\phi\cdot\boldsymbol{\nabla}\theta = 0, \tag{A.12}$$

and its magnitude is given by

$$|\boldsymbol{\nabla}\phi| = \frac{1}{R}. \tag{A.13}$$

In the sharp-boundary model presented in Chapter 5, the other two coordinates r and θ are defined by the cross-sectional parametrization that is independent of the toroidal angle ϕ. Note that the cross-sectional basis vectors $\hat{\boldsymbol{e}}_r$ and $\hat{\boldsymbol{e}}_\theta$ are not necessarily orthogonal to each other. In fact, the sharp-boundary geometry consists of two separate parametrizations; a non-orthogonal internal (plasma) basis and an orthogonal external (vacuum) basis. The details of the sharp-boundary geometry are described in Section 5.1, relating a set of curvilinear flux coordinates (r, θ, ϕ) to a cylindrical polar system (R, ϕ, Z). For reference, we also include below some generalized coordinate relations used in the sharp-boundary model calculations.

A.2 Generalized Coordinate Relations

The Jacobian of a coordinate transformation $\hat{\boldsymbol{x}}(r, \theta, \phi)$ is given by

$$J = \frac{\partial\hat{\boldsymbol{x}}}{\partial r}\cdot\left(\frac{\partial\hat{\boldsymbol{x}}}{\partial\theta}\times\frac{\partial\hat{\boldsymbol{x}}}{\partial\phi}\right). \tag{A.14}$$

Since $dr/dr = \boldsymbol{\nabla}r\cdot\frac{\partial\hat{\boldsymbol{x}}}{\partial r} = 1$, we find the contravariant derivatives from the dual relation

$$\boldsymbol{\nabla}r = J^{-1}\frac{\partial\hat{\boldsymbol{x}}}{\partial\theta}\times\frac{\partial\hat{\boldsymbol{x}}}{\partial\phi}, \tag{A.15}$$

with similar relations for $\boldsymbol{\nabla}\theta$ and $\boldsymbol{\nabla}\phi$. The constravariant derivatives are used to compute the gradient, divergence, curl and Laplacian operators defined below:

$$\boldsymbol{\nabla} f = \sum_{\alpha} \boldsymbol{\nabla}\alpha \partial_{\alpha}, \tag{A.16}$$

$$\boldsymbol{\nabla}\cdot\boldsymbol{A} = J^{-1} \sum_{\alpha} \partial_{\alpha}(J\boldsymbol{\nabla}\alpha \cdot \boldsymbol{A}), \tag{A.17}$$

$$\boldsymbol{\nabla}\times\boldsymbol{A} = J^{-1}\hat{\boldsymbol{e}}_3(\partial_1 A_2 - \partial_2 A_1) + J^{-1}\hat{\boldsymbol{e}}_1(\partial_2 A_3 - \partial_3 A_2) + J^{-1}\hat{\boldsymbol{e}}_2(\partial_3 A_1 - \partial_1 A_3), \tag{A.18}$$

$$\nabla^2 f = \boldsymbol{\nabla}\cdot\boldsymbol{\nabla} f = J^{-1} \sum_{\alpha}\sum_{\beta} \partial_{\alpha}(J\boldsymbol{\nabla}\alpha \cdot \boldsymbol{\nabla}\beta\partial_{\beta} f). \tag{A.19}$$

Appendix B

Code Manual

B.1 Python Code Implementation of the Sharp-Boundary Model

The Nonideal Eigenvalue with Ferritic-Resistive wall (NEFR) code implements the sharp-boundary model in Python. Its main purpose is to calculate the growth rate γ of the fastest growing mode for a given sharp-boundary equilibrium. Three files (in a common directory) are needed to run the code:

1. **nefr_main.py** contains all model calculations.
2. **nefr_toolkit.py** defines inputs, runs and plots.
3. **djr_settings.py** loads packages and plot settings.

Each of these modules, discussed below, is available on the HBT-EP Wiki page or by request: dovjr6@gmail.com.

Physics Module: nefr_main.py

This file contains the heart of the model, split into several functions. There is generally no need to open or modify this file for normal operation.

The *run* object contains all of the default inputs, database specifications and geometric functions. The default parameter initialization in the class definition appears as follows:

PHYSICAL INPUT PARAMETERS

beta = 0.1 # ratio of plasma pressure to magnetic pressure

q0 = 1.1 # central safety factor

qa = 2.1 # edge safety factor

J_spec = 'auto' # resonant surfaces ('auto' if set by $q_0 < m/n < q_p$)

tau_t = 1.0e4 # Plasma tearing dissipation time (in Alfven time)

tau_w = 1.0e3 # Resistive wall dissipation time (in Alfven time)

eps = 0.25 # inverse aspect ratio

kappa = 1.0 # vertical elongation (1.0 for circle)

delta_x = 0.0 # horizontal triangularity parameter

delta_y = 0.0 # divertor asymmetry (vertical triangularity) parameter

omega = 0.0 # plasma rotation frequency (in Alfven frequency)

rw = 1.3 # ferritic-resistive wall radius

mu_eff = 0.0 # effective ferritive permeability: $\delta F \times \mu/\mu_0$

NUMERICAL INPUT PARAMETERS

r0 = finite radius for launching internal solutions

nres = 1 # toroidal mode number

mres = 15 # poloidal mode harmonic spectrum (-mres, +mres)

N_FFT = 512 # Fast Fourier Transform steps

N_RK = 200 # Runge-Kutta (4th order) steps

use_previous = True # option to use previous calculation as initial guess

The main functions are described below. Each function starts out by defining shortcuts to the needed run-object parameters, both for convenience and to highlight the dependencies of the particular function.

1. **calc_CC_internal** radially integrates the perturbed magnetic potential from r0 (near the magnetic axis) outward to the plasma current layer $r = 1$. This vacuum-like (Laplacian) function V is solved as a system of Fourier components which are coupled by the shaped toroidal geometry (neglecting $O(\epsilon^2)$ terms). The system is helically symmetric with a fixed

toroidal Fourier number nres = 1, and the poloidal harmonic structure is resolved by Fast Fourier Transforms. For a system size of $I = 2 \times \text{mres} + 1$, the radial integration is carried out for I different initial conditions in order to span the solution space. The ideal plasma response is then concisely captured by a matrix CC_int which relates the tangential and normal field components at $r = 1-$ (just inside the skin current). For a given geometry CC_int is stored in a numpy zip (.npz) file to be reused when scanning over other parameters such as beta.

2. **calc_CC_external** similarly solves Laplace's equation, integrating from the wall radius rw inward to $r = 1+$ just outside the plasma skin current. The resulting external response matrix CC_ext is stored for reuse in .npz file.

3. **calc_FF_ideal** computes the ideal force matrix, combining internal and external response with additional beta-dependent matrices. This process involves calculation of the equilibrium poloidal field distribution and the resulting contributions from the plasma, vacuum and the perturbed surface. Using the **calc_Bi** function located among the numerical tools, the free parameter B_i of the external field structure is determined by beta (β), qa (q_a) and the equilibrium geometry. The field structure is used to define the ideal components of the energy matrix, including the surface, plasma and vacuum terms.

4. **calc_tearing_matrix** computes the γ-independent tearing (Δ) matrix that contributes to the total force matrix. **calc_Bi** is then used again to compute the field structure at each resonant surface with $q = m/n$, approximating all the surfaces to lie at $r = 1+$ and thus share the same geometric structure. The resulting magnetic field structure for each resonant surface is then used to define a straight field line angle which characterizes the resonant component of the perturbed field. Assumed to all have a common dissipation time tau_t (τ_t), the resonant jump conditions are combined into a single response matrix UU which contributes to the perturbed vacuum energy.

5. **calc_wall_matrices** computes the γ-independent wall matrices that contribute to the total force matrix, including both ferritic and resistive layers. The thin ferritic wall, assumed to lie just inside the resistive wall, contributes an effective jump in each Fourier component of the perturbed normal field. The resistive layer formulation is similar to the tearing response matrix but includes all of the Fourier harmonics rather than just the resonant components.

These beta-independent wall matrices, before including the growth rate and wall dissipation time tau_w (τ_w), are stored in a .npz file.

6. **energy_matrix_fxn** computes the total perturbed energy (potential + kinetic), including the ideal, tearing and wall contributions, as a function of the growth rate γ. This defines a non-linear eigenvalue problem for the growth rate and mode structure.

7. **calc_growth_rate** Finds the growth rate of the dominant mode by minimizing the determinant of the energy matrix over a range of gamma values. With no rotation (real solutions), the most positive growth rate is found by taking the absolute value of the determinant and initializing a Newton at large positive γ. In order to guarantee convergence to the dominant mode, the first calculation is taken at high beta (near the top of the ideal dome) where the growth rate is large and independent of the dissipation times tau_t and tau_w. The beta is then slowly ramped down towards marginal stability ($\gamma = 0$), using two existing data points at each step to initialize a guess for the next solution. While the main interest is generally the beta-limit given by the point of marginal stability, the entire ideal dome may be plotted by ramping beta upward from the top of the dome. With finite plasma rotation the dominant mode must be found in the complex plane. This is accomplished by ramping up omega (Ω) near the top of the ideal dome where the solution is largely independent of rotation. Then once again beta is ramped down keeping omega fixed.

8. **calc_eigenvector** is an optional function to compute the perturbed mode structure of the perturbed surface, using a singular value decomposition of the energy matrix function with the previously calculated growth rate. It additionally outputs the structure of the normal field and the tangential field.

For a given geometry many computed values are stored for reuse, to facilitate faster scans over a large range of parameters:

STORED VALUES

CC_internal.npz numpy zip file stores the plasma response matrix.

CC_external.npz numpy zip file stores the vacuum response matrix.

alpha_a.txt text file stores a field structure scalar 'alpha_a'.

Bi_beta_q_root.db python shelve database stores field structure parameters

'Bi' depending on 'beta', 'qa', and the equilibrium geometry.

surf_int.db python shelve database stores the geometric scalar 'Dm2' contained in the tearing response matrix, depending on 'beta', 'qa', and the equilibrium geometry.

wall_mats_rw(1.3).npz numpy zip file stores the (tau_w independent) wall response matrices, depending only upon the wall geometry.

This file **nefr_main.py** contains only functions and no actual run commands. The run commands and input specifications are contained in the separate file **nefr_toolkit.py** described below.

Run Module: nefr_toolkit.py

This file is used to run calculations using the **nefr_main.py** file described above, and to display output. Scanning values of a given parameter is implemented by refreshing the *run* object, defined in 'nefr_main.py' as a class called *nefr_run*. At the end of the file is a *def* **main** section which launches one of three main run functions:

- **scan_1d** scans a single parameter (typically beta) over a specified range and plots the real part of the growth rate for the dominant mode. It is generally used to plot a series of sampled parameters (e.g. different wall times).
- **four_beta_scan** implements a similar scan of a single parameter (typically beta), with the sampled variable automatically set to pairs of wall time (tau_w) and tearing time (tau_t) that produce the four beta branches: rp-rw, rp-iw, ip-rw and ip-iw.
- **beta_crit** scans a two-dimensional space and plots marginal stability points. It is typically used to determine how the critical beta changes with the wall distance, safety factor or shape parameters.

Section B.2 outlines how to specify inputs and run these three functions.

Settings Module: djr_settings.py

This module loads all of the numerical tools needed from the *numpy* and *scipy* packages [94], as well as the plotting tools needed from the *matplotlib* package [131]. In addition, this module is used to

set the default plot settings (e.g. fonts and axes). Other python codes (such as the reduced-MHD calculations from Chapters 3 and 4) can then load this same file and produce similar looking plots, with uniform size, fonts, labels, line width, etc.

B.2 User Tutorial

Running 'nefr_toolkit' will bring up the following options for user input:

Run Options

1 − > scan_1d

4 − > four_beta_scan

b − > beta_crit

q − > QUIT

Enter choice:

However, before choosing one of the three options, one locate the function of interest in the code and set the desired run inputs. The inputs and run options for the three functions are described below.

Initial scan of single parameter: *scan_1d*

The scan_1d function takes the run object as input. The parameter space to be scanned and sampled is then defined as follows:

1. *x_name* defines the parameter to be scanned, typically beta. The function *myrange* takes an initial value, final value and a step size. The values in *x_vals_1* are set to ramp down (descending order), whereas the values in *x_vals_2* ramp up.

2. *sample_name* defines the parameter to be sampled, that is the different curves to be plotted over the scanned parameter, with the values in the list *sample_vals*.

A good initial exercise may be to sample a few values of the tearing time 'tau_t' or wall time 'tau_w' until convinced that, despite the change in growth rate, the crossing points ($\gamma = 0$) are independent of these dissipation timescales, up to very large values ($\sim 10^8$) where a mode transition is observed to a higher beta-limit. For a preliminary test run it is recommended to run on low resolution (say

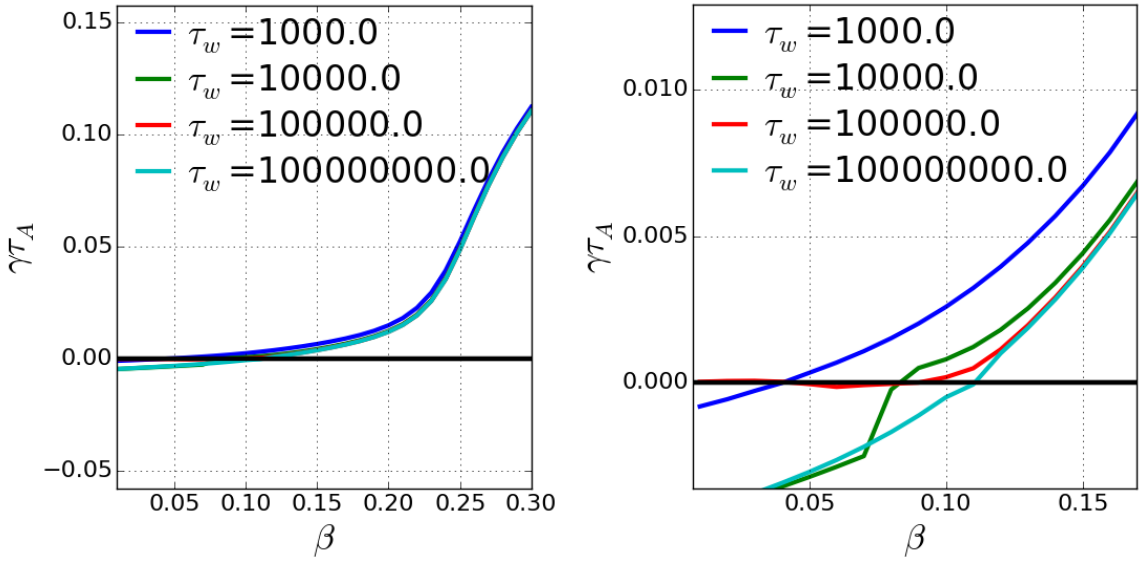

(a) (b)

Figure B.1: Low resolution calculation of the growth rate γ versus beta, for four different wall times (in Alfven time units). The left plot (a) shows a broad range up to ideal (Alfvenic) growth rates, while (b) on the right shows a close up near the marginal stability crossings.

beta-step 0.01 in *myrange*). Although the results will be choppy, the resulting plot should reveal if the given range starts at a sufficiently high growth rate and also contains a zero crossing. With the default object parameters above, let us start with setting the following input values:

```
"' INPUT "'
x_name = 'beta'
x_vals_1 = myrange(0.01, 0.30, 0.01)[::-1] # ramp down
x_vals_2 = [] # ramp up
sample_name = 'tau_w' # sample parameter
sample_vals = [1e3, 1e4, 1e5, 1e8]
```

In addition the user may change other default values in the run object. For example the inverse aspect ratio is reset for the present run to $\epsilon = 0.3$ by typing *run.eps = 0.3* In well under a minute (33 seconds on my computer), this should produce the plot shown in Figure B.1a. Zooming in on the domain near the marginal stability crossings, Figure B.1b shows on the low resolution becomes significant near the axis. The results can be rewritten by setting a higher resolution (say beta-step 0.001) and then setting *rewrite=True* in the inputs for the scan_1d function. This high resolution

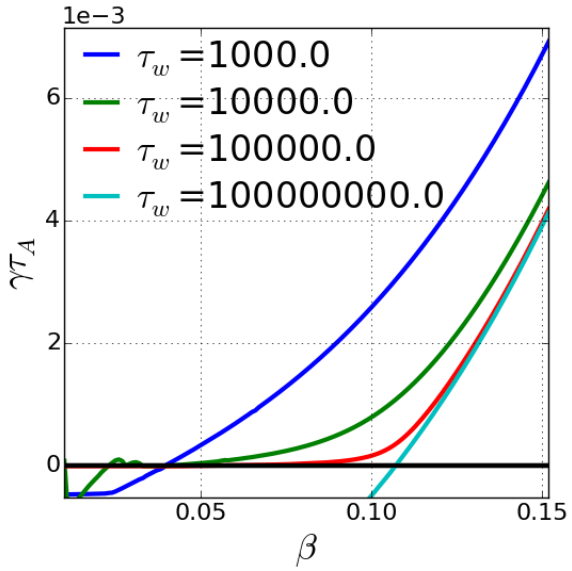

Figure B.2: Hight resolution calculation of the growth rate γ versus beta, for four different wall times (in Alfven time units), plotted near the marginal stability crossings.

calculation should take a few minutes (238 seconds on my computer). Globally, the resulting curves should look similar to the low resolution case, while the close up shown in Figure B.2 reveals a substantial improvement. While still a bit rough at very low beta, a clear transition is observed between the resistive wall and the ideal wall limit. It is important afterwards to reset *rewrite=False* so that rerunning with the same values loads existing data rather than recalculating. Note the third input in the function definition is typically set as *plot_imag=False*, but can alternately be set as *True* to plot the imaginary component corresponding to mode rotation (which is zero for the dominant mode when $\Omega = 0$). The last input *beta_normal=False* can be set to *True* in order to convert beta to the commonly used normalization

$$\beta_N \equiv \frac{\beta}{I_p[MAmp]/(a[m]B_0[T])} \times 100\% = 10^8 \frac{\beta}{I_p/(aB_0)}, \tag{B.1}$$

based on empirical observations by Troyon [132]. In the sharp boundary model, β_N can be obtained from the normalized equilibrium current

$$I_p/(aB_0) = \frac{1}{\mu_0 a B_0} \oint B_0 B_p(\theta) a h_a(\theta) d\theta. \tag{B.2}$$

Thus in this normalization the units of a and B_0 are eliminated. In terms of the unitless current

$$\mathcal{I}_p \equiv \oint B_p(\theta) h_a(\theta) d\theta, \tag{B.3}$$

β-normal can be calculated according to

$$\beta_N = \frac{4\pi \times 10}{\mathcal{I}_p} \beta. \tag{B.4}$$

Parameter scan with four branches: *four_beta_scan*

The scanned parameter name and values for this function are set the same way as for *scan_1d*. The sampled values, however, are automatically set for different combinations of the tearing time tau_t (τ_t) and wall time tau_w (τ_w), in order to generate the four beta branches:

1. resistive-plasma resistive-wall (rp-rw): finite τ_t, finite τ_w
2. resistive-plasma ideal-wall (rp-iw): finite τ_t, $\tau_w \to \infty$
3. ideal-plasma resistive-wall (ip-rw): $\tau_t \to \infty$, finite τ_w
4. ideal-plasma ideal-wall (rp-rw): $\tau_t \to \infty$, $\tau_w \to \infty$

Since the equilibrium calculations have already been carried out, there is little numerical cost in going straight to the high resolution calculation, with the following inputs:

```
x_name = 'beta'
x_vals_1 = myrange(0.01, 0.30, 0.001)[::-1] # ramp down
x_vals_2 = [] # ramp up
```

and *run.eps = 0.3*. Taking again well under a minute (37 seconds on my computer), the code should produce Figure B.3a. A close up shown in Figure B.3b clearly reveals the four marginal stability crossings corresponding to the four beta limits. The default plotting convention denotes the resistive/ideal plasma as dashed/solid, and the resistive/ideal wall as blue/red. For the higher (ideal-plasma) beta-limits, the steep curve tends to cut off at the axis rather than connecting to the stable branch of the mode. While this feature of the algorithm could be improved by fine tuning the forward-solver for the growth rate, it is of little significance since the important information is the point of marginal stability.

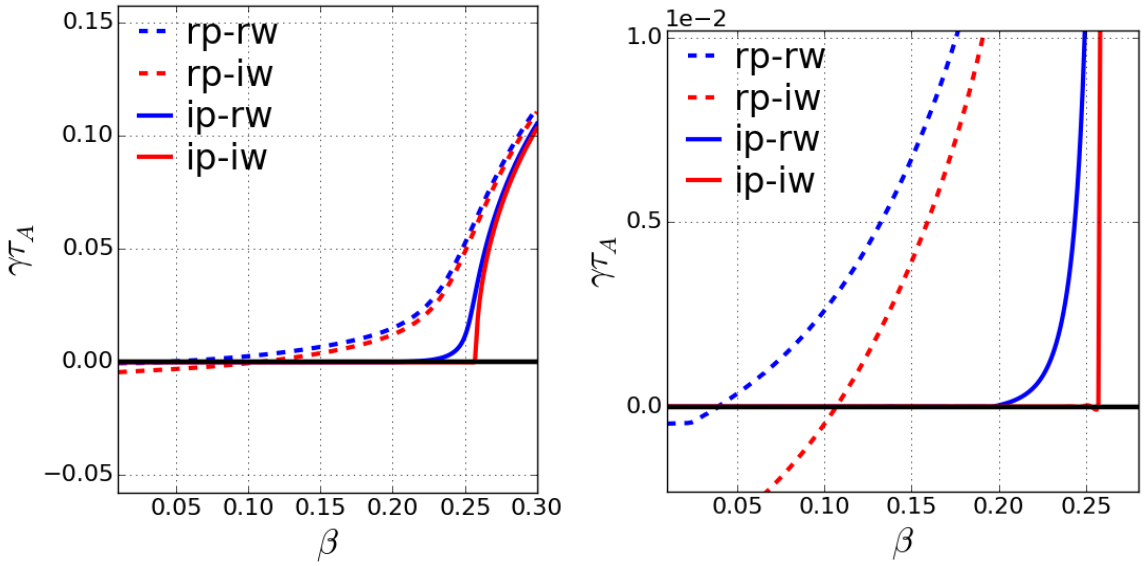

(a) (b)

Figure B.3: High resolution calculation of the growth rate γ versus beta for the four branches combining a resistive or ideal plasma with a resistive or ideal wall. The left plot (a) shows a broad range up to ideal (Alfvenic) growth rates, while (b) on the right shows a close up near the (4-beta) marginal stability crossings.

The resulting points of marginal stability are then used to initialize a search for the beta-limits in terms of an equilibrium parameter such as wall radius, safety factor, elongation, triangularity or up-down asymmetry.

Marginal stability points for the four branches: *beta_crit*

In order to examine how the four beta-limits vary with a desired parameter, a ramp down in beta is calculated for each value starting at a value with a positive growth rate. The ramp down stops at $\gamma <$ g_tol (according to the tolerance defined in the zero-finding function *crit_run*), and the resulting critical beta value is used to adapt the ramp down domain for the next parameter value. For example, let us consider a wall-radius scan with the following inputs:

y_name = 'beta'

x_name = 'frwr'

y_span = 0.02

and *run.eps = 0.3*. The new input parameter *y_span* defines the span of the ramp down domain in beta. Now for each of the four branches (rp-rw, rp-iw, ip-rw, ip-iw) the wall-radius and beta values are set separately. In the first section (rp-rw), let us set the following inputs under the condition *if x_name == 'frwr'*:

x_vals = myrange(1.1, 1.3, 0.01)[::-1]

y_vals = myrange(0.01, 0.08, 0.001)[::-1]

The wall radius values (*x_vals*, normalized by the plasma minor radius) are set to start at the default value of $r_w = 1.3$, according to the previous growth rate calculations. Since Figure B.3b shows the rp-rw limit to lie around $\beta = 0.04$, it is safe to initialize beta in *y_vals* to ramp down from 0.08. As before, the beta step is taken to be 0.001. At this high resolution it is expected to take approximately 40 beta-steps down from 0.08 before locating the critical beta point. The calculation for the following wall radius ($r_w = 1.29$) will initialize at $\beta = \beta_{crit}(r_w = 1.3) + \text{y\_span}$. After traversing the space of *x_vals*, the algorithm moves on to rp-iw, ip-rw and ip-iw, which are each initialized separately based on the appropriate marginal stability crossing found in Figure B.3b.

With the equilibrium computations already completed in previous steps, the entire calculation should only take a couple of minutes (115 seconds on my computer) to produce Figure B.4. The ideal-wall limits, which approach infinity as the wall radius approaches the plasma radius ($r = 1$), are cut off here above $\beta = 0.8$, above which the equilibrium calculation of B_i begins to face numerical problems. The resistive-wall limits are independent of wall radius because they coincide with the no-wall limits.

The steps outlined above can be used to examine the effect of the safety factor, rotation, ferritic wall permeability and geometric parameters on the domains of plasma stability. Varying equilibrium shape parameters such as ϵ, κ, δ_x or δ_y takes longer (up to an hour) since the ideal plasma and vacuum response matrices would need to be calculated at each step.

Good luck!

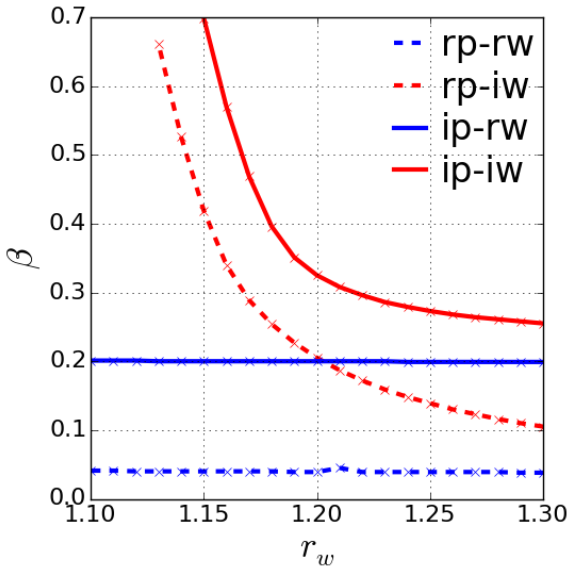

Figure B.4: Critical-beta values of the four branches versus wall radius.